NKS-468
ISBN 978-87-7893-563-2

Barsebäck as a Research and Development Platform, Extraction and Analysis of Service-aged and Irradiated Reactor Pressure Vessel Material

Pål Efsing[1,4]
Jonas Faleskog[1]
Daniela Klein[1]
Noora Hytönen[2]
Sebastian Lindqvist[2]
Kristina Lindgren[3]
Mattias Thuvander[3]
Jenny Roudén[4]

[1] Department of Engineering Mechanics – unit of Solid Mechanics, Royal Institute of Technology (KTH), SE-100 44 Stockholm Sweden

[2] VTT Technical Research Centre of Finland Ltd, PO Box 1000, FI-02044 VTT, Espoo, Finland

[3] Chalmers University of Technology, Department of Physics, SE-412 96, Göteborg, Sweden

[4] Ringhals AB, SE-43285 Väröbacka, Sweden

February 2023

Abstract

As part of the NKS-R program, VTT, Chalmers University of Technology and KTH have extended the mechanical and microstructural testing in order to analyze the as-aged material properties of the retired reactor pressure vessel, RPV, from Barsebäck unit 2. The testing included Impact testing of material from the reactor pressure vessel and microstructural characterization of the weld metal using LOM, SEM and APT. Due to the nature of the work, the NKS-project is connected to a number of adjacent activities, including support from the Finnish Nuclear Safety Program, the SAFIR-program, the Swedish Radiation Safety Authority SSM and Swedish Centre for Nuclear Technology, and SKC.

Key words

Low alloy steel, irradiation effects, fracture toughness, ductile to brittle transition temperature, constraint effects, high resolution microscopy, microstructural characterization

NKS-468
ISBN 978-87-7893-563-2
Electronic report, February 2023
NKS Secretariat
P.O. Box 49
DK - 4000 Roskilde, Denmark
Phone +45 4677 4041
www.nks.org
e-mail nks@nks.org

Barsebäck as a Research and Development Platform, Extraction and Analysis of Service-aged and Irradiated Reactor Pressure Vessel Material

Final Report from the NKS-R BREDA-RPV 2022 activity

(Contract: AFT/NKS-R(22)118/1)

Pål Efsing[1,4], Jonas Faleskog[1], Daniela Klein[1]
Noora Hytönen[2], Sebastian Lindqvist[2]
Kristina Lindgren[3], Mattias Thuvander[3]
Jenny Roudén[4]

[1] Department of Engineering Mechanics – unit of Solid Mechanics, Royal Institute of Technology (KTH), SE-100 44 Stockholm Sweden
[2] VTT Technical Research Centre of Finland Ltd, PO Box 1000, FI-02044 VTT, Espoo, Finland
[3] Chalmers University of Technology, Department of Physics, SE-412 96, Göteborg, Sweden
[4] Ringhals AB, SE-43285 Väröbacka, Sweden

Table of contents

	Page
1. Introduction/Background	3
2. VTT progress – microstructural and mechanical properties	4
3. CTH progress – Microstructural assessment of aged material using Atom Probe Tomography (APT)	6
4. KTH progress – Modelling of failure probabilities in aged materials	6
5. Conclusions	6
6. References	7

1. Introduction/Background

The objectives of the Nordic collaborative project on Barsebäck Reactor Pressure Vessel, where material is used for evaluation of embrittlement of pressure vessel steels, are multi-faceted. From the perspective of the participating entities, it is a unique opportunity for researchers to perform mechanical and microstructural investigations on a service aged reactor pressure vessel and connected components in an area where the laboratories, regulators and utilities have great needs. Further, it allows for knowledge retention and creating a living relationship between the young engineers in the Nordic area under the oversight and mentorship of senior partners at the same time as the relevant institutes and institutions are connected with the industry. It also connects the nano, micro, and macro aspects of the as-aged properties of low alloy steels by the use of different assessment tools from Atom Probe Tomography, APT, to fracture mechanical testing. From an end-user perspective the data produced will extend the knowledge base on the active ageing mechanisms in a vital component for the owners and regulators of nuclear power plants. The results will allow for comparison between the data produced during execution of surveillance of the ageing and degradation processes, and also the attenuation of radiation effects through the thickness of the pressure vessel wall. Finally, it also allows VTT to assess the new infrastructure in the Centre for Nuclear Safety, CNS.

In the 2022 NKS-R program, the participants of the BREDA project have continued the investigations of ageing effects on Reactor pressure vessel steels as outlined in the previous summary reports dating from 2016 to 2021 [Efsing et al. 2016, 2018, 2019, 2020, 2021]. Since the program includes a large number of steps; extraction, decontamination and pre-cutting, transport of material, sample manufacturing, mechanical and microstructural testing, and analysis of the collected materials, the schedule has been very extensive. The objective of the project is to utilize materials harvested from a retired RPV to provide the Nordic regulatory bodies and the operators of nuclear power plants, as well as the available academic support resources, a firm basis of understanding on how aging has influenced the mechanical properties of the aged component. The donor of samples in the project is the decommissioned Barsebäck 2 Boiling Water Reactor RPV rendering materials in both irradiated and thermally aged conditions. Further, it will give knowledge and insight into the correctness of the existing surveillance programs, as well as the influence of long-term thermal ageing of materials used for large pressure vessels in the nuclear industry such as the RPV and the Pressurizer, PRZ.

In 2016, the first steps were executed by baseline studies of unirradiated samples and comprehensive literature reviews of the issues in the area. Further, issues regarding the extraction methodology and the actual materials harvesting were outlined and initial qualification of the methodologies were performed. The harvesting work in 2018, and the collection of background information, was fully financed by the Swedish utility companies Ringhals AB, Forsmark Kraftgrupp AB and OKG AB as part of an umbrella project under the auspices of Energiforsk with Monika Adsten as the primary program manager at that time. That portion of the work resulted in the basis of the BRUTE activity of the Finnish state SAFIR umbrella, which was finished in 2022.

The activities in the 2018 to 2021 time period included planning and extraction of trepans from the RPV of Barsebäck 2, decontamination and preparation of the trepans at Ringhals, shipping of the samples to Finland and mechanical and microstructural testing in hot-cell laboratory. As a preparatory study, a number of archive materials, both identical to the actual RPV and other weldments produced with weld metal of the same requirements, were studied in order to establish an understanding of the initial microstructural and mechanical properties. In 2020, mechanical and microstructural tests were initiated. The first step in the actual testing was performed using material form the RPV head (RPVH) which was reported in 2021. The objective here was to establish a credible basis for the effect of thermal ageing in the material.

The key deliverables during BREDA-RPV 2022 are the open publications on the microstructural assessment of material from the RPVH and preliminary results from the beltline [Hytönen et al 2022, presented at Fontevraud 10] and an assessment of the thermally aged material [Boåsen et al 2022 in Engineering Fracture Mechanics, paper id 108248]. Further, the study on fracture initiation that has been executed in the companion project BRUTE was reported by [Que 2022 in Journal of Nuclear Materials, paper id 153925]. Noora Hytönen also presented the progress of the two adjacent projects BREDA/BRUTE at a research meeting, ICG-EAC, which was held in Tampere in May 2022. In August the BREDA and BRUTE project held a workshop at KTH to present and discuss the progress and recent findings regarding the modelling efforts, mechanical tests as well as microstructural studies. At the workshop, in addition to presentations on the progress within the project by Noora Hytönen, Daniela Klein, Mattias Thuvander, and Sebastian Lindqvist, Noora presented VTTs prospective BRIGHT project to be proposed to the next Finnish national program, SAFER.

KTH finalized a complementary activity studying the possibilities to reliably produce shallow edge defects on the surface of samples for mechanical testing. This is part of a different study but will allow for a firm foundation for future work regarding structural integrity of real components and the effects of constraint on irradiated and thermally aged material.

2. VTT progress – microstructural and mechanical properties

In 2022, the focus was on testing of the circumferential beltline weld (trepan 8), extracted from the weld seam W16, and the surveillance specimens. The surveillance specimens are non-tested specimens from the surveillance programme. Three specimens are from the surveillance chain denoted “C” (at a fluence of ~$0.1\cdot10^{19}$ n/cm^2) and three from chain “G” (fluence at $5.9\cdot10^{19}$ n/cm^2). For the surveillance materials, fracture toughness specimens were manufactured and tested. For the circumferential weld, tensile testing, impact testing and fracture toughness testing were performed. The material was sampled from the ¼ wall thickness location of the trepans extracted from the beltline region according to figure 1. The fluence of G-chain is approximately equal to the estimated 40-year dose at Pressurized Water Reactor, PWR, RPV, where-as the estimated 60-year dose for a BWR RPV is approximately 6 times lower, or slightly less than $1\cdot10^{19}$ n/cm^2.

The impact tests indicate for the circumferential beltline weld metal that the impact toughness is comparable to the RPV head weld. Supplementary impact tests were performed with specimens reconstituted from tested specimen halves. The reconstitution technique had not previously been utilised at VTT’s Centre for Nuclear Safety, CNS, giving the tests an additional value by development of techniques at CNS. Fracture toughness tests were performed with miniature compact tension, MCT, specimens. The successful fracture toughness tests demonstrate the inhomogeneity of the weld materials resulting from the regular as-welded and reheated multilayer structure. The multimodal transition temperature. T_M. for the circumferential beltline weld is -77.9 °C and -100 °C and 90 °C for surveillance chains C and G, respectively.

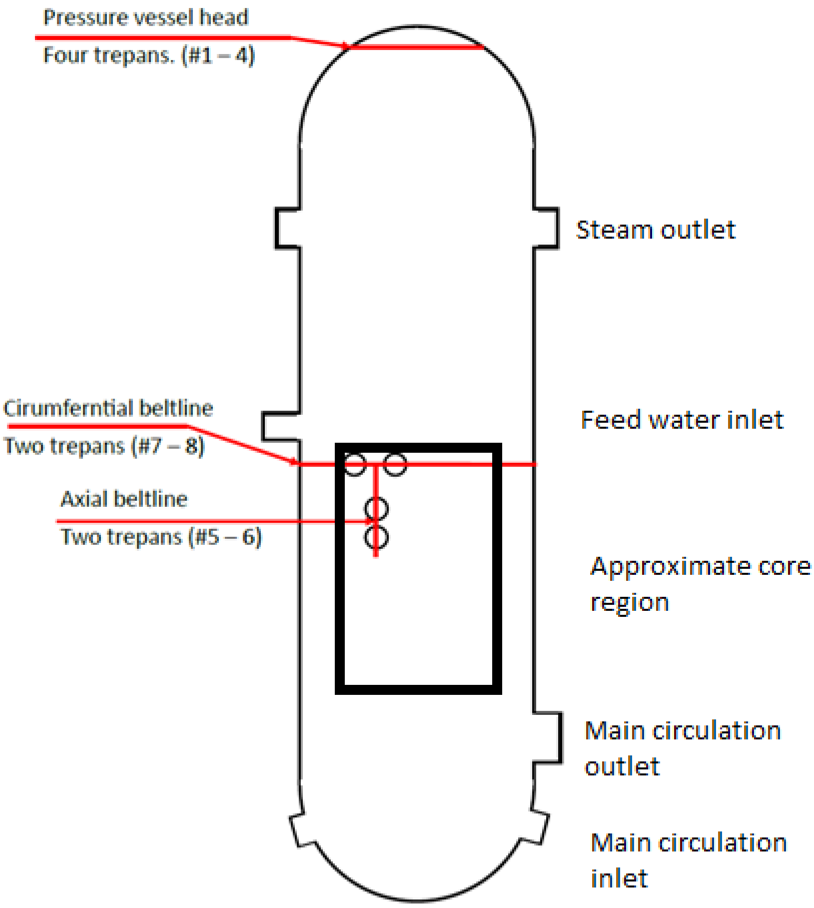

Figure 1, sketch of the RPV and approximate locations for the 8 extracted trepans.

In 2022, microstructural investigations included general characterisation of the circumferential beltline weld through wall thickness, including macro- and microhardness testing, and fractography of the brittle fracture specimens. The macrohardness of the weld metal was comparable to the RPV head weld. Fracture surfaces of specimens have been investigated with Scanning Electron Microscope, SEM, and Energy Dispersive Spectroscope, EDS. Similar features are found in brittle impact and fracture toughness specimens. In all investigated brittle specimens, a brittle oxide inclusion was found at the primary initiation site. A few surveillance MCT specimens were examined for fracture surface and similar initiation features were observed. The results were reported at the Fontevraud 10 conference in France in September 2022 [Hytönen 2022]. The study on fracture initiation was also reported by [Que 2022] in the open literature in 2022.

The chemical composition of the axial and circumferential beltline welds was measured at CNS using glow-discharge optical emission spectrometry, GDOES. The composition of the weld metal was measured through thickness and variation in certain elements were observed within the welds and between the welding directions of the multi-pass double U-welds.

3. CTH progress – Microstructural assessment of aged material using Atom Probe Tomography (APT)

The earlier achieved atom probe tomography, APT, data of the beltline region of Barsebäck RPV was further analysed. No obvious clustering was observed, but when doing statistical analysis of the distribution of atoms, there is some deviations between reference material and irradiated Barsebäck material. The statistical analysis was mainly performed using the radial distribution function, RDF, which shows that there is a clustering tendency of Ni atoms (and to a lesser extent of Cu). This tendency is weak and is not expected to influence the mechanical properties. However, it shows that clustering has started, and it is possible that it can affect the properties after much longer times.

A new APT instrument was installed at Chalmers at the end of 2022. This instrument has higher detection efficiency and improved ion optics, and, hopefully, a lower background signal. In the near future the RPV material from Barsebäck will be investigated, and it will be interesting to find out if the early clustering will be more visible. Regarding RPV steel research, Chalmers is also involved in the EU-funded program ENTENTE.

4. KTH progress – Modelling of failure probabilities in aged materials

KTH has analyzed the tests performed on round notched bar (RNB) specimens and the additional tests on single edge notched bend specimens in order to validate the modelling framework reported in [Boåsen 2021]. The work was carried out by Daniela Klein as a part of her PhD thesis. She has also performed a SEM investigation under supervision of experts at VTT in Finland, during a visit there in April, 2022. It could not be confirmed that failure in the RNB specimens was due to the intergranular mechanism as suggested by the modelling framework reported in [Boåsen 2021]. Also, the elongation of the specimens at failure was severely underestimated based on the latter model.

The new hypothesis is that the as-welded and the reheated zone in the weld material have different failure properties, due to different particle distributions in the zones. It is further assumed that the phosphorous segregation due to thermal aging affects the reheated zone more, as the grain boundary density is higher. Therefore, Daniela has investigated the influence of spatial heterogeneities and developed a new model based based on the weakest-link concept that covers the whole range from small-scale-heterogeneity to large-scale-heterogeneity. A first draft of this study is now under revision, which will be submitted for publication.

In August a joint workshop between the NKS supported FEMMA and BREDA projects was held at KTH with invited participants from the utility companies and regulators. The workshop was well attended and allowed the scientists performing the research to present their respective programs to a relevant audience and to receive feedback from the industrial representatives.

5. Conclusions

Samples have been extracted from the RPV of Barsebäck Unit 2 and shipped to VTT. Several milestones of the project were completed and in part reported in 2022, i.e. the mechanical testing of the beltline weld.

The FE-model regarding failure probabilities has been extended to better handle the whole range of defects in the different microstructural zones in the welds, from small-scale-heterogeneity to large-scale-heterogeneity, based on the weakest-link concept. Results from the mechanical testing is starting to become available thus allowing for initial assessments of the resulting changes in the properties. This work is foreseen to be extended in 2023 with expanded collaboration between the executing partners and the industrial/regulatory partners. Studies on the BWR irradiated materials have previously shown few or no signs of agglomerates as have been evident in the higher dose materials previously investigated. However, a re-examination of the data shows signs of clustering of Ni that may be the precursors of agglomeration.

6. References

Boåsen M. et al, A weakest link model for multiple mechanism brittle fracture – Model development and application, In *J of the Mechanics and Physics of Solids*, vol. 147, 2021

Efsing P et al. 2016, Barsebäck as research and development platform, extraction and analysis of reactor pressure vessel material, Final report for the BREDA2016 activity, NKS-385

Efsing P et al., 2018 Barsebäck as research and development platform, extraction and analysis of reactor pressure vessel material, Final report for the BREDA2018 activity, NKS-418

Efsing P et al, 2019 Barsebäck as research and development platform, extraction and analysis of reactor pressure vessel material, Final report for the BREDA2019 activity, rev 1, NKS-431

Efsing P et al, 2020 Barsebäck as research and development platform, extraction and analysis of reactor pressure vessel material, Final report for the BREDA2020 activity, NKS-443

Efsing P et al, 2022 Barsebäck as research and development platform, extraction and analysis of reactor pressure vessel material, Final report for the BREDA2021 activity, NKS-455

Hytönen et al, Comparison of Weld Microstructure and Brittle Fracture Initiation of RPV Head Weld and Beltline Axial Weld, In Proceeding from the *International Symposium Contribution of Materials Investigations and Operating Experience to LWRs' Safety, Performance and Reliability*, FONTEVRAUD 10, September 19 to 22, 2022, Avignon, France

Que et al, Brittle fracture initiation in decommissioned boiling water reactor pressure vessel head weld, in *J of Nuclear Materials*, 2022, vol 569. Paper id: 153925.

Acknowledgements

NKS conveys its gratitude to all organizations and persons who by means of financial support or contributions in kind have made the work presented in this report possible.

The support from the Finnish nuclear safety program, the SAFIR2022-program, the Swedish Radiation Safety Authority and the Swedish Centre for Nuclear Technology, SKC as well as the Swedish Nuclear Power Plants permit holders and owners (Ringhals AB, Forsmarks Kraftgrupp AB, OKG AB, Vattenfall AB, Fortum and Uniper) for the work is gratefully acknowledged.

Appendices

1. N Hytönen et. al., Comparison of Weld Microstructure and Brittle Fracture Initiation of RPV Head Weld and Beltline Axial Weld, Presented at Fontevraud 10, International Symposium on Contribution of Materials Investigations and Operating Experience to LWRs' Safety, Performance and Reliability, Avignon, France, September 19-21, 2022, Paper Id 50.

2. M Boåsen et. al., Analysis of thermal embrittlement of a low alloy steel weldment using fracture toughness and microstructural investigations, In *Engineering Fracture Mechanics*, vol. 262, 2022, paper id 108248

3. Z. Que et al, Brittle fracture initiation in decommissioned boiling water reactor pressure vessel head weld, In *J of Nuclear Materials*, vol 569, 2022, paper Id 153925

Bibliographic Data Sheet **NKS-468**

Title	Barsebäck as a Research and Development Platform, Extraction and Analysis of Service-aged and Irradiated Reactor Pressure Vessel Material
Author(s)	Pål Efsing[1,4], Jonas Faleskog[1], Daniela Klein[1] Noora Hytönen[2], Sebastian Lindqvist[2] Kristina Lindgren[3], Mattias Thuvander[3] Jenny Roudén[4]
Affiliation(s)	[1] Department of Engineering Mechanics – unit of Solid Mechanics, Royal Institute of Technology (KTH), SE-100 44 Stockholm Sweden [2] VTT Technical Research Centre of Finland Ltd, PO Box 1000, FI-02044 VTT, Espoo, Finland [3] Chalmers University of Technology, Department of Physics, SE-412 96, Göteborg, Sweden [4] Ringhals AB, SE-43285 Väröbacka, Sweden
ISBN	978-87-7893-563-2
Date	February 2023
Project	NKS-R BREDA2022 activity (Contract: NKS_R_2016_118)
No. of pages	8
No. of tables	0
No. of illustrations	1
No. of references	8
Abstract max. 2000 characters	As part of the NKS-R program, VTT, Chalmers University of Technology and KTH have extended the mechanical and microstructural testing in order to analyze the as-aged material properties of the retired reactor pressure vessel, RPV, from Barsebäck unit 2. The testing included Impact testing of material from the reactor pressure vessel and microstructural characterization of the weld metal using LOM, SEM and APT. Due to the nature of the work, the NKS-project is connected to a number of adjacent activities, including support from the Finnish Nuclear Safety Program, the SAFIR-program, the Swedish Radiation Safety Authority SSM and Swedish Centre for Nuclear Technology, and SKC.
Key words	Low alloy steel, irradiation effects, fracture toughness, ductile to brittle transition temperature, constraint effects, high resolution microscopy, microstructural characterization

Comparison of Weld Microstructure and Brittle Fracture Initiation of RPV Head Weld and Beltline Axial Weld

N. Hytönen[1], P. Arffman[1], J. Lydman[1], S. Lindqvist[1], Z. Que[1], P. Efsing[2]

1 VTT Technical Research Centre of Finland
2 Ringhals AB, 432 85 Väröbacka, Sweden

Content

- Background
- Materials and methods
- Microstructural characterisation
- Brittle fracture initiation
- Discussion
- Summary

Background

- Increasing the mechanistic understanding of brittle fracture initiation and microstructure after thermal ageing and neutron irradiation
  → Safe long-term operation and extended power plant life-time
- Current understanding of brittle fracture is obtained mainly studying base materials
  - High-density of carbides and low-density of inclusions
  - Relatively homogeneous microstructure
- Weld metals are considered more critical; inhomogeneous microstructure and relatively large amount of non-metallic inclusions due to welding metallurgy
  - Alloy elements are prone to clustering and (co-)segregation to grain boundaries during ageing
- Material from decommissioned Barsebäck unit 2 BWR, in operation for 28 years
  - RPV head weld W28 → thermal loading, non-irradiated
  - RPV beltline axial weld W14 → thermal loading & irradiated

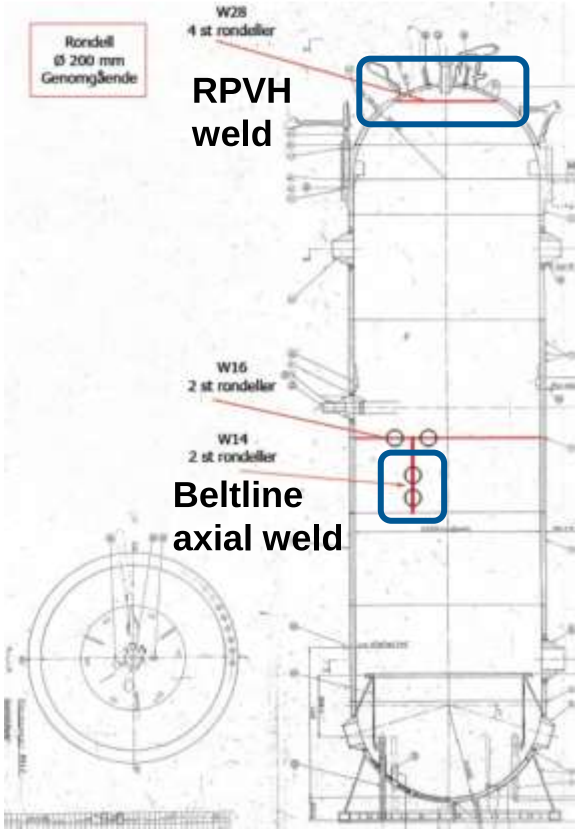

Materials

- Low-alloy steel weld with high Ni- and Mn-content, low Cu-content
- Microstructural characterisation through wall thickness
- Mechanical testing specimens cut from 1/4T depth from the RPV inner surface
  - T-S orientation when L is the welding direction

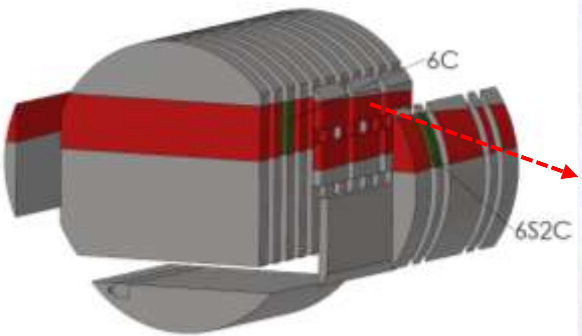

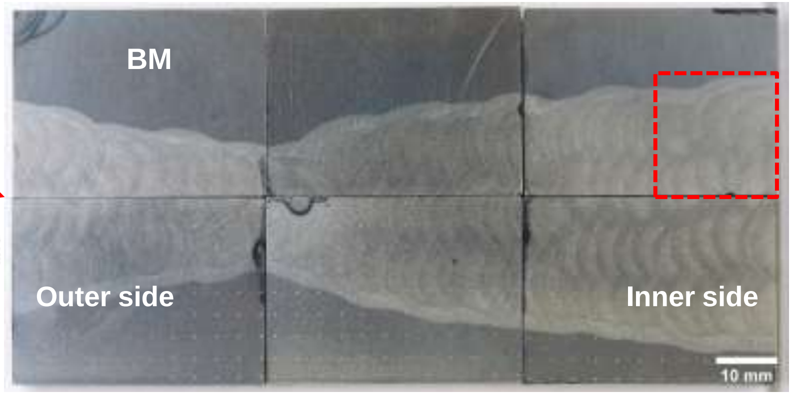

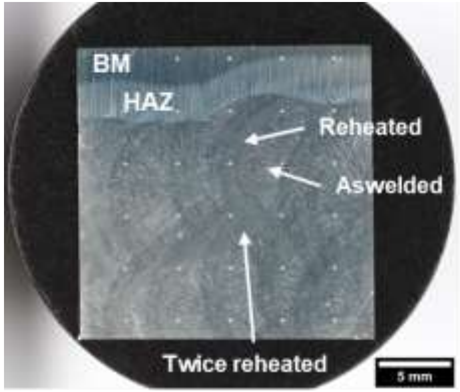

wt.%	C	**Mn**	**Ni**	Si	Mo	Cr	S	P	Cu	Al	Ti	Co	Fe
SAW weld	0.057	**1.43**	**1.48**	0.15	0.41	0.03	0.007	0.008	0.060	0.024	0.003	0.020	bal.
MMA weld	0.037	**1.38**	**1.22**	0.25	0.37	0.03	0.007	0.007	0.004	0.002	0.004	0.018	bal.

Methods

- VTT CNS hot laboratory
- Microstructural studies:
  - LOM/SEM/EBSD/hardness
- Fracture mechanical testing:
  - Impact toughness (Charpy V-notch) using instrumented pendulum
    - Temperature range: –120°C…+60°C
    - Determine DBTT
  - Fracture toughness (Miniature C(T))
    - Master Curve –method*
    - Temperature –146°C… –114°C
    - Different specimen geometries for RPVH and beltline due to in-cell test method development
- Fractography
  - Stereography/SEM/EDS
  - CVN: Brittle fracture considered below T_{41J}

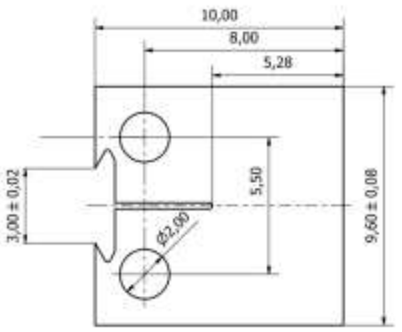

MCT RPVH

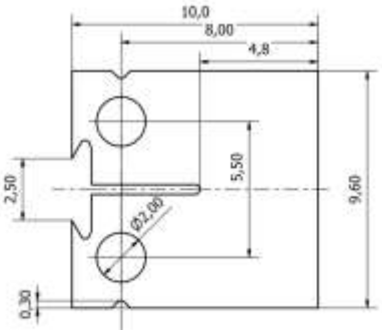

MCT beltline axial

 * ASTM E1921

Microstructural characterisation

Metallographic microstructure

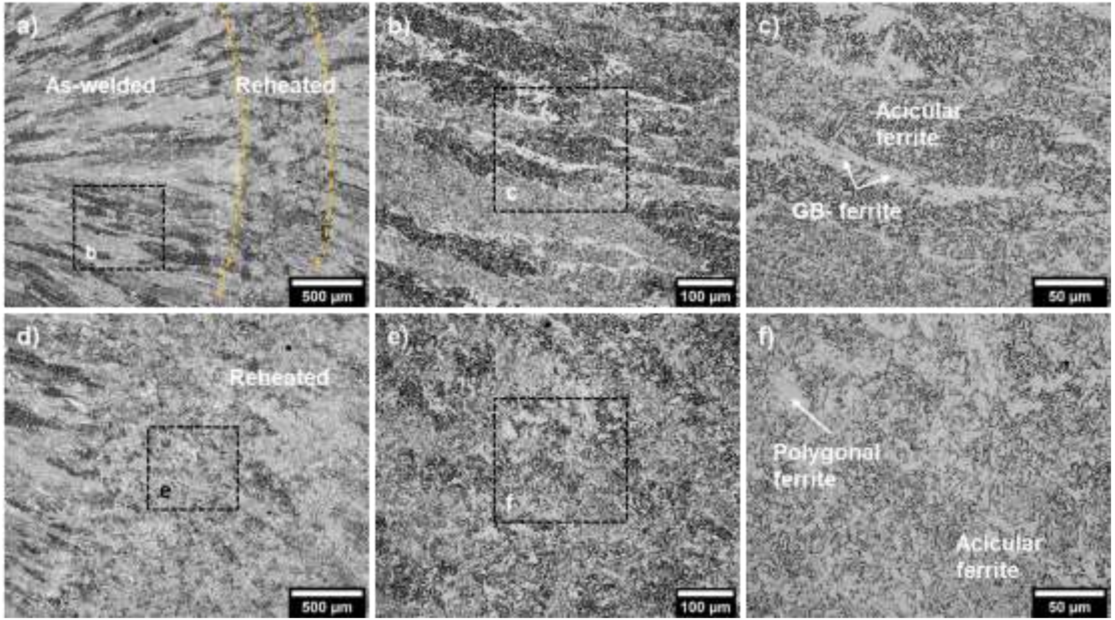

Main features:

- Aswelded microstructure:
  - Dendrites and acicular ferrite with interdendritic GB-ferrite
- Reheated microstructure:
  - Equiaxed grains of polygonal ferrite and acicular ferrite
- Beltline weld: appears more distinct GB-ferrite
- Complete weld bead height ~3 mm in beltline but ~4 mm in RPVH

Hardness HV10 and HV1

- RPVH average ~210 HV10
- Beltline axial average ~190 HV10
- HV1 peak across fusion boundary at CG-HAZ

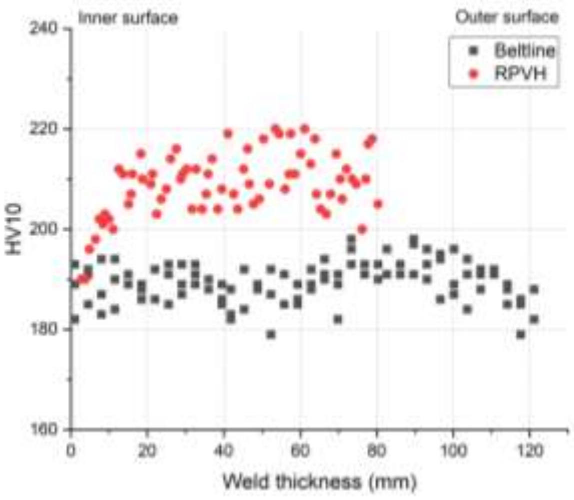

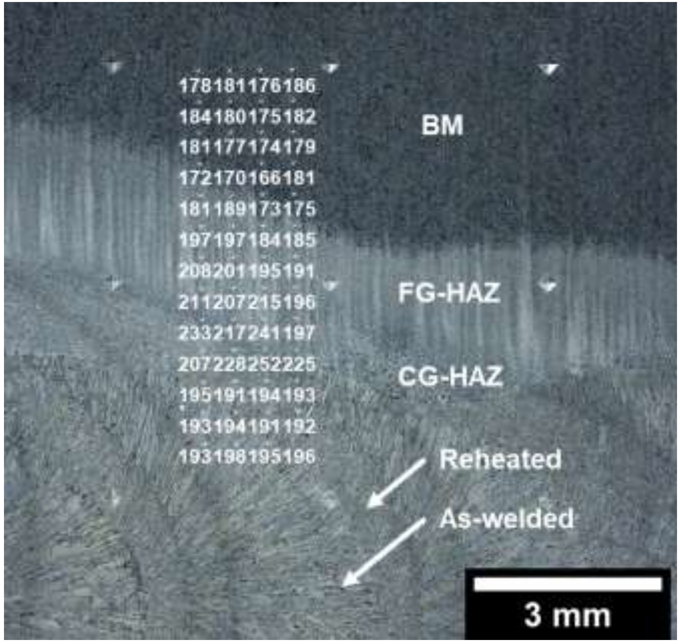

Brittle fracture initiation

Fracture mechanical testing

- Instrumented impact toughness testing
  - RPVH: T_{41J}= –75 °C
  - Beltline: T_{41J}= –95 °C
  - → Negligible thermal embrittlement
  - Fractographic examination on 9 brittle specimen in the lower part of the curve, below 41 J for both sets

- Fracture toughness testing
  - Master Curve -method (multimodal T_0 analysis)
  - RPVH: T_m= –109.4 °C
  - Beltline: T_m= –96.5 °C
  - Fractographic examination on all fully brittle specimen

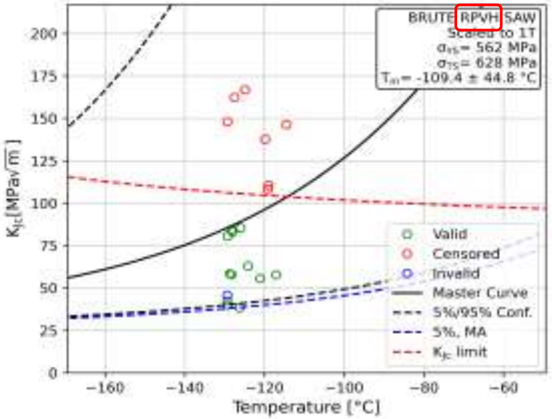

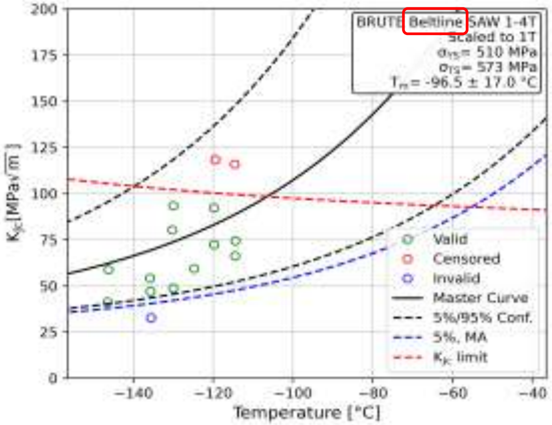

Fractography

- Transgranular cleavage fracture
- **Primary initiation site** can be determined following the macro-features and river patterns
- Broken or debonded from the matrix
- RPVH all initiation sites:
  - Brittle non-metallic inclusions of FeMnAlSi-(S)O
  - Size range ~0.5 – 2.5 µm

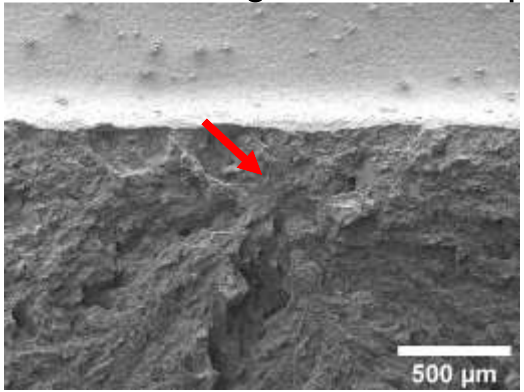

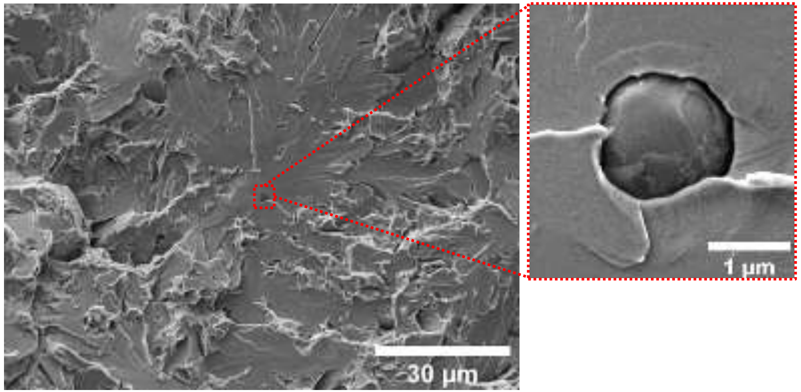

Fractography

- **Primary initiation site** in beltline axial weld has also a second type of initiator
  - Brittle non-metallic inclusions of FeMnAlSi-(S)O
  - Irregular-shaped inclusions of FeMnMo(S/C)
  - Size range ~0.2 – 2.3 µm
- IG observed surrounding the irregular-shape inclusion and initiation site

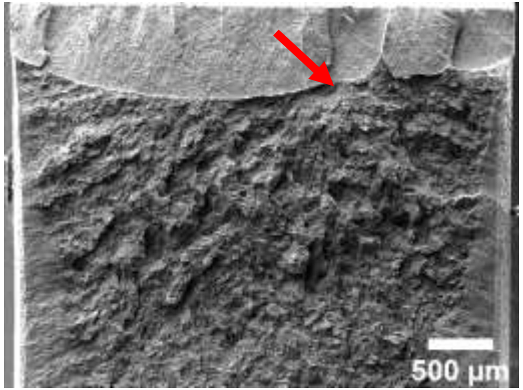

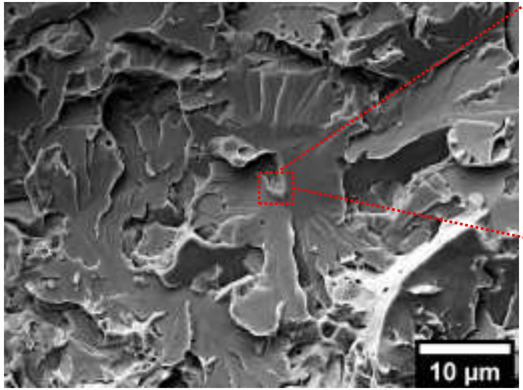

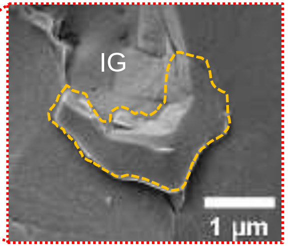

Discussion

- The fracture properties of the welds are highly similar:
  - Thermal ageing appears negligible as well as radiation damage when comparing the head weld and beltline axial weld
  - RPVH: T_{41J}= –75 °C vs. Beltline: T_{41J}= –95 °C
  - RPVH: T_m= –109.4 °C vs. Beltline: T_m= –96.5 °C
  - Indications that the beltline weld is softer and tougher than RPVH
- Fracture appearances between testing types have minor differences, the MCT causing more deformation
- Brittle fracture initiates from the largest inclusion in the effective process zone, acting as the weakest link
- Two different types of inclusions were observed
  - Roundish non-metallic inclusions → intragranular
  - Irregular-shaped inclusions → intergranular

Summary

- Multi-pass weld with as-welded and reheated regions
  - Majority of the as-welded region is acicular ferrite and ID GB-ferrite
  - Majority of the reheated region is polygonal ferrite
- The overall macrohardness of the RPVH is ~20HV10 higher than the beltline axial weld
- The fracture mechanical testing does not indicate ageing effect but overall tougher properties for the beltline axial weld
  - The fracture toughness tests demonstrate the inhomogeneity of the weld metal and the multimodal analysis provides the most reliable T_0
- Weakest links are the relatively large inclusions
  - Size range ~0.3 – 2.5 µm

Acknowledgement

- Finnish national nuclear safety programme SAFIR2022 for funding the research project
- BREDA (Barsebäck Research and Development Arena) programme for providing the research material

VTT

beyond the obvious

Noora Hytönen
noora.hytonen@vtt.fi

@VTTFinland

www.vttresearch.com

Engineering Fracture Mechanics 262 (2022) 108248

Contents lists available at ScienceDirect

Engineering Fracture Mechanics

journal homepage: www.elsevier.com/locate/engfracmech

Analysis of thermal embrittlement of a low alloy steel weldment using fracture toughness and microstructural investigations

Magnus Boåsen [a,*], Kristina Lindgren [b], Martin Öberg [a], Mattias Thuvander [b], Jonas Faleskog [a], Pål Efsing [a]

[a] Solid Mechanics, Department of Engineering Mechanics, KTH Royal Institute of Technology, SE-100 44 Stockholm Sweden
[b] Department of Physics, Chalmers University of Technology, SE-412 96 Göteborg, Sweden

A B S T R A C T

A thermally aged low alloy steel weld metal is investigated in terms of its fracture toughness and microstructural evolution and compared to a reference. The main purpose of the study is to investigate the effects of embrittlement due to thermal ageing on the brittle fracture toughness, and its effects on the influence of loss of crack tip constraint. The comparison of the investigated materials has been made at temperatures that give the same median fracture toughness of the high constraint specimens, ensuring comparability of the low constraint specimens. Ageing appears to enable brittle fracture initiation from grain boundaries besides initiation from second phase particles, making the fracture toughness distribution bimodal. Consequently, this appears to reduce the facture toughness of the low constraint specimens of the aged material as compared to the reference material. The microstructure is investigated at the nano scale using atom probe tomography where nanometer sized Ni-Mn-rich clusters, precipitated during ageing, are found primarily situated on dislocation lines.

1. Introduction

When assessing degradation due to ageing in low alloy steels used as structural materials in pressure vessel components both base and weld metals must be considered, as for example in reactor pressure vessels in nuclear power plants. In this type of materials in nuclear applications, ageing mainly occurs by neutron irradiation and thermal ageing, and generally manifests itself as a hardening effect and an increase in the ductile-to-brittle transition temperature, or in another word, *embrittlement*. In pressurized water reactors (PWRs), the pressurizer regulates the system pressure and thereby the temperature within the primary loop such that the water is kept from boiling. Following the replacement of the pressurizer in Ringhals unit 4 (R4) in 2011, material extraction was carried out in order to study potential ageing effects on the materials after 28 years of operation. Initial investigations of two of the weldments from the pressurizer material displayed a noteworthy increase in the transition temperature $\Delta T_{41J} = \{78 \text{ and } 71\}$ ℃ and an increase of the yield strength $\Delta R_{p02} = \{128 \text{ and } 59\}$ MPa, displaying a clear indication of embrittlement due to thermal ageing at the operating temperature of 345 ℃ (no irradiation present in the pressurizer).

Embrittlement is a key aspect in the structural integrity ageing assessment of any structure. Therefore, understanding the changes in the fracture toughness and all its features for a material that undergoes embrittlement is necessary. The cleavage fracture toughness of ferritic steels is strongly dependent on temperature, size and crack tip constraint. Generally, it can be stated that higher temperature endorses a more ductile behavior, larger specimens or components will be more brittle, and high constraint will produce a lower fracture toughness than low constraint. To our knowledge, no studies have been published concerning the constraint effect on fracture toughness after the material has undergone embrittlement and how this relates to the behavior of a reference material.

* Corresponding author at: KTH Solid Mechanics, Teknikringen 8D, SE-100 44 Stockholm Sweden.
E-mail address: boasen@kth.se (M. Boåsen).

https://doi.org/10.1016/j.engfracmech.2022.108248
Received 13 July 2021; Received in revised form 8 October 2021; Accepted 5 January 2022
Available online 12 January 2022

The prevailing explanation of embrittlement due to thermal ageing of low alloy steels in nuclear applications is impurity segregation towards prior austenite grain boundaries, e.g. phosphorus, commonly referred to as grain boundary embrittlement. Studies of thermal ageing include a wide spectra of base and weld metals from reactor types such as the VVER-1000 [1–4], as well as the western PWRs featuring the typical steels A508 and A533 or its equivalents [5–11]. All studies referenced here, report on intergranular fracture due to impurity segregation caused by thermal ageing.

In the extensive review of intergranular failure in steels by Briant and Banerji [12], it is noted that some distinguishable phenomena appear to be related to intergranular failure. One being that segregation of elements from groups IV-VI in the periodic table appears to yield the most potent grain boundary embrittlement, which is also mentioned by McMahon [13]. These groups include elements such as Si, Sn, P and S, which are not uncommon impurities or alloying elements in the steels of interest. Another is that a grain size effect appears to emerge where microstructures with larger grains yields more intergranular fracture than for the case of smaller grains. The authors of [12] speculate that this could be due to a dilution of the impurity elements due to the difference in grain boundary area in relation to grain volume, for the case of smaller grains. This implies that a microstructure with smaller grains would result in a larger degree of dilution of impurities across the grain boundaries and thus less embrittlement, than in a microstructure with larger grains *ceteris paribus*. Another notable phenomenon is the effect of co-segregation of elements such as Ni and Mn, which is indicated to yield a faster and more potent embrittlement [12,14,15]. In a study by Banerji et al. [16] concerning the effects of impurities and hydrogen on intergranular fracture in a commercial steel, several heats were tempered at different temperatures in the range 50–625 ℃ and then subjected to Charpy impact testing at room temperature. One of the findings in the study was that the largest decrease of the absorbed energy appeared after tempering at $\sim$ 350 ℃ with resulting intergranular facets covering the fracture surfaces. Also, a similar grain size dependency as reported in [12] could be observed, i.e. larger grains yielding more embrittlement at the same conditions.

Grain boundary embrittlement as a result of thermal ageing will act as a non-hardening embrittlement since it, in general, does not impede dislocation motion, and gives rise to a fracture morphology with a large incidence of grain boundary facets. It also appears to have several commonalities with the phenomenon called reversible temper embrittlement [12,17]. The hardening effect that is typically observed in irradiated low alloy steels comes to a large extent from the formation of solute clusters, but also clusters of either interstitials or vacancies, during irradiation. The hardening effect is due to that the clusters act as obstacles to dislocation motion, thereby increasing the resistance to plastic flow. In the case of the weldments of most of the Swedish reactor pressure vessels, the irradiation induced solute clusters consist mainly of Mn, Ni, Si and Cu [18–20]. The formation of similar clusters in a thermally aged weld metal has also been observed by Lindgren et al. [21]. In that study, solute clusters are noted to have been formed preferentially on dislocations as observed by atom probe tomography (APT) and is related to the thermally ageing induced hardening of the weld metal. It should be noted that the weldment investigated in this study and the one investigated by Lindgren et al. were extracted from the same pressurizer but from different welds. However, both welds were manufactured with the same welding specifications. In other atom probe studies of thermally aged low alloy steels [22–25], solute clusters of similar composition as the ones in [21] were found, however these findings were not connected to any changes in mechanical properties.

The weld investigated in this study is a multi-layer weldment, which signifies that the weld is built up by several layers of weld beads. This gives rise to a complex microstructure where three distinct grain zones will emerge. These zones are:

I. the as-welded zone, consisting of elongated dendritic grains,
II. the once reheated zone, consisting of small equiaxed grains, and
III. the multiple reheated zone, also consisting of small equiaxed grains.

This will give rise to variations in several properties such as local chemistry, fracture toughness and other mechanical properties. An interesting study of the fracture toughness of multi-layer weldments was made by Viehrig et al. [26].

The main purpose of the testing conducted in this paper is to investigate the effects of thermal ageing on the brittle fracture toughness, and its effects on the influence of loss of constraint. Since ageing also may lead to weakened grain boundaries, it is also of interest to investigate to what extent this may contribute to the embrittlement. Thus, the core of this paper is an investigation of the fracture toughness of an in-service thermally aged weld metal from a Swedish nuclear power plant. This is compared to a reference material from a replaced reactor pressure vessel head, which has been in operation at a lower temperature than the pressurizer and where the effects of ageing therefore are considered minor. The study presents the results from an extensive experimental program where effects of ageing on the constraint sensitivity has been a focal point. Moreover, results from ductile fracture toughness testing, and tensile as well as hardness testing are presented along with an examination of the materials microstructure on the nano scale.

The outline of the paper is as follows: Section 2 presents the materials used in this study in terms of chemical composition, as-manufactured mechanical properties, along with the experimental set-up used. Section 3 presents the outcome of the experimental program including fractography and results from APT.

2. Materials and experiments

2.1. Materials

The thermally aged material investigated in this study has been extracted from the decommissioned and replaced pressurizer of the Ringhals unit 4 reactor. The pressurizer was manufactured by Uddcomb from plates of low alloy steel of the type A-533 Gr B Cl. 1 The weld metal comes from the circumferential weldment connecting the lower head to the first cylindrical structure of the pressurizer. The studied weld was manufactured using submerged-arc welding employing a weld wire with a low Cu – high Mn-Ni content,

Table 1
Chemical composition of the investigated weld metals from the manufacturing documentation.

Wt. %	C	Si	P	S	V	Cr	Mn	Co	Ni	Cu	Mo	Sn	Fe
R4PRZ	0.082	0.20	0.013	0.006	0.004	0.14	1.62	0.008	1.61	0.06	0.45	0.005	Bal.
R3RPVH	0.08	0.22	0.008	0.006	0.000	0.03	1.66	0.019	1.57	0.07	0.49	0.002	Bal.

Table 2
Check-in mechanical properties of the investigated weld metals.

	R_{p02}/MPa	T_{41J}/C
R4PRZ	579	−53
R3RPVH	575	−59

characteristic for all of the nuclear pressure vessels manufactured by Uddcomb. The measured chemical composition of the welding wire and flux combination can be found in Table 1. A post weld heat treatment was conducted for residual stress relief at 620 ℃ as part of the fabrication procedure. The pressurizer was in operation from 1983 to 2011, gathering a total of 215 000 h at an operating temperature of 345 ℃. The pressurizer was well insulated during its operation and consequently the temperature gradient through the thickness can be considered negligible. The results from check-in mechanical testing of the weld metal can be found in Table 2. The material from the pressurizer will henceforth be denoted as *R4PRZ*.

A reference material extracted from the replaced reactor pressure vessel head of Ringhals unit 3 was also included in the testing program for comparison purposes. This material was used in the investigation since there was no archive material available for the pressurizer. The reference material was chosen to have as similar Cu-Mn-Ni-Si content and check-in mechanical properties as the thermally aged weldment from the pressurizer as possible from the available material. The reactor pressure vessel head was manufactured from forgings of A-508Cl. 2 by Uddcomb and was welded using the same manufacturing specifications as the R4PRZ. The measured chemical composition of the reference material can be found in Table 1, and the check-in mechanical properties in Table 2. The reference material was in operation between 1981 and 2005 accumulating 176 000 h at 310–315 C. Preliminary testing (not presented here) showed that the effects of thermal ageing at this operating temperature were minor in comparison to those of the pressurizer. The reference material will be denoted as *R3RPVH* throughout this paper.

2.2. Fracture testing

The fracture toughness testing in the investigation of the constraint effect utilizes SEN(B)-specimens with the same overall dimensions but with different crack depth, deep for a state of high constraint and shallow for low constraint, for an illustration see Fig. 1. Also included in the study is a small, deeply cracked SEN(B)-specimen, serving as a reference. All specimens were extracted as T-S oriented with dimensions $W = \{30 \text{ and } 14\}$ mm, $B = \{15 \text{ and } 7\}$ mm, $a/W = \{0.5 \text{ and } 0.1\}$, and were manufactured such that the weld was centered in the specimen with base metal on each side. All specimens within the same dataset have been taken from the same depth of the weld metal with the purpose to have as similar weld microstructure in each specimen as possible. Thus, all the specimens with the same crack depth will have comparable microstructures. The specimens were placed in the weld to avoid the region close to the surface and the root of the weld. All specimens for investigation of the brittle fracture toughness were manufactured without side-grooves.

The testing for the brittle fracture toughness was conducted in accordance with ASTM E1921 [27], with the exception that the standard does not cover testing of specimens containing shallow cracks. The cracks were created using fatigue pre-cracking at room temperature according to the recommendations in E1921, which resulted in straight crack fronts in all specimens. When pre-cracking the shallow specimens, the crack length was estimated using a strain measurement technique. Testing was carried out in a computer-controlled cooling chamber utilizing liquid nitrogen to cool the specimen. The fracture toughness testing was carried out in displacement control with a loading rate corresponding to 1 MPa$\sqrt{\mathrm{m}}$/s during the initial elastic region of the test. The fracture toughness was evaluated from the load line displacement. The J-integral at failure was calculated from the load line displacement where the plastic η-factor valid for shallow cracks in SEN(B)-specimens was taken from Faleskog et al. [28].

The brittle fracture toughness results were interpreted by means of the master curve standard ASTM E1921 [27]. The ductile-to-brittle reference temperature T_0 was evaluated according to that standard. The master curve concept is based on a probabilistic weakest link model for brittle cleavage fracture assuming small-scale yielding conditions and self-similar crack tip fields [29]. The probability of failure at K_{Jc} is expressed by

$$P_f = 1 - exp\left(-\frac{B}{B_0}\left[\frac{K_{Jc} - K_{min}}{K_0 - K_{min}}\right]^4\right), \tag{1}$$

where B is the thickness of the specimen (or crack front width), B_0 is a reference thickness which is set to 1 T = 25.4 mm, $K_{\min}$ is a threshold fracture toughness, and $K_0 = K_0\,(T)$ is a temperature dependent reference fracture toughness that is referenced to 10 MPa $\sqrt{\mathrm{m}}$ for a 1 T specimen at T_0. More specifically, K_0 is well described by

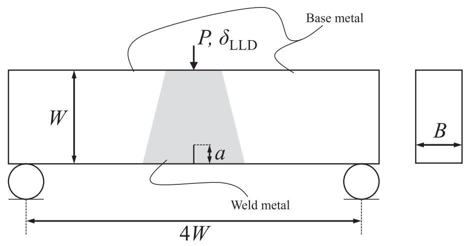

Fig. 1. Schematic illustration of a SEN(B)-specimen used in the experiments.

$$K_0 = 31 + 77exp(0.019[T - T_0])\ \ \mathrm{MPa}\sqrt{\mathrm{m}}. \tag{2}$$

For the master curve to give a good description of a materiaĺs brittle cleavage fracture toughness, the material itself needs to be homogeneous. In the case of a large degree of scatter due to material inhomogeneity, ASTM E1921 supplies additional methodology of T_0-evaluation so that a conservative estimate of the fracture toughness can be ensured. One example of such a method is the SINTAP-methodology [30], which now has been included in E1921, where an additional safety factor is included in the evaluation of T_0. Such methods may be needed in the evaluation of the fracture toughness of weld metals, where the scatter may be larger than that of more microstructurally homogeneous base metals. Another example is the case where the material displays a bimodal toughness distribution, where the bimodal master curve [31] can be utilized, which is expressed as

$$P_f = 1 - p_a exp\left(-\frac{B}{B_0}\left[\frac{K_{Jc} - K_{\min}}{K_0^A\left(T_0^A\right) - K_{\min}}\right]^4\right) - (1 - p_a)exp\left(-\frac{B}{B_0}\left[\frac{K_{Jc} - K_{\min}}{K_0^B\left(T_0^B\right) - K_{\min}}\right]^4\right). \tag{3}$$

The bimodal master curve requires three parameters that needs to be estimated, where ${T_0}^A$ and ${T_0}^B$ correspond to the reference temperature for each mechanism (mode in the distribution), respectively, and p_a is a probability scaling parameter that defines the contribution of each mechanism.

As the original master curve model is based on self-similar crack tip fields (small-scale yielding, high constraint), it is not capable of handling the effect of loss of constraint. In order to incorporate the effect of constraint, an empirical correction of T_0 by the T-stress is proposed by Wallin [32,33], as

$$T_0 = T_0^{\text{high constraint}} + \Delta T_0^{\text{constraint}},\ \text{where}\ \Delta T_0^{\text{constraint}} = A\frac{\Delta T_{\text{stress}}}{\sigma_y}. \tag{4}$$

Here, the difference in T-stress at the limit load between the predicted geometry and the geometry used to determine $\mathrm{T}_0^{\text{high constraint}}$ should be used, where $\mathrm{T}_0^{\text{high constraint}}$ normally is referred to as T_0, as the standard test method prescribes the use of deeply cracked specimens that produce a state of high constraint. In (4), the factor A is a yield strength dependent parameter that is empirically found to be approximately $\sigma_y/10$ MPa/K [32] for $\sigma_y > 600$ MPa and constant equal to 40 ℃ [33] when σ_y is below 600 MPa. It should be noted that the constraint correction of the master curve is still only partially developed for more complex geometries [34].

As the main purpose of this study is to investigate the sensitivity of the constraint effect on the fracture toughness of the thermally aged weld metal from the pressurizer and compare the results with the reference material available, a well-grounded approach is needed. An objective way to compare the constraint sensitivity of two materials is to choose the testing temperatures such that the median of the high constraint fracture toughness coincides. The next step is to conduct low constraint testing at the same temperatures, elucidating potential differences in the constraint effect on the fracture toughness between the two materials.

The testing was therefore conducted in the following steps:

i. Initial test series according to ASTM E1921 to find the reference temperature T_0 for the two materials
ii. use T_0 to determine temperatures where the high constraint fracture toughness will be the same for the two materials
iii. conduct remaining test series at the chosen temperature, high and low constraint as well as small specimens.

From the test results in step *i*, T_0 was evaluated to determine the testing temperatures to be used in step *iii*. The testing temperatures that would yield the same high constraint brittle fracture toughness was chosen to be −50 ℃ for R4PRZ and −90 ℃ for R3RPVH. Both materials were tested in series of 12 specimens in step *iii*.

Alongside the tests for the brittle fracture toughness, tests for the ductile fracture toughness were also conducted. These were carried out at a temperature of 75 ℃ to avoid brittle fracture altogether, i.e. clearly being on the upper shelf. The testing was performed with SEN(B)-specimens with side-grooves to promote uniform growth across the thickness of the specimens. The specimens for the ductile testing were extracted from the T-S orientation with dimensions $W = 30$ mm, $B = 15$ mm, $B_N = 12$ mm, and $a/W = 0.5$. The testing was conducted in accordance with ASTM E1820 [35]. The J-integral was calculated from the crack mouth opening displacement (CMOD).

2.3. Tensile and hardness testing

Uniaxial tensile testing was carried out on round bar specimens of both the weld and the base metal. In addition, hardness testing was performed on the weld metal, before and after heat treatments at 430 ℃ and 600 ℃, respectively. Note that different samples were used for the different temperatures. The hardness tests were performed to investigate the recovery of the ageing induced hardening during heat treatments. Hardness testing according to Vickers with an indentation load of 10 kgf was chosen as the test method. The specimens used were manufactured into blocks measuring 15 mm × 8 mm × 4 mm. An initial grid of indents was made to map out the initial hardness of the two materials, R4PRZ and R3RPVH, where the samples displayed a slight variation of hardness across the surface intended for measurement, as a result of the varying microstructure inherent to the weld. Hardness was also measured across and along the centerline of the weld in both materials.

2.4. Atom probe tomography

The nanostructure of the material has been investigated by APT, which was performed in a LEAP 3000X HR from Imago Scientific Instruments. From the results of the study in [21], it was expected that unevenly distributed Ni-Mn-Cu-Si rich clusters would be found. Due to this, large volumes, for APT, of material were analysed, and thus laser pulsing was used in addition to voltage pulsed analysis. However, laser pulsing affects the Si position due to surface diffusion [36] and thus both pulsing modes were used. For voltage pulsed analysis, a temperature of 50 K and pulse fraction of 20 % was used. For laser pulsed analysis, the temperature was 30 K and the laser energy 0.3 nJ. In both cases the laser pulse frequency was 200 kHz. The sample preparation was done using a standard two-step electropolishing method [37], finishing with millisecond pulsing to get rid of surface contamination. The reconstructions were made in the IVAS 3.6 software, using reconstruction parameters k between 4.0 and 5.3, and evaporation field of 33 V/nm in the case of voltage pulsed analysis and 23 V/nm for laser pulsed analysis. The image compression factor was set to 1.65 for all reconstructions.

The cluster analysis was performed using the maximum separation method (MSM) [38,39], a method that requires a careful choice of parameters in order to get relevant and comparable results [40,41]. Cluster parameters were chosen by comparing the data set to a randomised version and aiming to avoid defining random fluctuations in composition as clusters. Solute elements were chosen to be Cu, Ni, and Mn. The maximum solute atom distance in order for two atoms to be considered being in a cluster, d_{max}, was set to 0.45 nm, and the smallest number of solute atoms defining a cluster, N_{min}, was chosen to 20. Cluster sizes were determined by calculating the number of solute atoms in the clusters, assuming α-Fe body centred cubic structure and a detection efficiency of the LEAP of 37 %. The amount of Fe in the cluster is uncertain, since local magnification effects focus Fe atoms into the clusters during field evaporation [42,43]. Thus, the around 50 % Fe detected in clusters in these APT reconstructions is probably considerably lower in the actual material. Here, Fe was excluded from the clusters when calculating the size. This might give a slight underestimation if there is any Fe in the clusters. Cluster compositions were determined using MSM as well. For the number density, clusters on the edge of the analysis were identified and counted as half a cluster. It should be noted that the terms precipitate and cluster is used interchangeably in this paper, as the characterisation method (APT) does not give useful crystallographic information of the clusters.

3. Experimental results

3.1. Fracture toughness tests

In the evaluation of the reference temperature T_0, it was observed that the two materials behaved differently, which was due to the degree of inhomogeneity. The thermally aged R4PRZ displays a larger degree of inhomogeneity and has therefore been evaluated with

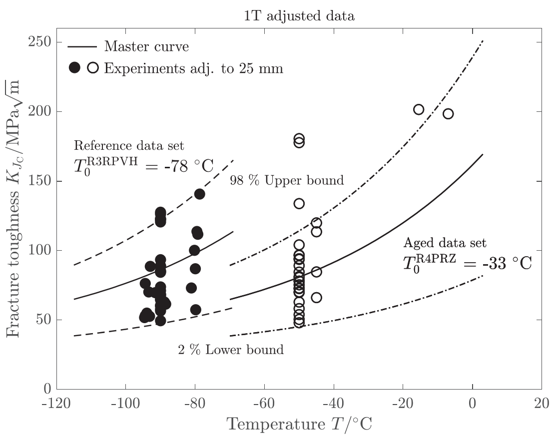

Fig. 2. Fracture toughness of individual specimens belonging to both R3RPVH and R4PRZ against testing temperature, and the predicted temperature dependence from the master curve model. Note that fracture toughness data for all deeply cracked specimens are presented in this figure.

the more conservative SINTAP-evaluation than that of the reference material R3RPVH, which was evaluated according to the normal procedure of E1921. The fracture toughness of deeply cracked specimens of both materials are shown as a function of testing temperature in Fig. 2 together with the master curve predictions based on the respective material's T_0. It is clear that the thermally aged R4PRZ is more brittle than R3RPVH, with a difference in T_0, $\Delta T_0 = 45$ ℃. Estimating the T_{41J} from the T_0 of R3RPVH by the empirical relation supplied in E1921 ($T_{41J} = T_0 + 24$ ℃) yields $T_{41J} = -54$ ℃, which agrees well with the check-in values for T_{41J} listed in Table 2, giving justification to using R3RPVH as a (fracture toughness) reference to R4PRZ.

By looking at the ranked probability of the single temperature tests, i.e. the constraint sensitivity tests, it appears that the R4PRZ displays a bimodal toughness distribution as seen in Fig. 3, while R3RPVH does not, as seen in Fig. 4. The rank probability is here

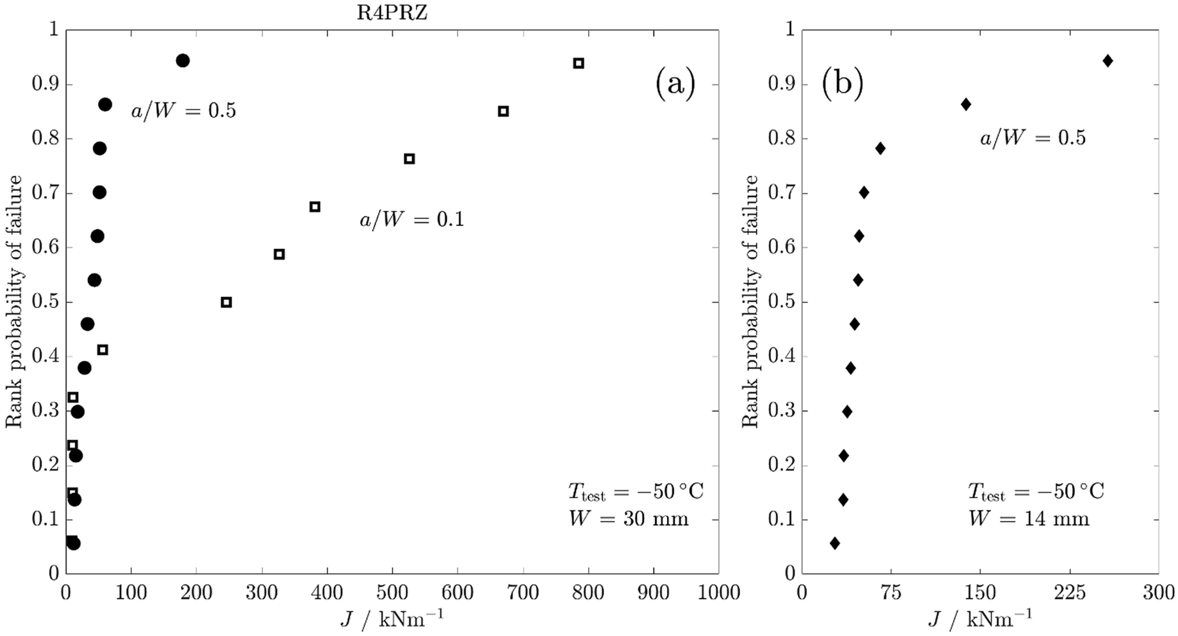

Fig. 3. Rank probabilities for the fracture tests of R4PRZ at the test temperature −50 ℃. (a) Data sets where $W = 30$ mm and $a/W = \{0.5, 0.1\}$. (b) Data set where $W = 14$ mm and $a/W = 0.5$.

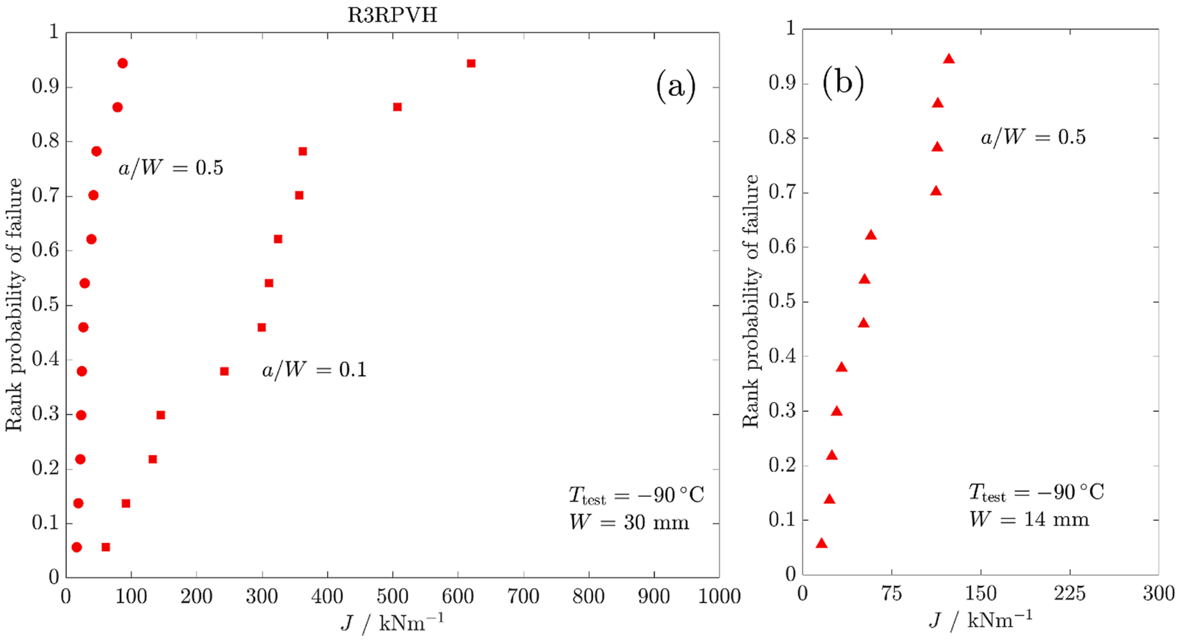

Fig. 4. Rank probabilities for the fracture tests of R3RPVH at the test temperature −90 ℃. (a) Data sets where $W = 30$ mm and $a/W = \{0.5, 0.1\}$. (b) Data set where $W = 14$ mm and $a/W = 0.5$.

computed as the median rank by Benard's approximation $P^i_{rank} \approx (i - 0.3)/(N + 0.4)$.

Especially noticeable is that the low constraint R4PRZ specimens ($a/W = 0.1$) behave very similar to the high constraint R4PRZ specimens ($a/W = 0.5$) at rank probability levels below 0.4, where the fracture toughness essentially coincides (Fig. 3). While at higher levels of rank probability, the low constraint R4PRZ specimens ($a/W = 0.1$) are subject to ductile crack growth up to 1 mm prior to brittle failure. Consequently, the scatter in fracture toughness, as expressed by the J-integral, becomes extreme and is found in the range 9.6 kN/m to 785 kN/m.

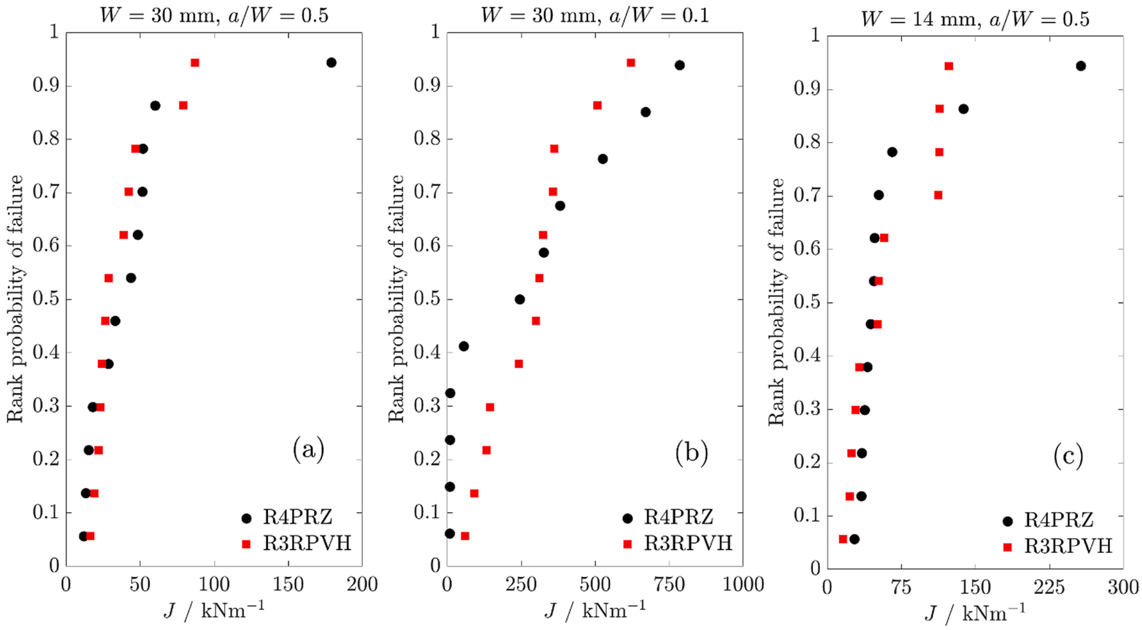

Fig. 5. Rank probabilities for the fracture tests of R4PRZ and R3RPVH for comparison of fracture toughness distribution. (a) Data set where $W = 30$ mm and $a/W = 0.5$. (b) Data set where $W = 30$ mm and $a/W = 0.1$. (c) Data set where $W = 14$ mm and $a/W = 0.5$.

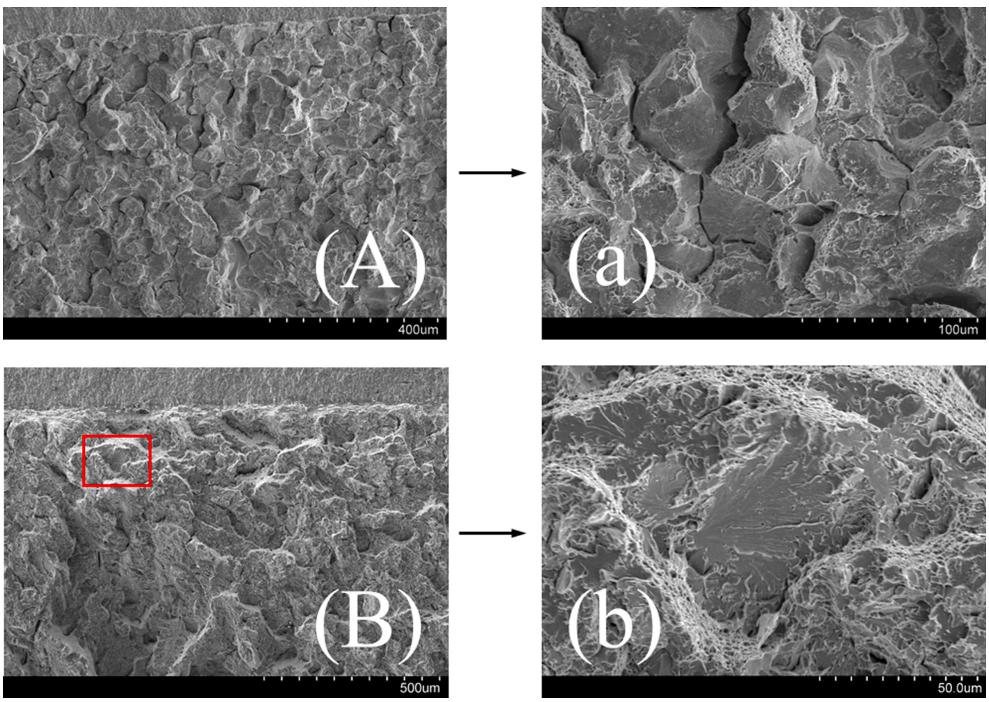

Fig. 6. Fractography of deeply cracked specimens ($a/W = 0.5$) from the R4PRZ data set. Specimen {(A), (a)} fractured at a *low* toughness of $K_{JC} = 52$ MPa$\sqrt{\text{m}}$, displays intergranular fracture, note secondary cracks in (a). Specimen {(B), (b)} fractured at a *higher* toughness of $K_{JC} = 108$ MPa$\sqrt{\text{m}}$, displays transgranular fracture, probable initation point in (b). The marked region in (B) shows where (b) is taken.

As seen in Fig. 5, the chosen temperatures for the constraint sensitivity tests were appropriate as the resulting fracture toughness distribution of the high constraint specimens (Fig. 5 a) shows a close similarity for both materials. In Fig. 5 (b), the low constraint results for both materials are compared, which clearly shows the difference between the thermally aged R4PRZ and the reference R3RPVH. In Fig. 5 (c), a comparison of the fracture toughness of the small specimens is shown, which aligns well, once again displaying the conformity of fracture toughness pertinent to high constraint geometries.

Fractography of the single temperature fracture tests presented in Fig. 3-Fig. 5 reveals that initiation of brittle fracture in the *low toughness specimens* from the thermally aged R4PRZ has occurred by grain boundary cracking. Here, the fracture surfaces are

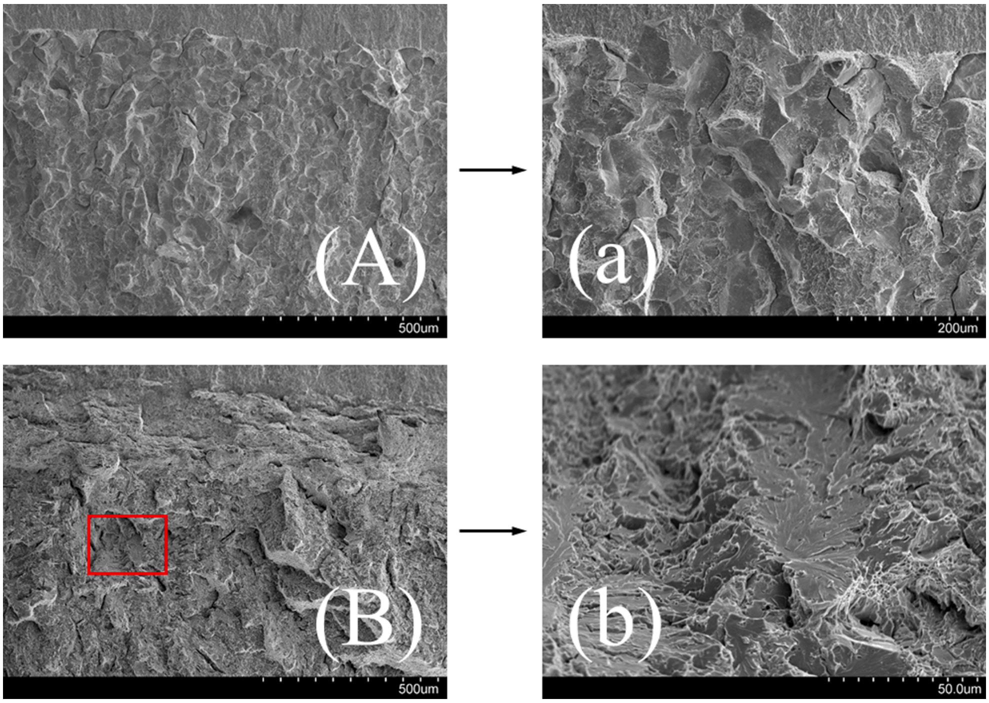

Fig. 7. Fractography of shallowly cracked specimens ($a/W = 0.1$) from the R4PRZ data set. Specimen {(A), (a)} fractured at a *low* toughness of $K_{JC} = 50$ MPa$\sqrt{\text{m}}$, displays intergranular fracture, note secondary cracks in (a). Specimen {(B), (b)} fractured at a *higher* toughness of $K_{JC} = 270$ MPa$\sqrt{\text{m}}$, displays transgranular fracture, probable initation point in (b). The marked region in (B) shows where (b) is taken.

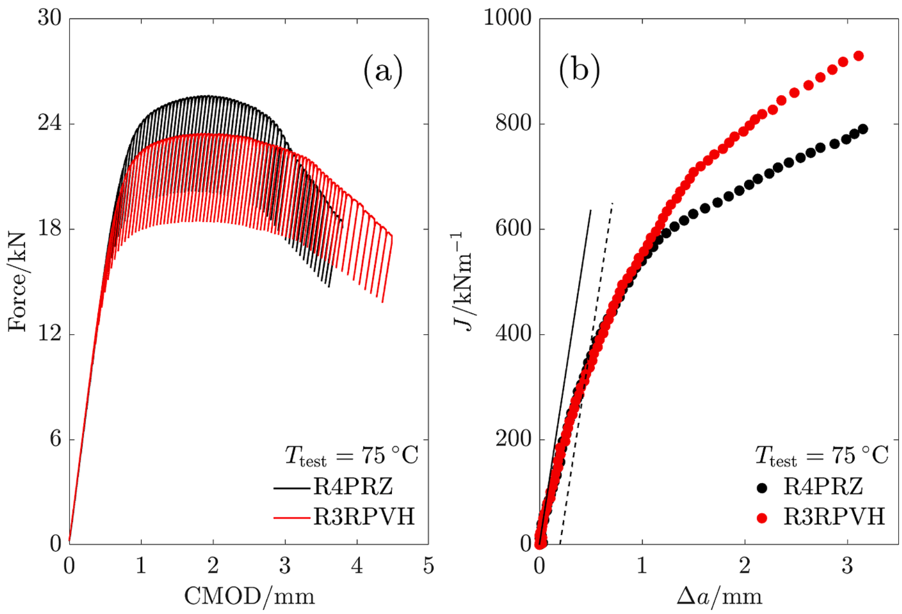

Fig. 8. Results from ductile fracture toughness testing. (a) Force-CMOD relation. (b) J-Δa relation.

consistently riddled with intergranular facets in direct connection to the crack front. This with no evidence of brittle fracture initiation from a second phase particle, as is commonly observed for cleavage fracture in ferritic steels. Observations of the *higher toughness specimens* unveil transgranular features and subsequently fracture initiation from second phase particles in tandem with intergranular features. For instance, low toughness brittle fracture appears to be solely associated with intergranular fracture while at higher levels of toughness, a mixture of both inter- and transgranular fracture appears to be the underlying cause of brittle fracture. Some examples of this is shown in Fig. 6 and Fig. 7 where low and high toughness specimens containing deep and shallow cracks are shown. For clarity, a low magnification image (uppercase) is associated with one of higher magnification (lowercase) per level of fracture toughness shown.

In the reference material R3RPVH, transgranular fracture is dominating the entire specimen population with few exceptions, where traces of intergranular fracture can be found in low toughness specimens. It should be noted that R3RPVH is not a perfect reference material, since it has been in operation during a significant number of years, however at a lower temperature and shorter time than R4PRZ.

The results from the ductile fracture toughness testing is shown in Fig. 8, where both the force-CMOD relation and the J_R-behavior for the two materials are shown. From these results it can be clearly distinguished that the ductile initiation fracture toughness $J_{IC} = 337$ kN/m is the same for both materials while the resistance to crack growth differs such that the thermally aged R4PRZ offers less resistance to crack growth after approximately 1 mm of growth.

3.2. Tensile and hardness tests

Fig. 9 shows a selection of the tensile tests that were carried out in this investigation. Fig. 9 (a) shows the tensile results at the testing temperatures pertinent to the constraint sensitivity fracture tests and it can be seen that the yield and ultimate tensile strength are virtually the same. Fig. 9 (b) displays the tensile results at room temperature, where it can be seen that the thermally aged R4PRZ appears to be slightly stronger than the reference R3RPVH. The tensile testing indicates that both materials are subjected to some hardening due to operation as the yield strength from the current investigation is higher than that of the check-in testing, a comparison is shown in Table 3.

The results from the Vickers hardness tests are shown in Fig. 10, where the hardness measured across and along the weld centerline in one of the R4PRZ and R3RPVH SEN(B)-specimens used for brittle fracture testing is plotted. It can clearly be seen that the hardness corresponds well with the results from the tensile tests in Fig. 9 for the two materials. For the hardness tests combined with heat treatments, annealing at 430 ℃ gave no change in hardness for times up to 50 h. However, annealing at 600 ℃ gave the results shown in

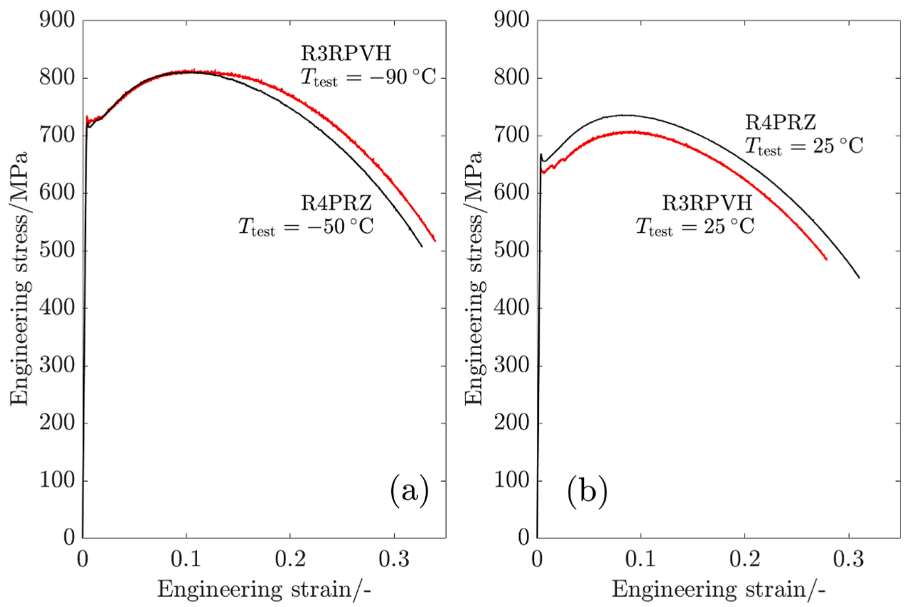

Fig. 9. Tensile tests of the weld metal of R4PRZ and R3RPVH. (a) At constraint sensitivity test temperatures. (b) At room temperature.

Table 3
Comparison between check-in yield strength and the results obtained in this investigation.

R_{p02}/MPa	Check-in	Current	Difference
R4PRZ	579	656	77
R3RPVH	575	637	62

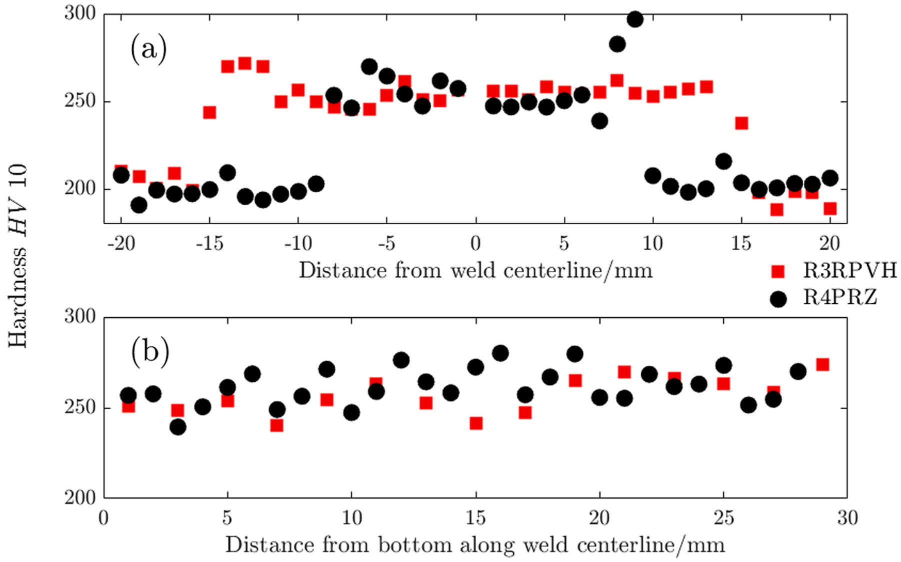

Fig. 10. Hardness measured on SEN(B)-specimens of R4PRZ and R3RPVH. (a) Shows the hardness across the weld centerline, from base metal to weld metal into base metal. (b) Shows the hardness along the weld centerline.

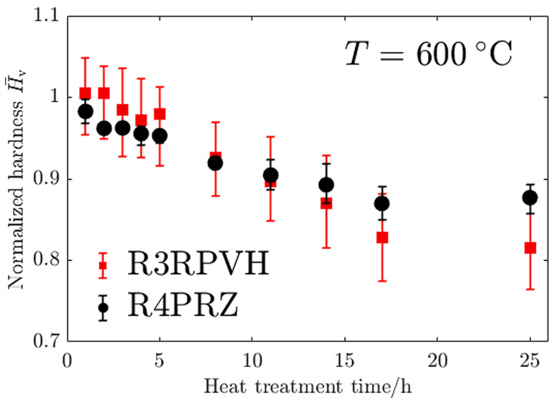

Fig. 11. Hardness of R4PRZ and R3RPVH against heat treatment time. Error bars represent the range in hardness measurement at each annealing.

Fig. 11, where normalized hardness is presented for both materials against annealing time. The error bars represent the range in hardness from the measurements after annealing. The initial hardness as defined by HV 10, of the specimens used in Fig. 11 can be represented by 248 and 254, which decreased to 220 and 213 after 25 h of annealing for R4PRZ and R3RPVH, respectively. It should be noted that a significant variability in hardness exists in the specimens, hence the wide range of the error bars.

3.3. Master curve analysis of single temperature fracture tests

By estimating the parameters of the bimodal master curve relevant to the single temperature fracture tests of R4PRZ, the results in Fig. 12 are obtained. When the three parameters are estimated for the high constraint specimen in Fig. 12 (a), it appears to give a consistent prediction of the size effect in Fig. 12 (c). However, there is no ambiguous way in which the bimodal master curve method can be constraint adjusted to reliably predict the experimental rank probabilities of the low constraint specimen in Fig. 12 (b). Therefore, the results presented in Fig. 12 (b) correspond to the low constraint specimen without corrections for loss of constraint. Furthermore, the bimodal master curve prediction in Fig. 12 (b) was based on a new set of parameters that were estimated to fit the experimental results shown in this graph. Thus, one set of bimodal parameters cannot be used to capture the experimental results of both the high and low constraint specimens displayed in Fig. 12. It should be noted that the master curve methodology, unimodal and bimodal, is based on self-similar crack tip fields related to a stationary crack, while the results in Fig. 12 (b) are subject to significant ductile crack growth prior to brittle failure. This will have an impact on the accuracy of the master curve with regards to parameter estimation and model predictions around and above the ductile initiation fracture toughness, $J_{IC} = 337$ kN/m, $K_{JC} = 272$ MPa $\sqrt{\text{m}}$.

In Fig. 13, master curve predictions of the probability of failure of the fracture tests of the reference material, R3RPVH are shown.

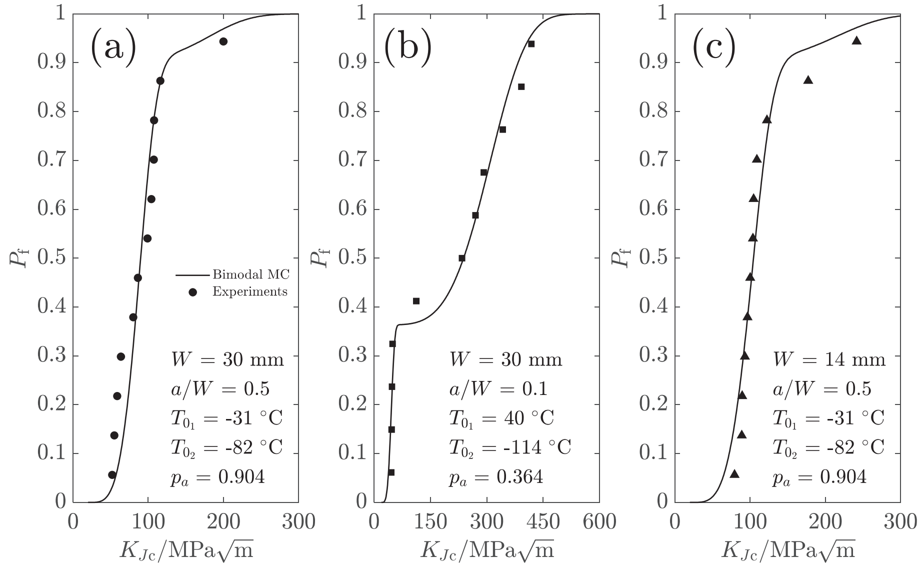

Fig. 12. Comparison of predicted failure probabilities (solid lines) from the bimodal master curve with rank probabilities for the experimental fracture tests pertaining to R4PRZ (symbols). (a) Data set where $W = 30$ mm and $a/W = 0.5$. (b) Data set where $W = 30$ mm and $a/W = 0.1$. (c) Data set where $W = 14$ mm and $a/W = 0.5$. Note, no constraint correction using e.g. T-stress has been used, the low constraint data has been used for both prediction and parameter estimation.

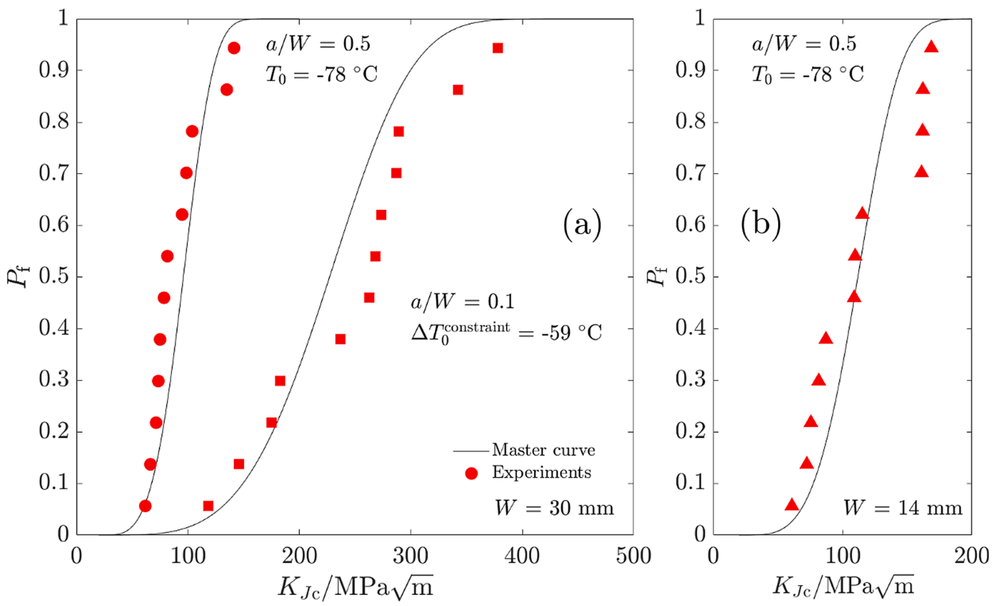

Fig. 13. Comparison of predicted failure probabilities (solid lines) from the (unimodal) master curve with rank probabilities for the experimental fracture tests pertaining to R3RPVH (symbols). (a) Data set where $W = 30$ mm and $a/W = 0.5$ and data set where $W = 30$ mm and $a/W = 0.1$. (b) Data set where $W = 14$ mm and $a/W = 0.5$. Note, T_0 has been subject to constraint correction using the T-stress for the low constraint specimens, $a/W = 0.1$ presented in (a).

Clearly, there is no need to use the bimodal master curve to describe the fracture toughness distribution of the reference material. The results presented in Fig. 13 (a) corresponding to the low constraint specimens ($a/W = 0.1$) are successfully constraint corrected using Eq. (4) where $A = \sigma_y / 10\,\mathrm{MPa/K}$.

3.4. Atom probe tomography

Regarding the results from the APT investigation, the measured chemical compositions of the matrix can be seen in Table 4. The

Table 4
Chemical matrix compositions as measured by APT. The standard deviation between different specimens is given as an estimate of the local variation in composition. N and S are omitted due to their overlaps with Si and O, respectively, in the APT spectrum.

At. %	R4PRZ	R3RPVH	Wt. %	R4PRZ	R3RPVH
C	0.03 ± 0.03	0.03 ± 0.01	C	0.01 ± 0.01	0.01 ± 0.01
Si	0.42 ± 0.09	0.47 ± 0.04	Si	0.21 ± 0.05	0.24 ± 0.02
P	0.02 ± 0.01	0.01 ± 0.01	P	0.01 ± 0.01	0.01 ± 0.01
V	0.004 ± 0.003	0.002 ± 0.001	V	0.004 ± 0.003	0.002 ± 0.001
Cr	0.13 ± 0.01	0.05 ± 0.01	Cr	0.12 ± 0.01	0.05 ± 0.01
Mn	1.33 ± 0.15	1.35 ± 0.07	Mn	1.31 ± 0.15	1.33 ± 0.07
Co	0.01 ± 0.01	0.02 ± 0.01	Co	0.01 ± 0.01	0.02 ± 0.01
Ni	1.69 ± 0.58	1.36 ± 0.08	Ni	1.78 ± 0.61	1.43 ± 0.08
Cu	0.05 ± 0.01	0.05 ± 0.01	Cu	0.06 ± 0.01	0.06 ± 0.01
Mo	0.12 ± 0.07	0.19 ± 0.07	Mo	0.21 ± 0.12	0.33 ± 0.12
Fe	Bal.	Bal.	Fe	Bal.	Bal.

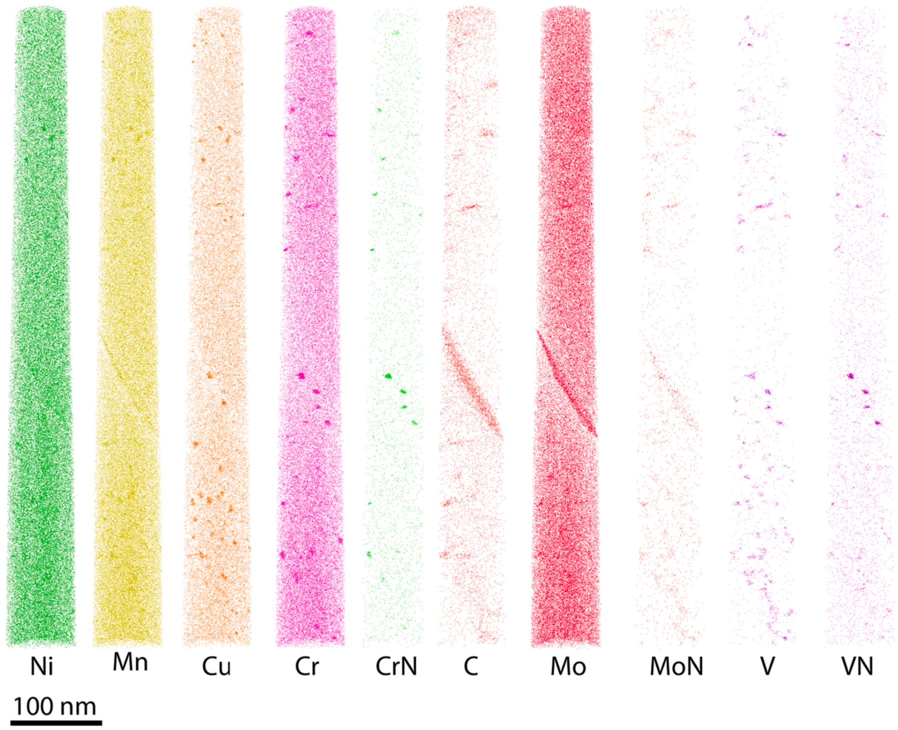

Fig. 14. APT reconstruction of thermally aged R4PRZ material. Only ions that are not randomly distributed are shown. This analysis was run in laser pulsed mode.

standard deviation between the different analyses of the same material is given, as APT is a local method and the welded material is chemically heterogeneous on the macroscopic scale. The average Ni content of the R4PRZ is slightly higher than that of R3RPVH. The average compositions are generally close to the nominal composition given in in Table 1. The low matrix concentration of C is expected as it is mainly present in carbides.

In the R4PRZ material, clusters were found using APT, see Fig. 14. The analyzed material was found to be heterogeneous; some of the smaller analyses did not contain any features whereas some contained many. Solute clusters containing Ni, Mn, Cu, and Si, were found in the reconstruction seen in Fig. 14. Some of these appear to have nucleated on very small carbonitrides. The carbonitrides contain V, Cr, Mo and some Mn, and some are found on dislocations, decorated with Mo, C, and Mn. As seen in the figure, not all carbonitrides contain all elements. The reconstruction in Fig. 14 also contain a boundary layer with Mo, C, some Ni, Si and Mn, and a few clusters/precipitates, out of which two appear to contain Cu and two do not.

A difficulty when analyzing the clusters and carbonitrides was the overlap in the mass spectrum at 32.5 Da. Both $^{65}Cu^{2+}$ and VN^{2+}

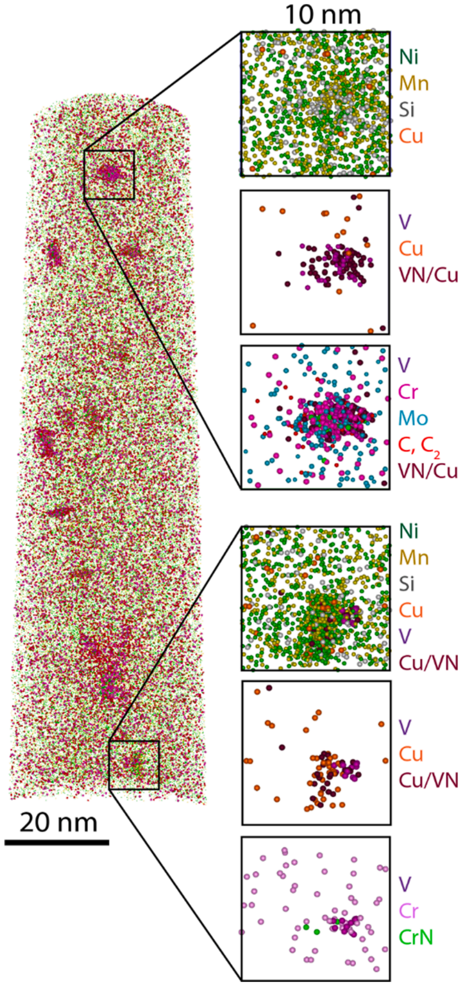

Fig. 15. Atom probe reconstruction of the thermally aged R4PRZ material. Two precipitates are cut out in boxes of $10 \times 10 \times 10\,\mathrm{nm}^3$, with different elements shown. The upper V and Cr-rich carbonitride does not contain any Ni or Cu, and only small amounts of Mn. The ions marked VN/Cu are mainly VN. The lower precipitate contains mainly Ni, and Mn, and some Cu. There is also some V in one part of the precipitate. Most of the Cu/VN ions are probably Cu. This analysis was run in voltage pulsed mode.

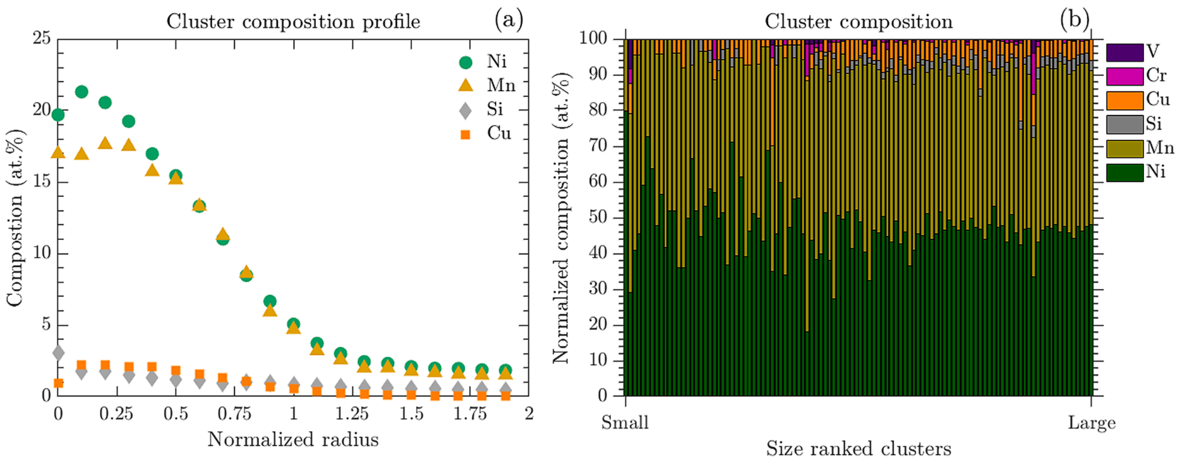

Fig. 16. The composition profile (a), and the cluster composition cluster by cluster (b), normalized by Fe in R4PRZ. The composition profile is not normalized in terms of composition, but the radius is. Zero corresponds to the cluster center, and unity to the edge of the cluster. The cluster composition cluster by cluster is sorted in increasing size.

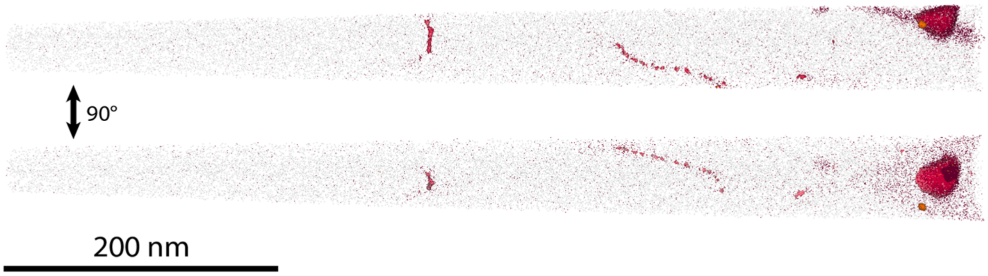

Fig. 17. APT reconstruction of the R3RPVH. Red *iso*-concentration surfaces correspond to Mo 1.9%, orange to Cu 1%, and brown dots are C atoms. A few dislocations are visible as well as a boundary layer containing a Mo-rich carbide and a small Cu-rich precipitate. The outline of the analysis is shown in grey. The reconstruction is turned 90°. (For interpretation of the references to colour in this figure legend, the reader is referred to the web version of this article.)

have peaks here in the voltage pulsed analyses. This was handled by using the peak at 31.5 Da to identify Cu^{2+} atoms, comparing with the local natural abundance of ^{65}Cu and ^{63}Cu. An example of this is shown in Fig. 15, where the upper precipitate is a carbonitride and the peak at 32.5 Da is mainly VN^{2+}. The 32.5 Da peak atoms then mainly coincide with the V atoms, whereas there are Cu atoms spread outside the carbonitride. In the lower cluster, that consists of mainly Ni, Mn, Si and Cu, the 32.5 Da peak is mainly $^{65}Cu^{2+}$, and the ions coincide with the $^{63}Cu^{2+}$ atoms at 31.5 Da. In laser pulsed runs the field is lower and thus most of the Cu evaporates as 1 + ions [44]. In this case, the overlap problem is less prominent as VN still evaporates as VN^{2+}.

In Fig. 16, the normalized composition profile and the individual cluster compositions of one analysis are shown. The clusters contain mainly Ni and Mn, and smaller amounts of Cu and Si. It was found that the cluster Cu content varied between the different analyses, and that the example in Fig. 16 is low in Cu. The clusters have similar composition within the same analysis. Many of the clusters contain some V or Cr. The average diameter of the Ni-Mn-rich clusters was also varying between the analyses, but the average was found to be 2.1 ± 0.3 nm, and the number density $1.3 \pm 0.5 \cdot 10^{22}$ /m^3.

The reference material from the RPVH of Ringhals R3, R3RPVH, was also analysed using APT. One reconstruction can be found in Fig. 17. In general, this material contained a lower density of small carbonitrides than the pressurizer. Still, some were found, and also Mo and C enriched dislocations, and boundaries. In Fig. 17 a Mo-rich carbide is sitting on a boundary.

Interestingly, occasional clusters containing Cu, Ni, and Mn were found in the R3RPVH material. In Fig. 17, one is present on the boundary layer. In other reconstructions, a few clusters were found on dislocations. The number density of the precipitates was very low, and they were not homogeneously distributed.

4. Discussion

The in-service thermal ageing of the pressurizer weld metal from Ringhals unit 4 appears to manifest through both hardening and non-hardening embrittlement mechanisms. That is, both by an increase in yield strength and by a weakening of the grain boundaries of the material. The effects of the embrittlement due to thermal ageing are profound in that they both give a significant change in the reference temperature T_0 and affects the fracture toughness distribution. As seen in Figs. 3-5 the comparison between the fracture toughness distributions of R4PRZ and R3RPVH reveals that there are some apparent differences at conditions that should be equal in terms of the high constraint fracture toughness. The most notable difference being that the low constraint specimens of R4PRZ shows a very wide range in the test data, where the most brittle specimens display fracture initiation through intergranular fracture and the tougher specimens appear to experience brittle fracture initiation from both grain boundaries and second phase particles, where the latter appears to bring out transgranular fracture features.

The toughness distribution of the R4PRZ appears to be bimodal where the bimodality has its origin in the multiple initiation mechanisms. This indicates that failure initiated from a grain boundary is weaker than that of failure initiated from a second phase particle in this material. The upper part of the distribution for the R4PRZ appears to be tougher than that of R3RPVH, which is likely an effect of ductile crack growth that occurs prior to the final brittle fracture. It is also important to note that the ductile crack growth that occurs prior to the final brittle failure will further pronounce the bimodality of the fracture toughness distribution. However, it is of the opinion of the authors that ductile crack growth alone cannot produce the effect that is seen in the fracture toughness results of the aged material. Clearly, it is the effect of multiple mechanisms acting to initiate brittle fracture that causes the bimodal fracture toughness distribution that acts concurrently with a ductile crack growth process.

For describing the toughness distribution of the thermally aged R4PRZ, the bimodal master curve is required and appears to be able to describe the material well under conditions of high constraint. The reference material R3RPVH is well described by the standard master curve, i.e. the *unimodal* model. However, the transition between the high and low constraint geometries is not trivial. For the case of R3RPVH, the correction of T_0 for the low constraint $a/W = 0.1$ appears to work well using Wallin's empirical relation [32]. But, a constraint correction for the bimodal master curve that ideally should be used to describe the R4PRZ is currently ambiguous due to the complex interactions of the initiation mechanisms and the number of parameters included in the model. A weakest link model capable of describing two brittle initiation mechanisms as well as predicting the size and constraint effect in a satisfactory manner has been proposed in Boåsen et al. [45].

Separating the effects from hardening and non-hardening contributions to the change in fracture toughness is not straight-forward. From the fractography of the thermally aged R4PRZ, the effects of non-hardening embrittlement can be distinguished from the presence of intergranular features. The hardening contribution was elucidated by the combination of hardness tests and heat treatments. From the measurements presented in Fig. 11, the hardness in both materials can be seen to decrease by 12–18 %, which is similar to the difference between the yield strengths obtained in the current investigation and the check-in data. It should also be noted that the decrease in hardness is to a level judged to be relevant to the as-manufactured hardness of the weld. This implies that there is a hardening effect present in both the R4PRZ and the R3RPVH materials, i.e. hardening due to thermal ageing at the operating temperatures.

Concerning the ductile fracture tests presented in Fig. 8, the fracture toughness plotted against crack growth aligns well for crack growth up to ~ 1 mm, thereafter it deviates so that the R4PRZ has less resistance than R3RPVH. This is accompanied with a change in fracture surface appearance where the morphology changes notably. A possible explanation would be that the crack grows into a different part of the microstructure, which presents different requisites for void growth and coalescence, the main operating mechanism for ductile crack growth in these materials. As an example, if the crack starts growing in a zone with a reheated microstructure (small equiaxed grains), it is likely that the ductile fracture resistance will change once the crack grows into an as-welded zone (elongated dendritic grains), or vice versa.

The obvious material to compare the APT-results of the R4PRZ material with is the pressurizer weld analysed by APT in [21] and [46]. This weld comes from the very same component, but a different weld that is slightly different in terms of composition. The clusters containing Cu, Ni, Mn, and Si are relatively similar in appearance. The Cu content is higher in the clusters reported in [21] and [46], but the measured Cu content is also higher in that weld (0.10 at. % compared to the 0.05 at. % in the weld in this paper). The lower Cu content makes the core–shell structure (Cu-rich core) less prominent in the clusters here. The cluster size and number density of the two studies of pressurizer welds are within the estimated errors considering the heterogeneous distribution.

As mentioned earlier, the terms cluster and precipitate are used interchangeably in this paper, as APT does not provide enough crystallographic information to reveal the crystal structure of these small clusters/precipitates. Generally, bcc Cu-clusters in α-Fe are believed to transform into 9R precipitates when they have a diameter of at least around 4 nm, and into fcc at larger sizes [47,48]. Here, the Ni and Mn content of the clusters is high, and thus the question is what type of precipitate is formed, and at which diameter.

The most significant difference from the other weld of the same pressurizer is the amount of small carbonitrides. In the other material, occasional V and Cr-containing carbonitrides were found. They were also found in the reference material used in that paper and in the Ringhals RPV weld metal [20]. It is assumed that the carbonitrides are present before ageing and are thus not affecting the shift of mechanical properties in a direct way. They appear to act as nucleation point for the Ni-Mn-rich clusters, as many of them are found in connection to each other (see Figs. 14-16). The higher number of carbonitrides does, however, not seem to give a significant increase in the number of Ni-Mn-Si-Cu clusters as the number density of $1.3\ 10^{22}\ /m^3$ here is close and within the uncertainty of the $1.6\ 10^{22}\ /m^3$ measured in [21]. Also, there are carbonitrides where Cu, Ni, Mn and Si have not precipitated/clustered, see Figs. 14 and 15.

The fact that Ni-Mn-Cu-Si clusters could be found in the R3RPVH material that was used as reference material is interesting. Such clusters were not found in similar un-aged reference materials used by the authors in similar high Ni and Mn, low Cu weld metals [21,20]. Despite the diffusion of these elements in α-Fe being very slow at the relevant temperature (310–315 °C), some clustering still seems to be possible, although to a very limited degree.

5. Conclusions

The effects of embrittlement due to thermal ageing on the weldments from a pressurizer of a Swedish nuclear power plant, more specifically the effect of ageing on the constraint sensitivity of the fracture toughness has been investigated and compared to a reference material. Testing revealed a $\Delta T_0 = 45\ ^{\circ}C$ between the materials, indicating a significant embrittlement. The thermally aged material displays a bimodal fracture toughness distribution, which is pronounced at low constraint, and is due to brittle fracture being initiated from weakened grain boundaries as well as second phase particles. To describe the fracture toughness distribution, the bimodal master curve is needed and no constraint correction for the low constraint specimens can unambiguously be made. The reference material is well described by the unimodal master curve and the constraint effect is well predicted within the same framework.

The nanostructure of both materials is characterized using atom probe tomography. In-homogeneously distributed solute clusters of Ni-Mn-Cu-Si situated on dislocations and on carbonitrides, which are also present within the material, were observed.

A hardening due to thermal ageing is apparent in both the studied materials. It is investigated using uniaxial tensile tests as well as hardness tests in combination with heat treatments. After annealing at 600 ℃ for 25 h it appears that the ageing induced hardening is restored, most likely due to dissolution of solute clusters formed due to thermal ageing.

CRediT authorship contribution statement

Magnus Boåsen: Conceptualization, Data curation, Formal analysis, Investigation, Methodology, Project administration, Software, Visualization, Validation, Writing – original draft, Writing – review & editing. **Kristina Lindgren:** Conceptualization, Formal analysis, Investigation, Methodology, Software, Visualization, Writing – original draft, Writing – review & editing. **Martin Öberg:** Methodology, Resources, Software, Supervision, Writing – review & editing. **Mattias Thuvander:** Conceptualization, Methodology, Resources, Supervision, Writing – original draft, Writing – review & editing, Funding acquisition. **Jonas Faleskog:** Conceptualization, Investigation, Methodology, Supervision, Writing – original draft, Writing – review & editing. **Pål Efsing:** Conceptualization, Funding acquisition, Investigation, Methodology, Project administration, Resources, Supervision, Writing – original draft, Writing – review & editing.

Declaration of Competing Interest

The authors declare that they have no known competing financial interests or personal relationships that could have appeared to influence the work reported in this paper.

Acknowledgements

The Swedish Radiation Safety Authority (SSM) and the Swedish Centre for Nuclear Technology (SKC) are acknowledged for their financial support. Ringhals AB is acknowledged for supplying the material that was used in the experimental investigation. Jenny Roudén at Ringhals AB is greatly acknowledged for her support in this study and for constructive comments on the manuscript. The APT was performed at the Chalmers Materials Analysis Laboratory (CMAL).

References

[1] Debarberis L, Acosta B, Zeman A, Pirfo S, Moretto P, Chernobaeva A, et al. Ductile-to-brittle transition temperature of thermally segregated WWER-1000 base metal. Int J Microstruct Mater Prop 2007;2(3/4):326. https://doi.org/10.1504/IJMMP.2007.015312.
[2] Gurovich BA, Chernobaeva AA, Yu Erak D, Kuleshova EA, Zhurko DA, Papina VB, et al. Chemical composition effect on VVER-1000 RPV weld metal thermal ageing. J Nucl Mater 2015;465:540–9.
[3] A. A. Chernobaeva, E. A. Kuleshova, B. A. Gurovich, D. Yu Erak, O. O. Zabusov, D. A. Maltsev, D. A. Zhurko, V. B. Papina and M. A. Skundin, "Thermal ageing effects of VVER-1000 weld metal under operation temperature," in *Fontevraud 8*, Avignon, 2014.
[4] Shtrombakh YI, Gurovich BA, Kuleshova EA, Maltsev DA, Fedotova SV, Chernobaeva AA. Thermal ageing mechanisms of VVER-1000 reactor pressure vessel steels. J Nucl Mater 2014;452(1-3):348–58.
[5] Joly P, Roch F, Primault C. Effect of thermal ageing on properties of pressure vessel low alloy steel. Proceedings of the ASME 2013 Pressure Vessels and Piping Conference. 2013.
[6] Pelli R, Forstén J. Effect of thermal ageing on impact ductility of the nuclear pressure vessel steel SA533B and its weld metal. Theor Appl Fract Mech 1987;8:25–31.
[7] Kameda J, Nishiyama Y. Combined effects of phosphorus segregation and partial intergranular fracture on the ductile-brittle transition temperature in structural alloy steels. Mater Sci Engng, A 2001;528:3705–13.
[8] Andrieu A, Pineau A, Joly P, Roch F, Ryckelynck D. Influence of P and C intergranular segregation during manufacturing and ageing on the fracture toughness of nuclear pressure vessel steels. Procedia Mater Sci 2014;3:655–60.
[9] S. G. Druce, G. Gage and J. G., "Effect of ageing on properties of pressure vessel steels," *Acta Metallurgica,* vol. 34, no. 4, pp. 641-652, 1986.
[10] Vatter IA, Hippsley CA, Druce SG. Review of Thermal Ageing Data and its Application to Operating Reactor Pressure Vessels. Int J Press Vessels Pip 1993;54(1-2):31–48.
[11] Naudin C, Frund JM, Pineau A. Intergranular fracture stress and phosphorus grain boundary segregation of a Mn-Ni-Mo steel. Scr Mater 1999;40(9):1013–9.
[12] Briant CL, Banerji SK. Intergranular failure in steel: the role of grain boundary composition. Int Metal Rev 1978;23(1):164–99.
[13] McMahon CJ. Intergranular Fracture in Steels. Mater Sci Eng 1976;25:233–9.
[14] Guttmann M. Equilibrium segregation in a ternary solution: a model for temper embrittlement. Surf Sci 1975;53(1):213–27.
[15] Guttmann M. Temper Embrittlement and Ternary Equilibrium Segregation. Mater Sci Eng 1980;42:227–32.
[16] Banerji SK, McMahon CJ, Feng HC. Intergranular Fracture in 4340-Type Steels: Effects of Impurities and Hydrogen. Metall Trans A 1978;9(2):237–47.
[17] Stein DF. Reversible temper embrittlement. Annu Rev Mater Res 1977;7(1):123–53.
[18] Miller MK, Powers KA, Nanstad RK, Efsing P. Atom probe tomography characterizations of high nickel, low copper surveillance RPV welds irradiated to high fluences. J Nucl Mater 2013;437(1-3):107–15.
[19] Styman PD, Hyde JM, Parfitt D, Wilford K, Burke MG, English CA, et al. Post-irradiation annealing of Ni-Mn-Si-enriched clusters in a neutron-irradiated RPV steel weld using Atom Probe Tomography. J Nucl Mater 2015;459:127–34.
[20] Lindgren K, Boåsen M, Stiller K, Efsing P, Thuvander M. Evolution of precipitation in reactor pressure vessel steel welds under neutron irradiation. J Nucl Mater 2017;488:222–30.
[21] Lindgren K, Boåsen M, Stiller K, Efsing P, Thuvander M. Cluster formation in in-service thermally aged pressurizer welds. J Nucl Mater 2018;504:23–8.
[22] Hyde JM, Sha G, Marquis EA, Morley A, Wilford KB, Williams TJ. A comparison of the structure of solute clusters formed during thermal ageing and irradiation. Ultramicroscopy 2011;111(6):664–71.
[23] Styman PD, Hyde JM, Wilford K, Morley A, Smith GDW. Precipitation in long term thermally aged high copper, high nickel model RPV steel welds. Prog Nucl Energy 2012;57:86–92.
[24] Styman PD, Hyde JM, Wilford K, Smith GDW. Quantitative methods for the APT analysis of thermally aged RPV steels. Ultramicroscopy 2013;132:258–64.
[25] Styman PD, Hyde JM, Wilford K, Parfitt D, Riddle N, Smith GDW. Characterisation of interfacial segregation to Cu-enriched precipitates in two thermally aged reactor pressure weld steels. Ultramicroscopy 2015;159:292–8.
[26] Viehrig H-W, Houska M, Kalkhof D, Schindler H-J. Fracture mechanics characterisation of reactor pressure vessel multi-layer weld metal. Int J Press Vessels Pip 2015;135-136:36–51.
[27] ASTM International, "E1921 Standard Test Method for Determination of Reference Temperature, T0, for Ferritic Steels in the Transition Range," ASTM International, West Conshohocken, 2019.
[28] Faleskog J, Kroon M, Öberg H. A probabilistic model for cleavage fracture with a length scale - parameter estimation and predictions of stationary crack experiments. Engng Fract Mech 2004;71(1):57–79.
[29] Wallin K. The scatter in KIC-results. Engng Fract Mech 1984;19(6):1085–93.
[30] Pisarski HG, Wallin K. The SINTAP fracture toughness estimation procedure. Engng Fract Mech 2000;67(6):613–24.
[31] Wallin K, Nevasmaa P, Laukkanen A, Planman T. Master Curve analysis of inhomogeneous ferritic steels. Engng Fract Mech 2004;71:2329–46.
[32] Wallin K. Quantifying T-stress controlled constaint by the master curve transition temperature T0. Engng Fract Mech 2001;68:303–28.
[33] Wallin K. Fracture Tougness of Engineering Materials - Estimation and Application. Croydon: EMAS Publishing; 2011.
[34] Boåsen M, Stec M, Efsing P, Faleskog J. A generalized probabilistic model for cleavage fracture with a length scale - Influence of stress state and application to surface cracked experiments. Engng Fract Mech 2019;214:590–608.
[35] ASTM International, "E1820 Standard Test Method for Measurement of Fracture Toughness," ASTM International, West Conshohocken, 2019.
[36] Hyde JM, Burke MG, Gault B, Saxey DW, Styman P, Wilford KB, et al. Atom probe tomography of reactor pressure vessel steels: an analysis of data integrity. Ultramicroscopy 2011;111(6):676–82.
[37] Miller MK. Atom Probe Tomography: Analysis at the Atomic Level. Academic/Plenum Publishers 2000;200.

[38] Hyde JM, English CA. "An Analysis of the Structure of Irradiation induced Cu-enriched Clusters in Low and High Nickel Welds," in *Materials Research Society Symposium*. Boston 2000;650. https://doi.org/10.1557/PROC-650-R6.6.

[39] Vaumousse D, Cerezo A, Warren PJ. A procedure for quantification of precipitate microstructures from three-dimensional atom probe data. Ultramicroscopy 2003;95:215–21.

[40] Dong Y, Etienne A, Frolov A, Fedotova S, Fujii K, Fukuya K, et al. Atom Probe Tomography Interlaboratory Study on Clustering Analysis in Experimental Data Using the Maximum Separation Distance Approach. Microsc Microanal 2019;25(2):356–66.

[41] Lindgren K, Stiller K, Efsing P, Thuvander M. On the Analysis of Clustering in an Irradiated Low Alloy Reactor Pressure Vessel Steel Weld. Microsc Microanal 2017;23(2):376–84.

[42] Marquis EA, Hyde JM. Applications of atom-probe tomography to the characterization of solute behaviours. Mater Sci Eng R Rep 2010;69(4–5):37–62.

[43] Edmondson PD, Parish CM, Nanstad RK. Using complimentary microscopy methods to examine Ni-Mn-Si-precipitates in highly-irradiated reactor pressure vessel steels. Acta Mater 2017;134:31–9.

[44] Kingham DR. The Post-Ionization of Field Evaporated Ions: a Theoretical explanation of Multiple Charged States. Surf Sci 1982;116:273–301.

[45] Boåsen M, Dahlberg CFO, Efsing P, Faleskog J. A weakest link model for multiple mechanism brittle fracture - Model development and application. J Mech Phys Solids 2021;147:104224.

[46] K. Lindgren, M. Boåsen, K. Stiller, P. Efsing and M. Thuvander, "Thermal ageing of low alloy steel weldments from a Swedish nuclear power plant - the evolution of the microstructure," in *Fontevraud 9*, Avignon, 2018.

[47] Deschamps A, Militzer M, Poole WJ. Comparison of Precipitiation Kinetics and Strengthening in an Fe-0.8%Cu Alloy and a 0.8% Cu-containing Low-carbon Steel. ISIJ Int 2003;43:1826–32.

[48] Othen PJ, Jenkins ML, Smith GDW. High-resolution electron microscopy studies of the studies of the structure of Cu precipitates in α-Fe. Philos Mag A 1994;70:1–24.

Journal of Nuclear Materials 569 (2022) 153925

Contents lists available at ScienceDirect

Journal of Nuclear Materials

journal homepage: www.elsevier.com/locate/jnucmat

Brittle fracture initiation in decommissioned boiling water reactor pressure vessel head weld

Zaiqing Que[a,*], Matti Lindroos[b,*], Jari Lydman[a], Noora Hytönen[a], Sebastian Lindqvist[a], Pål Efsing[c], Pekka Nevasmaa[a], Pentti Arffman[a]

[a] Nuclear Reactor Materials, VTT Technical Research Centre of Finland, Espoo 02044, Finland
[b] Integrated Computational Materials Engineering, VTT Technical Research Centre of Finland, Tampere 33720, Finland
[c] Department of Solid Mechanics, Royal Institute of Technology (KTH), Stockholm SE-100 44, Sweden

ARTICLE INFO

Article history:
Received 11 May 2022
Revised 8 July 2022
Accepted 17 July 2022
Available online 18 July 2022

Keywords:
Brittle fracture
Initiation
Reactor pressure vessel
Weld metal
Inclusion
Toughness

ABSTRACT

The brittle fracture initiation behavior and fracture toughness in the ductile-to-brittle transition region for a thermally-aged weld metal of a decommissioned reactor pressure vessel head (in operation at 288 °C for 23 effective full power years) and in the non-aged reference condition were investigated. The results show that brittle fracture initiated primarily from non-metallic inclusions. The correlation between fracture toughness and brittle fracture initiation type (inclusion debonding or breakage), initiator size, initiation location (as-welded or re-heated regions in the weld metal) were analysed. Despite that thermal ageing does not affect significantly the fracture toughness, it could promote the debonding as a brittle fracture primary initiation type. The influence of debonded inclusion on the evolution of cumulative damage and brittle fracture initiation was assessed using crystal plasticity modelling.

1. Introduction

The structural integrity of the reactor pressure vessel (RPV) is of utmost importance for safety and long-term operation in a nuclear power plant (NPP) [1]. During operation, the RPV is subjected to neutron irradiation and thermal aging, which can result in materials embrittlement and elevate the ductile-to-brittle transition temperature (DBTT) [2–9].

There have been extensive investigations on the weld embrittlement resulted from thermal aging and/or irradiation [10,11]. Thermal aging of a high-Ni and high-Mn weld metal (WM) in a pressurizer for 24.6 years operation at 345 °C was reported to cause an increase in DBTT [7], clustering [12] and intergranular (IG) fracture [7]. Segregation of solute elements to grain boundaries (GBs) with co-segregation process involving Cr, Ni, C, Mn, Mo and P was observed in thermally-aged RPV steel weld [13]. High bulk Ni content can encourage the formation of clusters during thermal aging, which have higher Cu and lower Ni, Mn and Si contents than the clusters found in irradiation-induced clusters [5,14,15].

In terms of embrittlement, WMs are normally considered as more critical than base materials (BM) [6], which is due to the higher density of non-metallic inclusions and lower cohesive strength of boundaries resulted from the higher level of GB segregation in WM compared to BM [11]. WMs are typically composed of a large amount of homogeneously distributed round inclusions, which are different from the BMs where the inclusions are more irregular in shape and less densely populated. Consequently, the probability of an inclusion suitable for initiating a brittle fracture is higher in WMs than in BMs [16]. Typically, the oxygen content in arc weld metals, such as submerged arc welding (SAW) WM, can be even a magnitude higher than in BM, which favours the formation of non-metallic inclusions in WM. McMahon and Cohen [17] reported that the cracking of cementite particles located at ferrite GBs represents a primary cleavage initiation mechanism for BMs whereas non-metallic inclusions are the main cleavage initiators for WMs [18]. Hein et al. [19] had similar observations that inclusions were the primary initiators in RPV WMs. Oh et al. [20] found that the fracture toughness was inversely proportional to the square root of the triggering inclusion diameter. However, the specimens investigated were from the whole transition curve instead of basing the assessment on fracture toughness specimens from the ductile-to-brittle transition region where initiation of brittle fracture occurs after some ductile deformation. A systematic investigation on the type, location and chemical composition of the brittle fracture primary initiators in the weld metal is still pending.

* Corresponding authors.
E-mail addresses: zaiqing.que@vtt.fi (Z. Que), matti.lindroos@vtt.fi (M. Lindroos).

https://doi.org/10.1016/j.jnucmat.2022.153925

The presence of inclusions have a significant influence on the initiation of brittle cleavage crack [21]. A microcrack of brittle fracture can initiate within a brittle particle resulted from plastic straining of the matrix surrounding the particle and propagate from the broken particle [22] or initiate at the interface between secondary particles and matrix due to debonding [23]. These modes were further referred to as inclusion cracking, inclusion-assisted cracking and inclusion decohesion by Miao and Knott [24]. A nucleated microcrack must grow to a critical size and overcome microstructural barriers such as GBs to develop into a cleavage crack with self-sustained growth subject to a high enough exterior stress beyond a sufficiently large area around the nucleation site [25]. Since a large inherent scatter is a natural part of brittle fracture, probabilistic modelling, e.g., the weakest link model is often used to describe its behavior [26,27]. However, metallurgical and microstructural data of brittle fracture initiators in real NPP component, e.g., decommissioned RPV, is required for an improved mechanistic understanding of brittle fracture.

This work aims for enhancing the comprehension of the factors affecting brittle fracture initiation by fracture toughness testing, materials characterisation and modelling of a high-Ni WM of a decommissioned boiling water reactor RPV head (RPVH). The WM is investigated in thermally-aged and reference conditions.

2. Experimental

2.1. Materials

The studied RPVH WM was harvested from the decommissioned Barsebäck Unit 2 boiling water reactor, which was in operation at 288 °C for 23 effective full power years. Barsebäck Unit 2 RPV non-irradiated non-aged state WM from the surveillance program was studied as reference material. The same type of WM has been used in several reactors [6,28]. The circumferential weld was used to join forged material (SA 508 Cl. 2) on the top and plate material (SA 533 Gr. B Cl. 1) at the lower side (Fig. 1(a)). The RPV was manufactured by Uddcomb AB, and has been post weld heat treated [29]. Trepans for tests and characterisations were drilled from the RPVH weld. The inner surface stainless steel cladding was removed before transportation of the trepans to VTT. The RPVH WM is only subjected to thermal aging but not to neutron irradiation. The investigated WM was mainly welded using SAW process with a filler material of Phoenix-Union S3NiMo with high Ni and Mn contents and low Cu content [30]. The chemical compositions of the thermally-aged RPVH WM and non-aged reference WM are presented in Table 1.

2.2. Specimens and tests

Tensile test, Charpy V-notch (CVN) impact toughness test and compact tension (C(T)) fracture toughness based T0 testing were performed. All three types of specimens were machined from a one-quarter depth from the inner surface of RPVH trepan and were fabricated in the orientation TS, which corresponds with the reference non-aged WM specimens in the Barsebäck Unit 2 surveillance program. The tensile testing with flat miniature tensile specimens was performed in accordance to ISO 6892-1 with a constant displacement rate of 0.12 mm/min at room temperature. CVN impact toughness specimens with the size of 55 mm × 10 mm × 10 mm were tested according to the standard SFS-EN ISO-148-1:2016. Miniature C(T) specimens were manufactured from the tested CVN specimens. As shown in Fig. 1(a, b), 4 miniature C(T) specimens were manufactured from 1 CVN specimen (two from each half) and in total 20 miniature C(T) specimens from RPVH WM were manufactured and tested between −114.4 and −129.9 °C (with fracture toughness values between 51.7 and 259.8 MPa$\sqrt{}$m) for the Master curve analysis according to ASTM E1921. 11 miniature C(T) specimens of reference non-aged state were tested between −110 and −140 °C.

2.3. Materials characterisation

The metallography specimens were fine polished and etched with 3 vol% Nital solution (HNO_3 + ethanol). The weld solidification microstructure were characterised using the Zeiss Axio Observer 7 inverted light optical microscope. Reprography images were taken with Olympus OM-D E-M1 Mark II camera. Microhardness of HV1 and HV0.3 was measured using a Struers DuraScan-80 device.

A Zeiss Crossbeam 540 scanning electron microscope (SEM) equipped with EDAX Hikari Plus electron backscatter diffraction (EBSD) detector and EDAX Octane Plus Energy dispersive X-ray spectroscopy (EDS) detector was used. EBSD mapping was conducted at an accelerating voltage of 15 kV, a working distance of 14 mm and a probe current of 1.5 nA. EBSD inversed pole figure (IPF) images were analysed by TSL OIM Analysis 8 software. EDS was performed with 10−15 keV and a current density of 1.5 nA.

2.4. Modelling

A micromorphic crystal plasticity model was used to investigate the microstructural level deformation and damage behavior of the WM. Lindroos et al. described the model background in Ref. [31], in which strain gradient like micromorphic extension is used to provide scale dependent plasticity and damage behavior for martensitic steels. In the current work, micromorphic regularisation is placed on plasticity alone to control slip localisation that also affects the damage process by introducing *microslip* approach. Furthermore, previous work with micromorphic models [32,33] have been dedicated to regularise damage growth in different materials with so-called *microdamage* approach, while the objective of these models was not to apply strain gradient plasticity. Other recent approaches have focused on introducing length-scale plasticity and also its effects on ductile damage [34,35]. The present work focuses on investigating the effect of small non-metallic inclusions to the damage susceptibility within ferritic microstructures and therefore the use of scale dependent framework is supported. The following presents the key contents of the current model.

Finite strain multiplicative decomposition of the deformation gradient was employed to the elastic and inelastic contributions. Inelastic contribution considers plastic deformation by dislocation slip and damage systems. First part of this section presents the dislocation slip model and the second part focuses on the damage extension.

$$\underset{\sim}{F} = \underset{\sim}{F}^E \cdot \underset{\sim}{F}^{IN} = \underset{\sim}{E} \cdot \underset{\sim}{P} \tag{1}$$

The inelastic velocity gradient is then written as:

$$\dot{\underset{\sim}{P}} \cdot \underset{\sim}{P}^{-1} = \underset{\sim}{L}^P + \underset{\sim}{L}^D \tag{2}$$

Table 1
Chemical composition of studied weld metals according to optical emission spectrometry (wt.%).

Element	C	Si	Mn	P	S	Cr	Mo	Ni	Cu	Co	Al
RPVH SAW weld	0.057	0.15	1.43	0.008	0.007	0.03	0.41	1.48	0.060	0.020	0.024
Reference weld	0.084	0.22	1.53	0.011	0.004	0.13	0.44	1.47	0.064	0.008	0.005

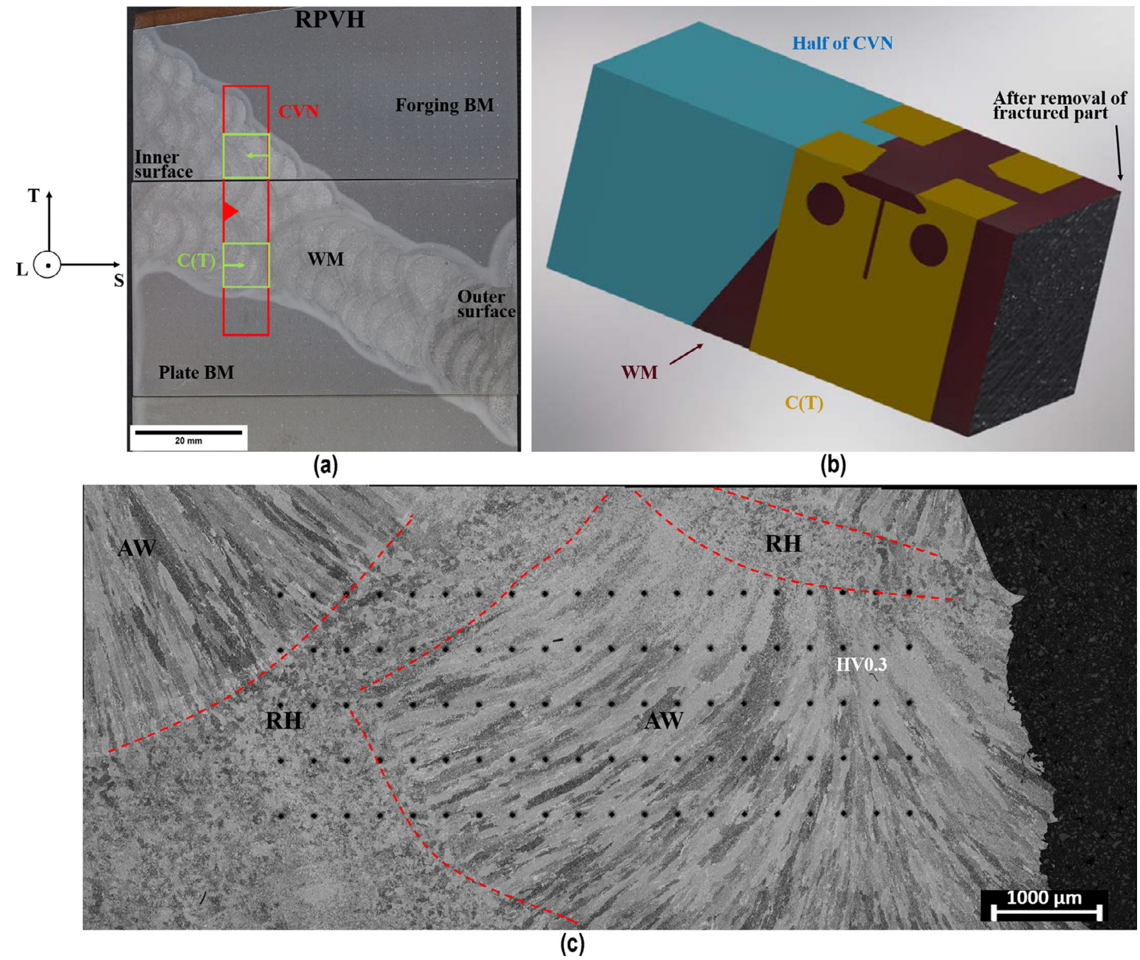

Fig. 1. (a) The WM was used to join the plate BM and forging BM in RPVH. The inner surface of RPVH was on the left side. (b) Two C(T) specimens were fabricated from one half of tested CVN specimen. (c) A micro-etched specimen prepared from the cross section of a tested CVN specimen showing WM microstructure includes AW and RH zones. Indentations of HV0.3 are seen as black dots.

Plastic deformation is carried over by dislocation slip. Total of 24 slip systems are included for BCC crystal, involving slip families {110}<111> and {112}<111> with both 12 slip systems. Plastic velocity gradient is:

$$\underline{L}^P = \sum_{s=1}^{N_s=24} \dot{\gamma}^s \underline{N}^s \tag{3}$$

where $\dot{\gamma}^s$ is the slip rate of a slip system s, and $\underline{N}^s$ is an orientation tensor. A visco-plastic slip rate is used:

$$\dot{\gamma}^s = \left\langle \frac{|\tau^s| - (R^s - S_\chi)}{K} \right\rangle^N sign(\tau^s) \tag{4}$$

where τ^s is the resolved shear stress on slip systems, R^s is the isotropic hardening of each system. K and N describe viscosity and strain rate dependency of the model. A micromorphic model extension involving a generalised stress term S_χ is introduced to accomplish length-scale dependent plasticity and therefore indirectly also a link to damage following works of Lindroos et al. [31,36]. In detail, a *microslip* variable is introduced with γ_χ as an additional degree of freedom. The model resembles a strain-gradient approach, whenever the penalisation parameters related to the micromorphic model is chosen accordingly. The effective flow rule f^s can be written using this framework by:

$$f^s = |\tau^s| - (R^s - S_\chi) = |\tau^s| - (R^s - A\, Div\big(Grad\ \gamma_\chi\big)) \\ = |\tau^s| - (R^s - A\, \Delta_\chi \gamma_\chi)) \tag{5}$$

in which *microslip* γ_χ is related to cumulative plastic slip $\gamma_{cum} = \int_0^t \sum_{s=1}^{N_s=24} |\gamma^s| dt$ with a regularisation equation:

$$\gamma_\chi - \frac{A}{H_\chi} \Delta_\chi \gamma_\chi = \gamma_{cum} \tag{6}$$

where A is a higher order modulus and H_χ is a penalisation modulus, and Δ_χ is Lagrangian-Laplace type operator. The generalised stress term then affects slip activity and modifies a standard crystal plasticity approach.

The isotropic hardening is written as a sum of initial slip resistance τ_0 and the dislocation interaction part.

$$R^s = \tau_0 + Q \sum_{s=1}^{N_s=24} H_{rs}\{1 - \exp(-b\nu^r)\} + H\beta^2\nu + H\beta d \tag{7}$$

where Q describes the magnitude of the hardening, H_{rs} is the interaction matrix between slip systems taken from Hoc and Forest [37], and b defines saturation of hardening. Again, the cumulative slip is tracked with $\nu^s = \int_0^t |\dot{\gamma}^s| dt$ and the total cumulative slip ν is summed over all slip systems. Total cumulative plastic slip of the slip systems is denoted by $\nu^{s/r}$. Coupling between plasticity and damage is performed with a parameter β and cumulative damage is denoted by d and will be defined in later section. The damage coupling terms include a self-softening term as well as a term that depends on the amount of damage coming from the free energy function suggested in Sabnis et al. [33] and Lindroos et al. [38].

A damage model is introduced with a modification to the previous works [31–33,38], where inelastic damage occurs by crystalline cleavage planes. Cleavage planes of type [100] are considered for the present BCC material. The main inelastic deformation mechanism in the model is the opening of the [100] cleavage planes and accommodation shear mechanisms operating on the same plane. Damage rate is constructed of the opening (mode I), and shear systems (modes II and III).

$$\underline{L}^D = \sum_{a=1}^{N_{\mathrm{damage}}} \dot{\delta}_c^a n_d^a \otimes n_d^a + \dot{\delta}_1^a n_a^a \otimes l_{d1}^a + \dot{\delta}_2^a n_2^a \otimes l_{d_2}^a \tag{8}$$

where $\dot{\delta}_c^a, \dot{\delta}_1^a, \dot{\delta}_2^a$ are the strain rates of opening and shear systems of each damage plane, n_d^a is a normal vector to the plane and l_{d1}^a, l_{d2}^a are in-plane accommodation along shear directions. The cumulative damage strain d is computed as the sum of absolute strains generated by each opening and shear damage system.

Damage related strain rates are operated with a similar Norton type of flow rule.

$$\dot{\delta}_c^a = \left(\frac{\left| n_d^a \cdot \underline{I}^M \cdot n_d^a \right| - Y_c^a}{K_d} \right)^{N_d} sign\left(n_d^a \cdot \underline{\Pi}^M \cdot n_d^a \right) \tag{9}$$

$$\dot{\delta}_l^a = \left(\frac{\left| n_d^a \cdot \underline{M}^M \cdot l_{di}^a \right| - Y_i^a}{K_d} \right)^{N_d} sign\left(l_{di}^a \cdot \underline{\Pi}^M \cdot l_{di}^a \right), \text{ with } i = 1, 2 \tag{10}$$

where K_d and N_d are material parameters, $\underline{\Pi}^M$ is Mandel stress in the reference configuration, and Y_c^a, Y_i^a are damage criteria. No additional micromorphic variable is placed to regularise damage growth in this work due to that the use of a single micromorphic variable for both plasticity and damage can be too restrictive [31]. The damage criteria is given as:

$$Y_c^a = Y_i^a = \sigma_d^0 + H_{soft} d \; + \; H_{soft} \beta \nu \tag{11}$$

where σ_d^0 is the initial cleavage/damage resistance. The damage resistance is decreased by accumulation of damage. In addition, it is assumed that slip localisation makes the material more prone to damage and thus coupling with plasticity is used, whenever plastic slip accumulates. The value for the softening modulus H_{soft} is negative. A constraint is placed for both slip resistance R^s and damage resistances Y_c^a and Y_i^a to remain positive as the accumulation of damage can lead to negative values. The model is implemented to Zset finite element solver. Non-metallic aluminium oxide inclusions are included in the simulations, however, they are treated as elastic domains for simplicity with Young's modulus of 380 GPa and Poisson's ratio of 0.25.

3. Results

3.1. Baseline characterisations of thermally-aged RPVH

EBSD mappings of the RPVH WM are shown in Fig. 2. It is noteworthy to mention that the main microstructural features of the RPVH WM and the non-aged reference WM are very similar. The weld consists of as-welded (AW) and re-heated (RH) regions. In the WM, intragranular acicular ferrite with a fine basket weave structure is the dominant microstructural phase in dendritic AW region zones, as shown in Fig. 2(a). The acicular ferrite has the length of 4, 5 times of the width with ∼1 to 2 μm. In addition to acicular ferrite, the AW dendrites also consist of a small fraction of pro-eutectoid GB ferrite, Widmanstätten ferrite side plates and polygonal ferrite (Fig. 2(b)). Pro-eutectoid GB ferrite appears at the dendritic boundaries.

The main microstructure of the RH zones is polygonal ferrite, as shown in Fig. 2(c, d). The prior austenite grain size in the RH zone is ∼120 μm length with 60 μm width. The polygonal ferritic microstructural boundaries is of 12 μm length with 3 μm width. Compared to the AW zones, the solidification boundaries and ferritic microstructural boundaries in RH zones tend to become more granular. No Widmanstätten ferrite side plates are present in the RH zone. Acicular ferrite is observed occasionally in RH zones. A summary of microstructures in WM is shown in Table 2.

3.2. Comparison study of thermally-aged RPVH and non-aged reference WMs

3.2.1. Mechanical properties

The comparison of mechanical properties of the decommissioned thermally-aged RPVH and non-aged reference WMs is shown in Table 3. The results of T_0 fracture toughness tests, CVN impact toughness tests and tensile tests of these two materials exhibit similar mechanical properties.

HV0.3 microhardness was measured from cross-sections of 7 and 4 CVN specimens of the decommissioned thermally-aged RPVH and non-aged reference WMs, respectively. The microhardness matrix included 100 indentations per specimen. After etching, the locations of indentations in different microstructures were identified (Fig. 1(c)). There were no significant hardness variation in the AW and RH microstructures. The summary of microhardness is presented in Table 4. The average microhardness in the WM of decommissioned thermally-aged RPVH was 214 ± 8 HV0.3 in AW and 216 ± 8 HV0.3 in RH microstructures, respectively. The average microhardness in the WM of the non-aged reference material was 209 ± 5 HV0.3 in AW and 208 ± 4 HV0.3 in RH microstructures, respectively. The mechanical test results suggest a minor (statistically insignificant) thermal embrittlement effect on the mechanical properties of the WM.

3.2.2. C(T) specimens primary initiator study

Based on ASTM E1921, the weld has a tendency to behave as a macroscopically inhomogeneous material. In this paper, though, the T_0 is estimated based on standard Master curve assessment to get an indication of the transition temperature. The T_0 temperature determined by the miniature C(T) testing of RPVH WM is −113 °C, which differs by −15 °C from the non-aged reference material condition. The brittle fracture in all the 20 miniature C(T) specimens of RPVH WM initiated from a particle with size between 0.3 and 1.8 μm. 13 out of 20 of the specimens primarily initiated from a debonded particle while the rest 7 initiated from a broken inclusion particle. Table 5 summarises the primary initiator type (as a debonded or broken particle) and the initiation location (in AW or RH microstructures). The percentage of debonded particles as primary initiating particles is higher than broken particles and there seems to be more brittle primary initiation from AW than RH regions. For the reference non-aged WM, the fractographic investigations and the determination of the primary initiation sites were performed for 11 miniature C(T) specimens. All the specimens with a determinable initiator have the brittle fracture primarily initiated from broken inclusion particles with sizes between 0.6 and 1.8 μm. As revealed by the cross-sectional metallography, 5 of the 11 primary initiation sites were found in AW microstructure and the rest in RH region.

The primary initiation site of brittle cleavage fracture can be determined based on the characteristic river patterns. For the thermally-aged RPVH WM, the fractographic examinations of two representative C(T) specimens where brittle fracture primarily initiated from a debonded particle and a broken inclusion particle are shown in Figs. 3 and 4, respectively. The specimen in Fig. 3 was tested at −128.3 °C with a fracture toughness of 81.0 MPa$\sqrt{\text{m}}$. A cross-sectional metallographic specimen right below the primary

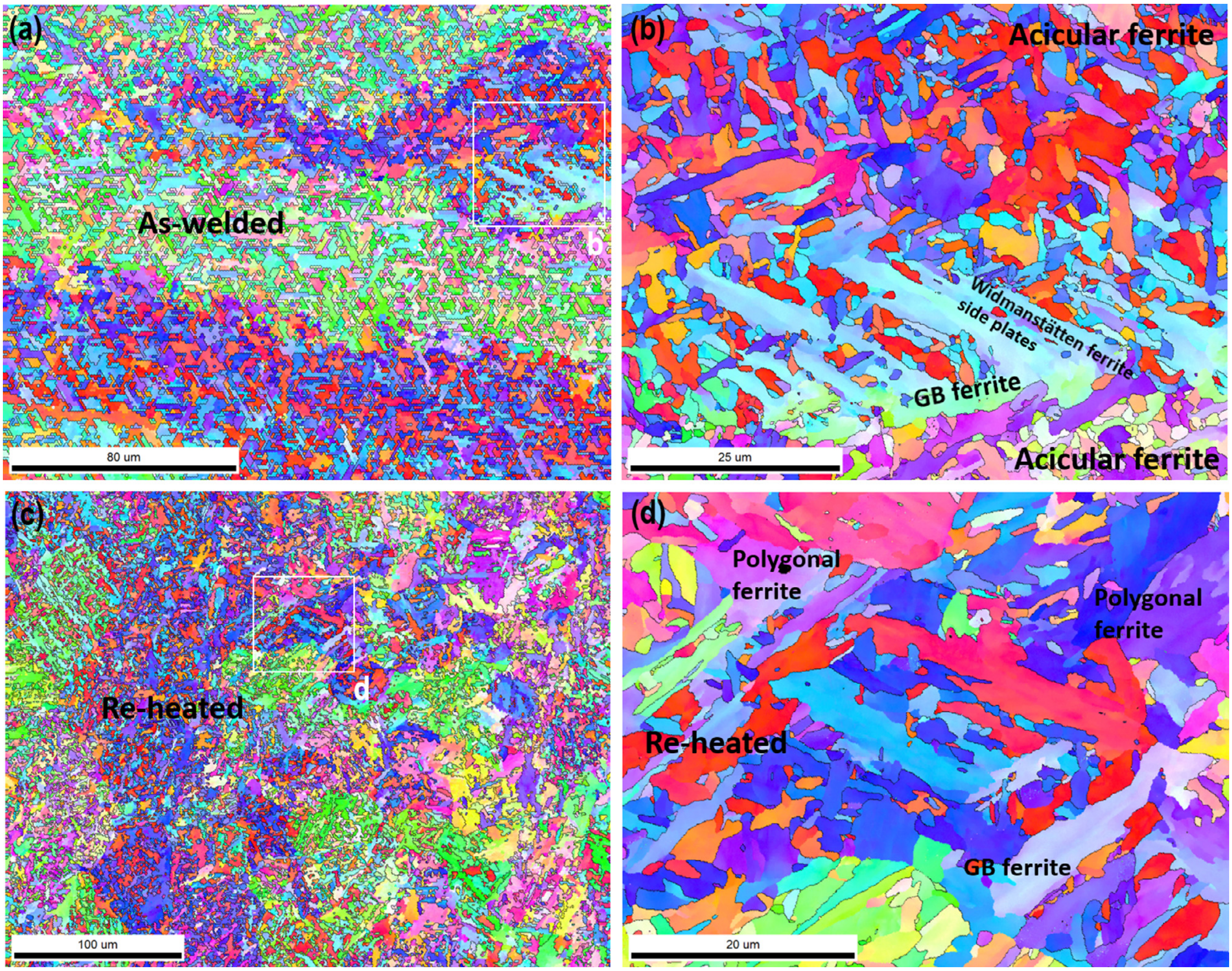

Fig. 2. EBSD mapping of (a, b) AW region and (c, d) RH region of thermally-aged RPVH material.

Table 2
Summary of grain size in various microstructures of thermally-aged RPVH material.

Microstructures	Phases or features	Grain size (μm)
As-welded	Dendritic boundary	1 mm length with 45 μm width
	Acicular ferritic GB	8–10 μm length with 1–2 μm width
Re-heated	Prior austenite GB	120 μm length with 60 μm width
	Polygonal ferritic GB	12 μm length with 3 μm width

Table 3
Mechanical properties of WMs from the decommissioned RPVH and the non-aged reference material.

	Toughness		Tensile test			
Materials	T_0 °C	T_{41J} °C	Yield stress MPa	Tensile stress MPa	Fracture strain %	Reduction of area %
Decommissioned RPVH WM	−113	−75	562.2	627.5	19.5	72
Non-aged reference WM	−98	−73	560	642	20	73.2

Table 4
Microhardness HV1 and HV0.3 of AW and RH zones from the decommissioned RPVH and the non-aged reference material.

Materials	Microstructures		HV1	HV0.3
Decommissioned RPVH	WM	AW	227 ± 5	214 ± 8
		RH		216 ± 8
Non-aged reference material	WM	AW	213 ± 3	209 ± 5
		RH		208 ± 4

initiation site was prepared by electric discharge machining as marked by the red arrow in Fig. 3(a). As shown in Fig. 3(b, c), the brittle fracture initiated from the GB ferrite in the AW microstructure. The crack growth generally follows the macroscopic microstructure of the AW dendritic boundaries and the angle between the local weld bead direction and the crack plane is ~10°. The debonded primary initiator remained on the fracture surface of specimen half A (Fig. 3(d–f)) and on the mating fracture sur-

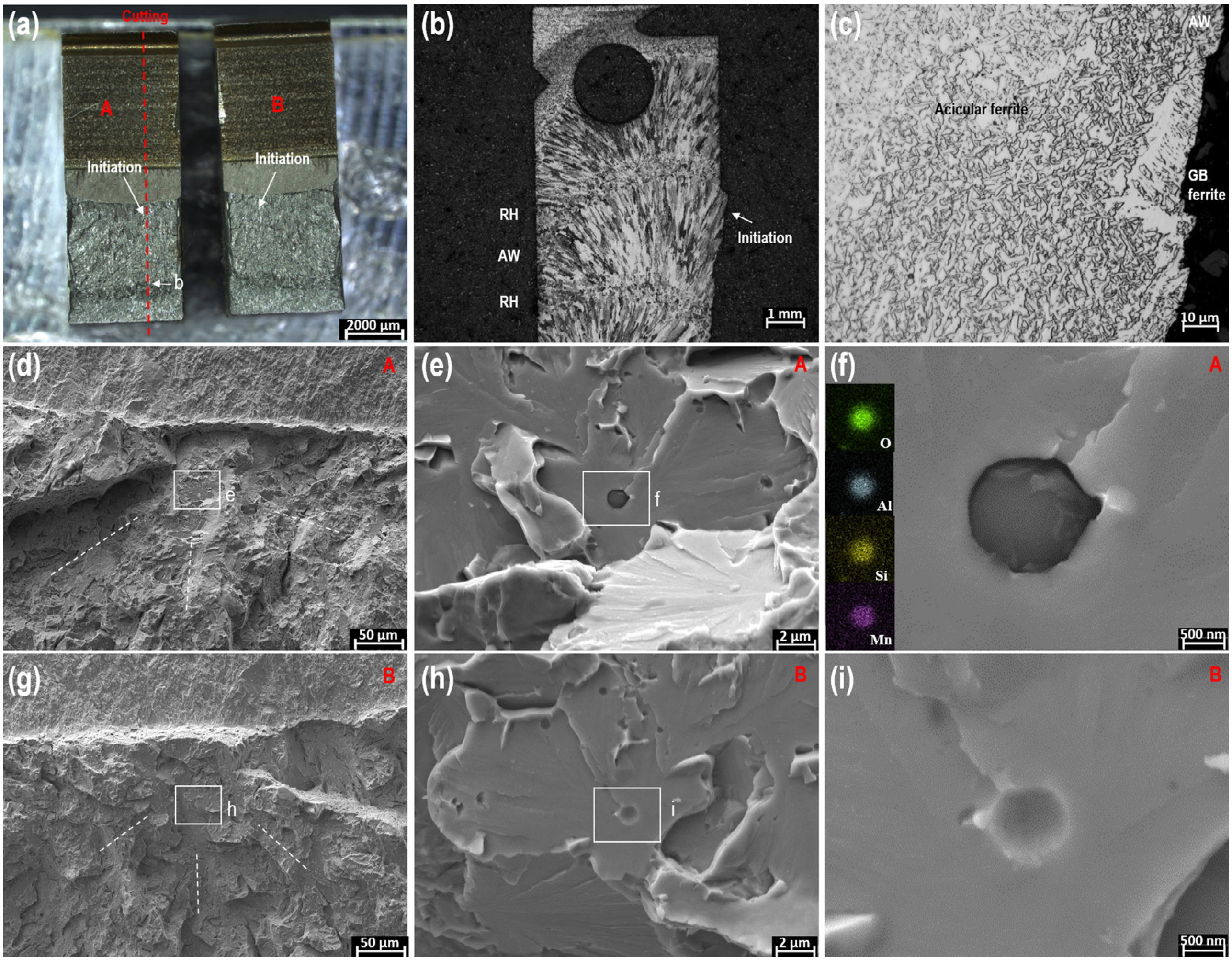

Fig. 3. (a) Parts A and B of a representative miniature C(T) specimen of the thermally-aged RPVH material (tested at −128.3 °C with fracture toughness of 81.0 MPa$\sqrt{m}$) showing the primary initiation site and the electric discharge machining cutting line. (b, c) Cross section reveals that the primary initiation locates in the AW microstructure. SEM images of primary initiation site of specimen half A (d–f) and half B (g–i). The brittle fracture initiated from a debonded inclusion.

Table 5
Summary of distribution of debonded and broken particles as the brittle fracture primary initiating particles in T0 testing C(T) specimens in AW or RH microstructures of investigated WMs.

Material	Brittle fracture primary initiation type	AW	RH
Thermally-aged RPVH	Debonded particle	8	5
WM	Broken particle	4	3
Non-aged reference	Debonded particle	0	0
material	Broken particle	5	6

face of half B there is a dent and only some traces of the particle (Fig. 3(g–i)). The primary initiation site is characterised by an Al-, Si-, Mn-rich oxide particle (with trace elements of Ti and Mg) with a size of 1.0 µm. In Fig. 4, the specimen was also tested at −128.3 °C but with a fracture toughness of 123.9 MPa$\sqrt{m}$. As shown in Fig. 4(b, c), the primary initiation site locates in the RH microstructure. The initiator particle was broken and found located in both of the specimen halves (Fig. 4(d–i)). The primary initiation site is characterised by an Al-, Si-, Mn-rich oxide particle (with trace elements of Mg, S, Ti, Cu) with a size of 1.8 µm.

The fracture surface of a representative C(T) specimens of reference non-aged material where brittle fracture primarily initiated from a broken particle is shown in Fig. 6. The specimen was tested at −140 °C with a fracture toughness of 54 MPa$\sqrt{m}$. As shown in Fig. 6(b, c), the primary initiation site locates in the RH region with polygonal ferrite microstructure. The initiator particle was broken and found located in both of the specimen halves (Fig. 6(d–i)). The primary initiation site is characterised by a Fe-, Mn- and Mo- carbide with some traces of S. The primary initiator has an irregular shape and a size of 1.8 µm. The same irregular shape of primary initiators were found in all of specimens of reference non-aged material, which was different from the round shape of primary initiators in the RPVH specimens.

For the RPVH WM, in addition to the dominant transgranular cleavage, interdendritic (ID) and IG fracture as the secondary fracture mode is observed on the fracture surfaces in the AW and RH microstructures, respectively (Fig. 5). The representative fracture surfaces in RH region (IG and cleavage) and AW region (ID and cleavage) are shown in Fig. 5(b, c) and Fig. 5(d–f), respectively. The ID and IG fracture surface shown in Fig. 5 has propagated along the GB ferrite. The size of GB ferrite in RH microstructure is smaller than in AW microstructure (as seen in the EBSD examinations) and thus the IG fracture in RH region is more local. The size of ID and IG fracture area corresponds well with the dendrite and prior austenite grain size of AW and RH regions. The ID and IG features have been occasionally observed in the reference non-aged state WM, with the fraction being smaller than in the thermally-aged materials.

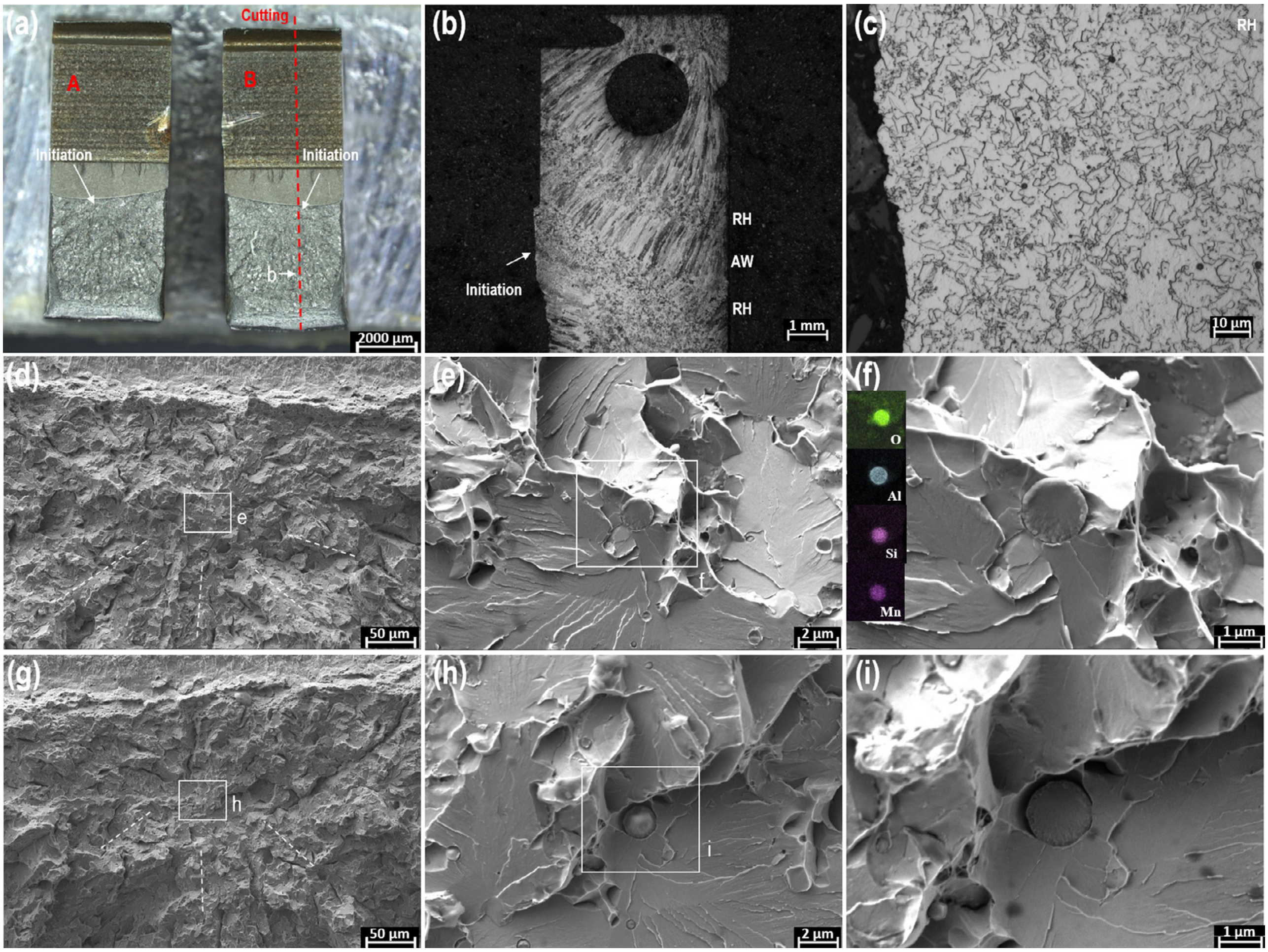

Fig. 4. (a) Parts A and B of a representative miniature C(T) specimen of the thermally-aged RPVH material (tested at −128.3 °C with fracture toughness of 123.9 MPa$\sqrt{m}$) showing the primary initiation site and the cutting line. (b, c) Cross section reveals that the primary initiation locates in the RH region. SEM images of primary initiation site of specimen half A (d–f) and half B (g–i). The brittle fracture initiated from an inclusion with breakage.

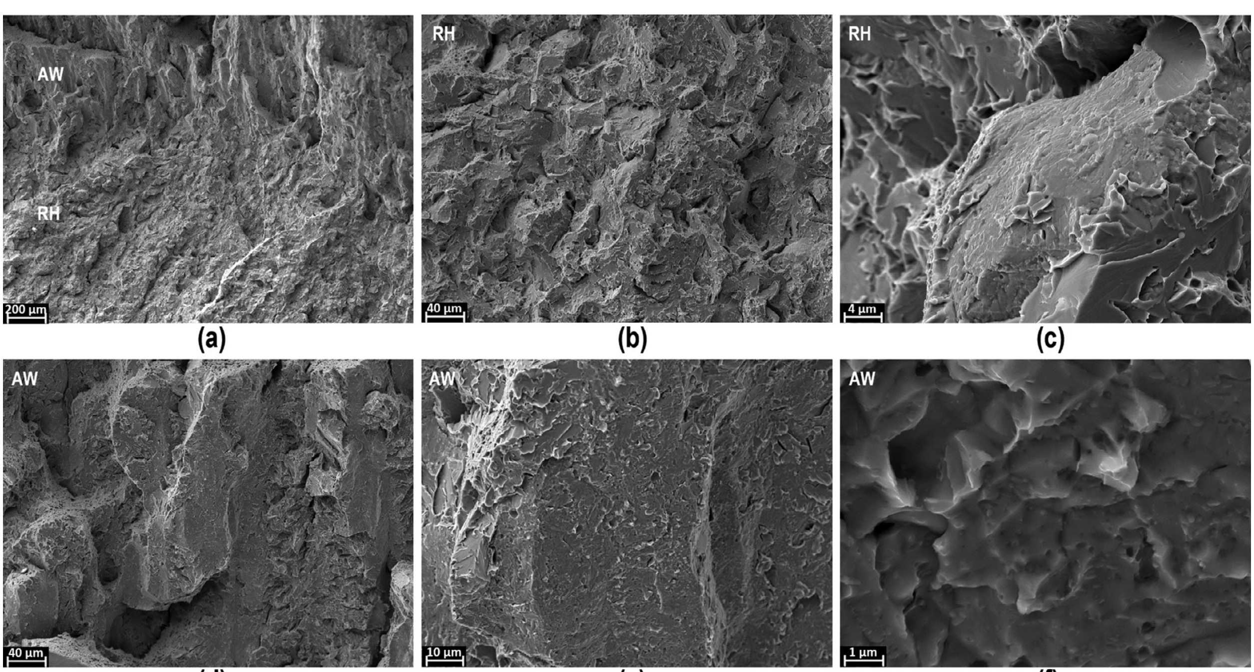

Fig. 5. (a) Representative brittle fracture surface of the thermally-aged RPVH material including both AW and RH regions. (b, c) Fracture surface of RH structure (IG and cleavage). (d–f) Fracture surface of AW structure (ID and cleavage).

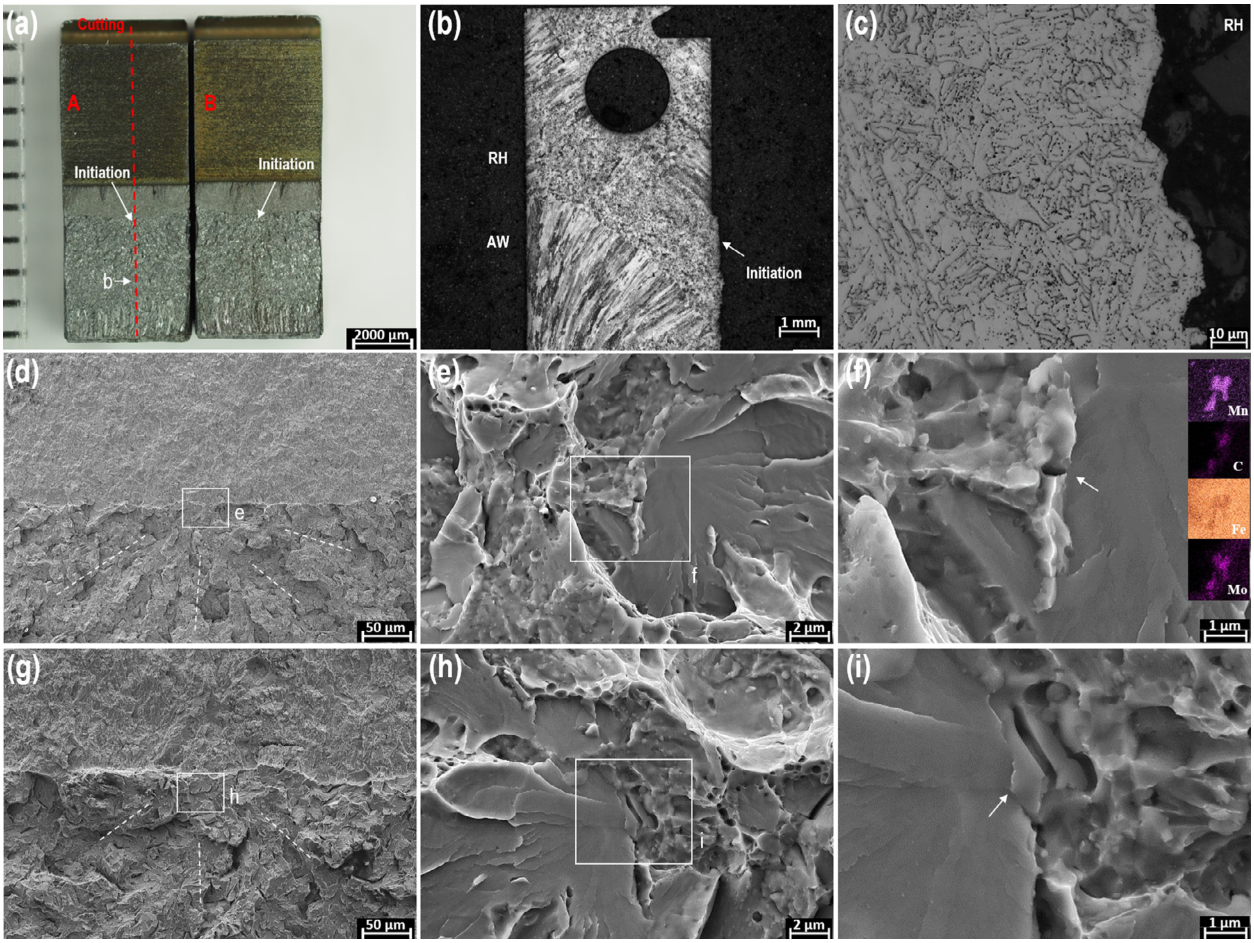

Fig. 6. (a) Parts A and B of a representative miniature C(T) specimen of reference non-aged material (tested at −140 °C with fracture toughness of 54 MPa$\sqrt{m}$) showing the primary initiation site and the cutting line. (b, c) Cross section reveals that the primary initiation locates in the RH region. SEM images of primary initiation site of specimen half A (d–f) and half B (g–i). The brittle fracture initiated from an inclusion with breakage.

3.3. Fracture initiation modelling

3.3.1. Modelling aspects

The characteristics of the non-metallic inclusions acting as the primary initiation site for brittle failure and existing as a part of the microstructure of RPVH WM are not well known. To address some of the key features possibly leading to premature damage of the material, a non-exhaustive listing may be identified as: (i) *interface conditions between inclusion and WM matrix*, how well is the inclusions initially attached and what is the area of detachment; (ii) *multi-phase heterogeneity of the oxide-inclusion*; (iii) *prior slip localisation near the interface region from manufacturing*; and (iv) *existing pre-cracks* within the inclusions and the damage behavior of inclusions during deformation. The simulations of this work focuses on analysing the susceptibility of inclusions to cause damage in the weld microstructure. Emphasis is placed on investigating the debonding behavior of the inclusions when they are initially fully adhered to the matrix metal.

Finite element based crystal plasticity simulations were performed on EBSD-based microstructural meshes. The computational domain was constructed based on the reconstruction of grains identified by their orientation to imitate the material's microstructure utilizing a subset of the measurement data from Fig. 2(b). Tensile loading was applied to the microstructure to investigate the susceptibility for inclusions to initiate damage and to compare with experimental stress-strain curves. Kinematic uniform boundary conditions were used to retain regularity of the domain, i.e., no localisation was allowed at the edges of the domain. Damage near the edges of the simulation domain was also prohibited to avoid interference from boundary conditions.

Three simulation cases were studied, involving a bulk microstructure without any inclusions and two microstructures containing three inclusions at different locations. The inclusion sizes range from 1.0 to 1.5 μm. No specific interface model is assigned between an inclusion and matrix and therefore any damage must occur as a description of metal failure. If the metal fails at the elements directly at the interface, it is judged as interface damage and debonding of the inclusion from the matrix, which occurs once damage resistance reaches its minimum value, i.e., crack has fully developed within the volume of the element. A transition from a nano-crack to microcrack is assumed when several elements in the cracked region are fully deteriorated and the crack itself extends significantly. Cracks can initiate anywhere in the metal matrix and they may propagate in the elements facing GB or intra-grain. GBs are modelled with an orientation change between different grains and therefore change in orientation naturally affects elastic-plastic deformation and damage responses. Table 6 lists the used crystal plasticity parameters.

3.3.2. Results from modelling

Fig. 7(a) shows the simulated and experimental strain-stress curves. Tensile strain is applied slightly exceeding the peak stress of the material to analyse the effect of inclusions on local damage. The inclusions have a slight hardening effect on the overall stress-

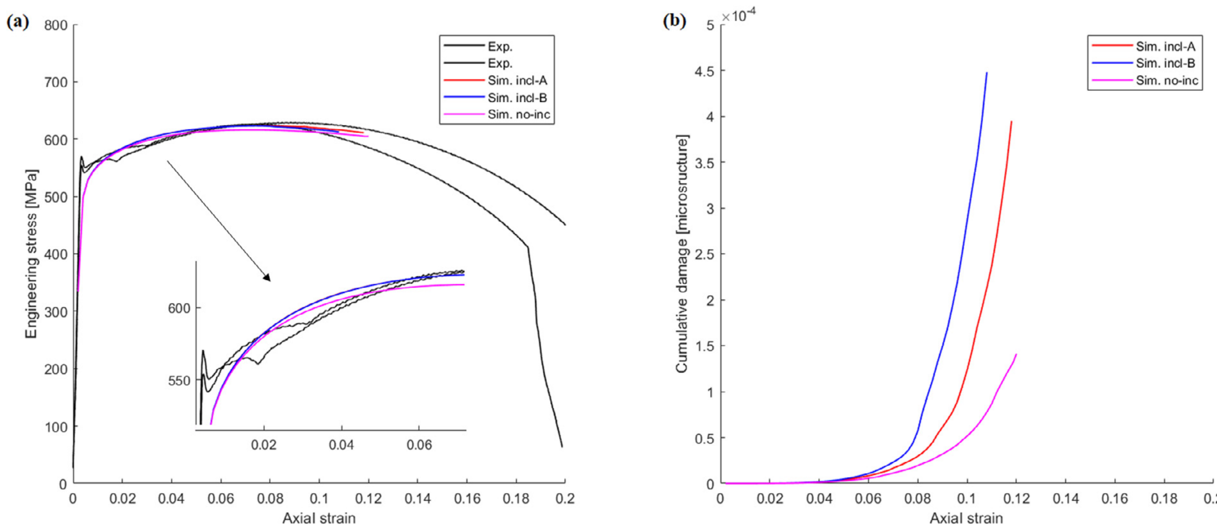

Fig. 7. (a) Experimental and simulated stress-strain curves for bulk and inclusion-containing microstructures and (b) the simulated accumulation of damage.

Table 6
Crystal plasticity parameters.

Parameter name	Parameter	Value and unit
Elastic constant	C_{11}	197 [GPa]
Elastic constant	C_{12}	134 [GPa]
Elastic constant	C_{44}	105 [GPa]
Slip parameters		
Strain rate parameter	N	15.0
Viscous parameter	K	155
Initial slip resistance	τ_0	155 [MPa]
Hardening parameter	Q	4.0 [MPa]
Hardening saturation	b	20.0
Interaction matrix	h1–h8	1.3, 1.0, 1.05, 1.15, 1.025, 1.3, 1.495, 1.0
Damage parameters		
Damage strain rate parameter	N_d	4.0
Damage viscous parameter	K_d	300.0
Initial damage resistance	σ_d^0	1300 [MPa]
Coupling plasticity-damage	β	0.25
Damage softening	H_{soft}	−3500 [MPa]
Micromorphic parameters		
Penalization modulus	H_χ	10,000.0 [MPa]
Higher order modulus	A	0.1 MPa. mm^2

strain curve in comparison to the bulk grain structure without inclusion. Fig. 7(b) shows the cumulative damage for the simulation cases. Damage initiates locally with around 5% of macroscopic strain and the presence of inclusions rapidly increases the damage rate. Fig. 8 illustrates damage maps overlain to the deformed microstructures. When there are no inclusions present, small-scale cracks emerge throughout the microstructure, especially near GBs. In both cases with inclusions, dominant cracks tend to appear primarily at the inclusion-matrix interface region and they continue to propagate to the metal matrix.

The inclusions are then partially debonded from one side or around the perimeter of the inclusion. However, it is seen in Fig. 8(c) that the inclusions do not necessarily lead to significant damage in all cases as possibly only small damage is accumulated at the vicinity of an inclusion. This indicates that the surrounding grain structure has a crucial role whenever the inclusions are judged as detrimental. The Von Mises stress contours show that inclusions affect the local stress state of the microstructure and the initiation of damage depends on the stress state and strain localisation near the inclusions, as the model couples plasticity and damage. It is worth noting that the maximum damage strain is limited to 5% in the figures for clarity. However, much higher local values are observed especially near the inclusions. In this work, a fully developed crack in the material was interpreted when the local damage resistance reaches limiting value, i.e., a close to zero value but non-zero for numerical convenience.

A qualitative local analysis was performed to investigate the effects of inclusions on driving the local damage and their debonding from the matrix with more focus on mesh discretisation than larger computational domains. Fig. 9 shows the used subset of EBSD map from Fig. 2(b). Artificial inclusions are placed at a triple point (Local A) and inside a large grain (Local B) so that the edges of the inclusion appear at the GB of two neighbouring grains. Although the local microstructure contains only a small amount of grains and thus it has a limited capability to represent the whole microstructure, this local analysis provides indication of the influence of inclusion on damage. Fig. 10 shows the stress-strain curves of the three cases. Inclusions with relatively large size introduce notable additional hardening for the material, while the location of the inclusion does not show any significant effect on strain hardening. When the inclusion is placed on the triple point, Fig. 10 indicates that early damage initiation and rapid propagation is observed. The inclusion located inside a large grain in the middle of the simulation domain also promotes damage growth at the vicinity of the inclusion, further confirming that damage susceptibility of the material depends on inclusion location within the microstructure.

Fig. 11 illustrates damage growth within the microstructure and the residual Von Mises stress at specific tensile strains. Damage is mainly observed at the interface of the inclusion and matrix leading to partial separation of the inclusions. However, damage was not observed for the bulk microstructure case without inclusion in Fig. 11(a) in the current simulation, which is a result of an overall lower stress state of the local microstructure and the lack of suitable nucleation sites. It is clearly seen that the inclusions affect the local stress state and the mismatch between matrix and inclusion introduces suitable conditions for a premature failure process.

4. Discussions

4.1. Weld microstructure

The ferrite phases present in the WM of RPVH are briefly discussed as following. Acicular ferrite is the dominant phase

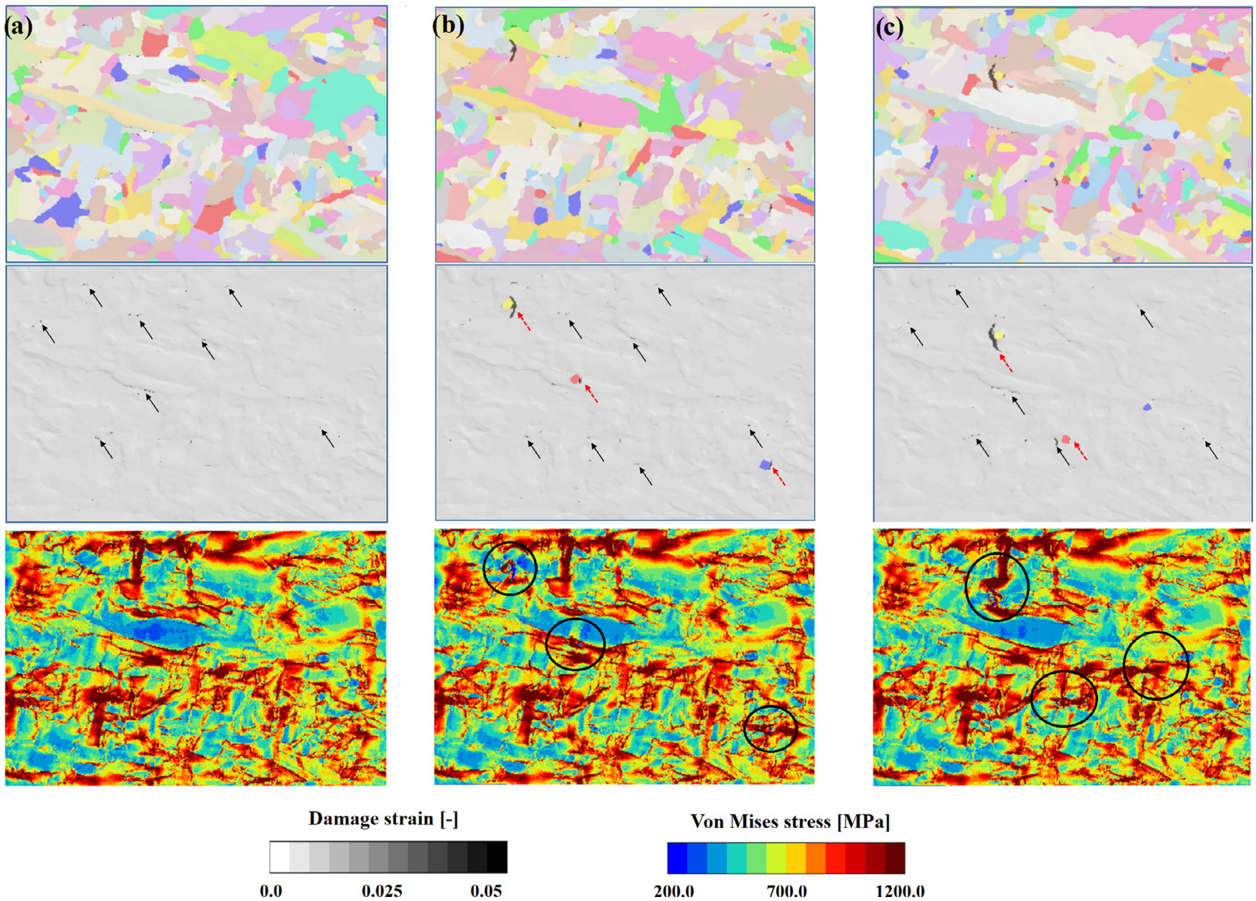

Fig. 8. Damage maps overlain to the deformed microstructure and Von Mises stress maps at the end of the simulations for (a) no inclusion, (b) case A with three inclusions, and (c) case B with three inclusions. Red arrows indicate inclusion debonding and black arrows show some of the matrix regions with initiated damage.

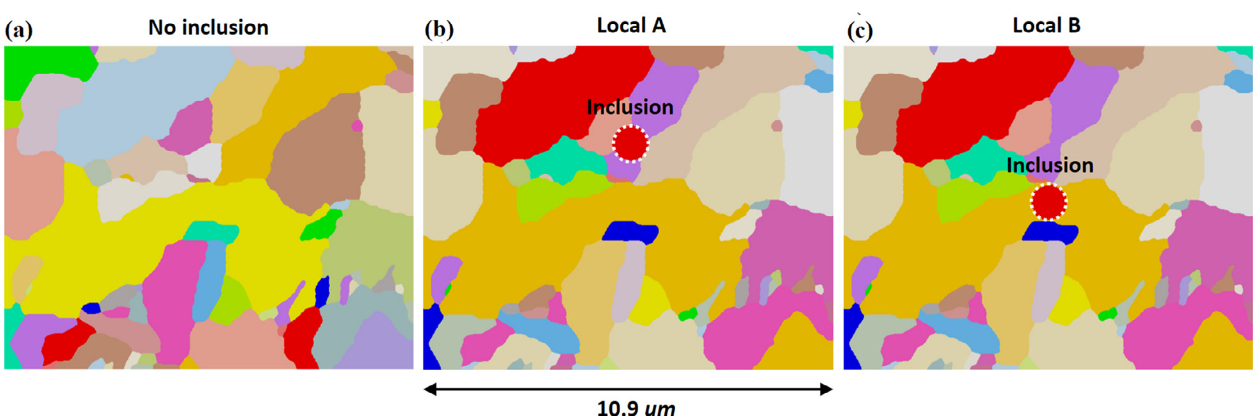

Fig. 9. Local microstructure with (a) no inclusion, (b) inclusion position A at a triple point, and (c) inclusion position B inside a grain. Size of the inclusion is circa one micron. Colours represent different grains and the inserted inclusions are highlighted.

in the AW dendrites. In addition, AW regions also consist of a small fraction of pro-eutectoid GB ferrite, Widmanstätten ferrite side plates and polygonal ferrite. Acicular ferrite is generally formed intragranularly by direct nucleation on the non-metallic inclusions, with a random crystallographic orientation and high angle boundaries between grains [39–41]. Moreover, acicular ferrites have much higher dislocation densities than GB allotriomorphic ferrite or Widmanstätten ferrite side plates [21]. These features make acicular ferrite tougher than the other ferrite phases and enable acicular ferrite laths to retard the propagation of a cleavage crack. GB allotriomorphic ferrite and Widmanstätten ferrite side plates are always present at the solidification dendritic boundary (Fig. 2). Pro-eutectoid GB ferrite forms at austenite grain surfaces at higher temperatures during the solidification and covers the whole GBs. Widmanstätten ferrite grows along well-defined planes of the austenite and towards austenite grain interiors [42] by directly emanating from austenitic GBs or from the existing allotriomorphic GB ferrite [43–45]. Widmanstätten ferrite can be unfavourable because Widmanstätten ferrite promotes brittle crack nucleation and propagation due to that the ferrite side plates nucleate and grow as parallel plates with the same crystallographic orientation and small angle boundaries. However, only locally small amount of Widmanstätten side plate ferrite is seen in the microstructure due to a competitive na-

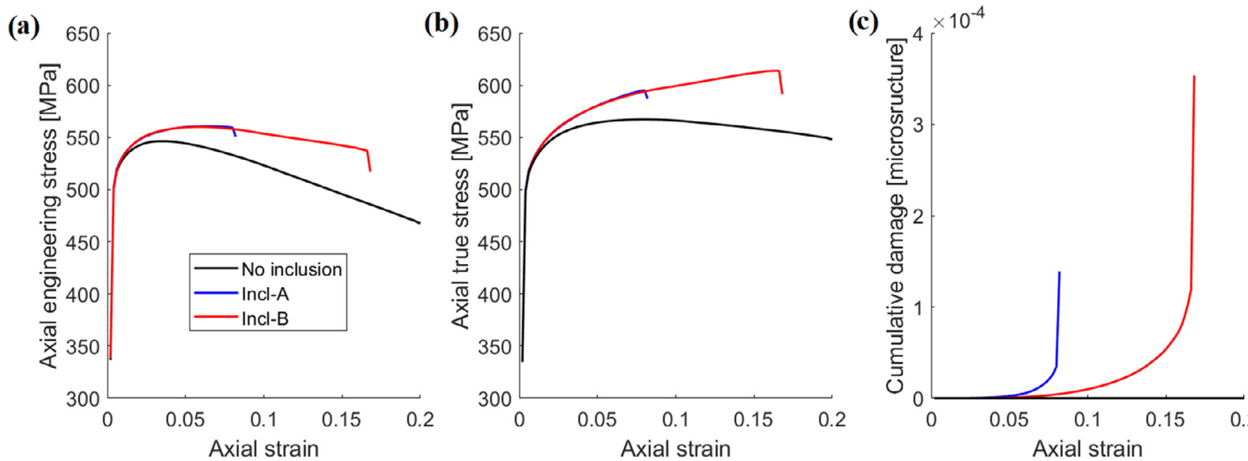

Fig. 10. (a) Engineering and (b) true stress-strain curves for a bulk material without inclusion and for the two cases with inclusions, and (c) cumulative damage strain average over the whole microstructure for the inclusions cases.

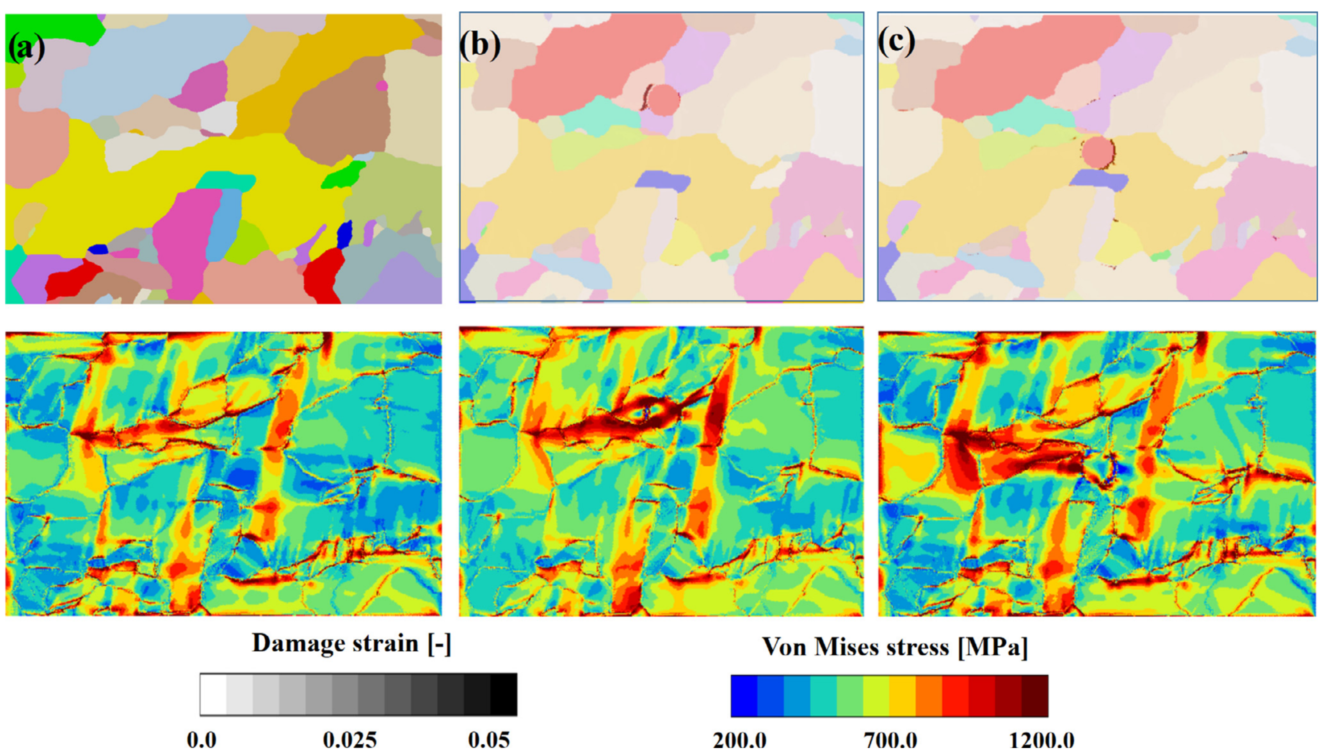

Fig. 11. Damage maps overlain to the deformed microstructure and Von Mises stress contours for (a) the local bulk material without inclusion at 16.8% of strain, (b) inclusion case A at 8.2% of strain, and (c) inclusion case B at 16.8% of strain. Tensile direction is from left to right.

ture between the formation of acicular ferrite and Widmanstätten side-plate ferrite, thus it did not play a major role in this study.

The RH zone is formed when the weld bead receives heat input again when welding a new weld bead on its top. Therefore, the RH zone is mainly consisted of polygonal ferrite due to the grain reconstruction and carbon diffusion with the new heat input. Compared to the AW zone, solidification boundaries and intragranular polygonal microstructural boundaries in RH zone also tend to become more granular. No Widmanstätten ferrite side plates are present in the RH zone.

The toughness of the WM mainly depend on the microstructure and proportion of different ferrite phases [46], particularly by the acicular ferrite. The AW microstructure is in general tougher than the RH region. The toughness decreases with an increasing amount of GB ferrite structure. The ID and IG fracture observed in this work confirm the weakening role of GB ferrite. ID fracture was observed in the AW region in C(T) specimens where the angle between the cracking plane and dendrite structure is low, i.e., $< 25°$. When the angle between brittle fracture cracking and dendrite structure is high, i.e., $> 45°$, no ID feature was found on the fracture surface. Therefore, a low angle between the pre-fatigue crack plane and the local dendrite orientation in the weld bead structure can be a prerequisite for ID cracking. If the angle is high, the brittle fracture propagates through the grains and results in cleavage fracture.

4.2. Correlation between toughness and brittle fracture initiation site

The critical local normal stress for non-metallic inclusion is generally lower than for structural boundaries/barriers at equal fracture toughness level [11], which results in the energy-

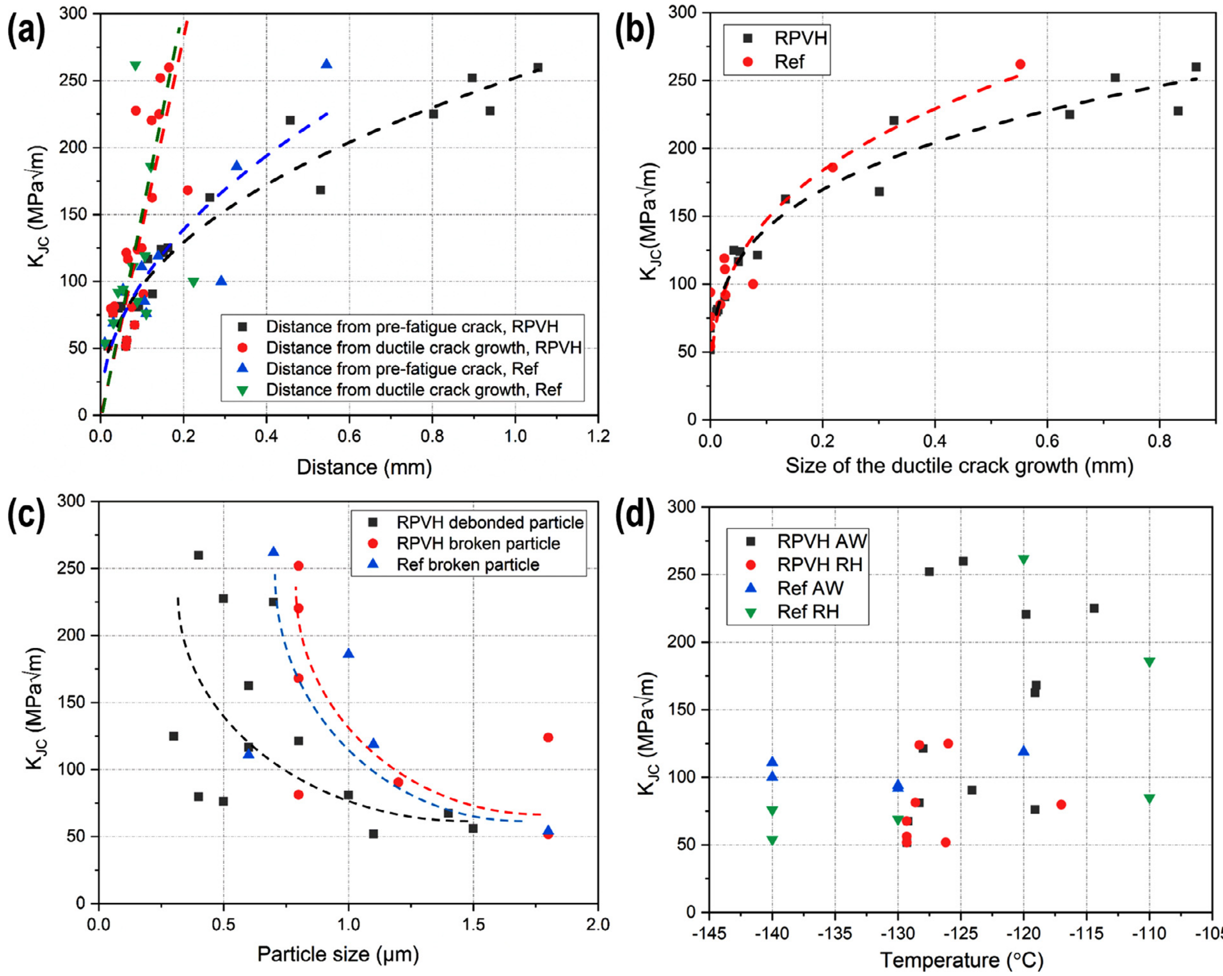

Fig. 12. Fracture toughness tests summary of the thermally-aged RPVH material and the reference non-aged WM. (a) Fracture toughness vs the distances of initiation sites from end of pre-fatigue (black square) and end of ductile crack growth (red circle). (b) Fracture toughness vs size of the ductile crack growth prior to brittle fracture. (c) Fracture toughness vs the initiating particle size (including both debonded and broken primary initiation particles). (d) Fracture toughness vs testing temperature and initiating microstructures.

preferable brittle fracture initiation from non-metallic inclusions. As revealed in this work, all brittle fracture primary initiation sites are non-metallic inclusions. For the thermally-aged RPVH WM, the majority of the primary initiators (with sizes of 0.3−1.8 μm) in T_0 testing specimens are debonded particles. For the reference non-aged WM, only broken inclusion particles with size of 0.6−1.8 μm were found in the T_0 testing C(T) specimens.

Some observations revealed by T_0 testing of thermally-aged RPVH material and the reference non-aged WMs are summarised in Fig. 12:

- The distance of primary initiation site from pre-fatigue crack front shows a correlation to the fracture toughness, Fig. 12(a). Specimens with higher fracture toughness values have initiation sites further from the pre-fatigue crack tip than specimens with lower fracture toughness. This follows the theory of weakest link, as there are initially no critical locations in the process zone close to the crack, the load increases together with the fracture process zone until a critical location is reached. The correlation follows a power law fitting.
- Though the C(T) specimens were tested at low temperatures and have a dominant brittle fracture, some small extents of preceding plastic deformation and ductile fracture prior to the brittle fracture were observed. A linear relation between the fracture toughness and the distance of initiator from the end of prior ductile crack growth is obtained (Fig. 12(a)). The two types of fitting curves in Fig. 12(a) shows elastic plastic and linear elastic behavior, respectively.
- Specimens with higher fracture toughness values have more prior ductile crack growth. The size of the ductile crack growth ranged from ∼0 to 0.865 mm. Fig. 12(b) shows a power law behavior and the fitting line for thermally-aged RPVH material seems to be slightly lower than that of the reference non-aged WM. Local plasticity at boundaries of inclusions are required to initiate cleavage fracture [47].
- Lower fracture toughness values are obtained in specimens with larger initiating particle size, as shown in Fig. 12(c). The required applied global stress for causing final fracture can be lower for larger particles since a larger particle creates a larger initial microcrack with higher energy release rate for easier crack propagation to the matrix. Similar observations were reported in literature [11,47].
- Brittle fracture of 13/20 of the C(T) specimens of RPVH WM initiated from a debonded particle while 7/20 initiated from broken particles. All of the initiating particles with a size $<$ 0.7 μm are debonded type and the initiators with a size of $>$1.6 μm are broken. Primary initiation particles between 0.7 and 1.6 μm are either broken or debonded. As shown in Fig. 12(c), with a similar initiator particle size, specimens with debonded initiators are likely to have a lower fracture toughness than the specimens with broken inclusions. Due to the large scatter in the

data points, an absolute conclusion requires more data. The fitted curves of the broken initiators of RPVH WM and reference non-aged WM in Fig. 12(c) are close to each other.

- Fig. 12(d) shows the fracture toughness as a function of test temperature and initiating microstructure (i.e., AW or RH regions). Specimens, in which brittle fracture initiated in the RH microstructure have lower fracture toughness values compared to specimens with initiation from the AW microstructure, particularly for thermally-aged RPVH material. The T_0 is −113 °C and −85 °C for the AW and RH structures in the RPVH material, respectively. As discussed in Chapter 4.1, the toughness of the acicular ferrite (the major microstructure in AW region) was higher than the other ferritic microstructure.

4.3. Brittle fracture initiation

In this work, a brittle fracture microcrack initiates either within the multi-phase oxide inclusions (leading to initiator breakage) or from the debonded interfaces between the uncracked inclusions and WM matrix (resulting into debonded initiator). The average diameter of inclusions in the investigated RPVH WM is ≤ 0.3 µm [30]. According to the weakest link theory, the brittle fracture initiates within the effective process zone from the weakest location (biggest inclusion). Based on the semi-quantitative EDS mapping from the primary brittle fracture initiation sites in RPVH WM, the initiators are generally multi-phase oxides with main elements of Mn, Si, and Al and other trace elements like S, Mg and Cu, which is similar to that found in thermally-aged WM in literature [20]. Depending on the particle size, chemical composition and surface status of the inclusions, stress state and testing temperature, the brittle microcrack initiates either by debonding or breakage in WM of thermally-aged RPVH. The oxides or carbides with a more brittle nature fulfil the Griffith criterion of brittle fracture initiation. With the existing defects or inclusion boundaries, the microcrack initiates within the inclusion, results in the breakage of the inclusion and further induces cleavage fracture [23]. For oxysulfides that are more ductile, void nucleation and coalescence at the particle-matrix interface result in debonding of the interfaces of intact inclusions to WM matrix. The exterior stress, which exceeds critical local normal stress [11], breaks the interatomic bonding between the inclusion and the matrix. Moreover, irregular-shape carbide type and round-shape oxide type initiators were found in specimens of reference non-aged and the RPVH specimens, respectively. The reason for the change of shape of the brittle fracture primary initiators is unclear. Nevertheless, irregular inclusions have sharp corners for high stress concentration, which might assist in the inclusion breakage.

For the decommissioned thermally-aged RPVH, there are more debonded initiators than broken initiators in T_0 testing specimens. However, WM of the non-aged reference condition revealed dominant broken primary initiators in T_0 testing specimens. It indicates that thermal aging could promote debonding as the brittle fracture initiation mechanism. Though macroscopically the thermal embrittlement effect on toughness are not significant (due to the moderate thermal aging temperature, low matrix P content and possibly also the absence of neutron irradiation in RPVH WM), the thermal aging could promote the interface/boundary segregation and thus debonding phenomenon [48,49]. The long-term thermal operation can enhance the elemental segregation of impurities (e.g., P, S, etc.) to the particle surfaces and GBs and decrease the cohesion strength of the particle-matrix interface [11]. The high nickel content of the WM can accelerate the process of P segregation [9]. Miao and Knott [24] reported that fracture toughness was not significantly changed with the formation of sulphide coatings on the surface of inclusions but the primary initiation from debonded particles were clearly associated with sulphide “patches” on inclusions. In the study by Boåsen et al. [25] [50], enhanced debonding as a consequence of thermal aging was reported. Filho et al. [47] reported the fracture stresses produced by failure from cracked inclusions are not significantly different to that produced when inclusions were decohered from matrix. This means that as inclusion cracks, it partly blunts out at the interface and thus leads to a similar level of fracture stress that is not much higher than from a decohered inclusion. This is in line with the finding in Fig. 12(c) and it further indicates the potential role of thermal aging in promoting the brittle fracture initiation with decohesion/debonding and the fracture stresses required are not fundamentally different.

4.4. Correlation of brittle fracture with crystal plasticity modelling

Though the C(T) specimens were tested at low temperatures and have a dominant brittle fracture failure, preceding plastic deformation and ductile fracture prior to brittle fracture are required and were observed on the fracture surface. Local plasticity at boundaries between inclusions and WM matrix are required to initiate the cleavage fracture. Crystal plasticity simulations were performed to investigate the effect of debonding non-metallic oxide inclusions on damage initiation. The grain structure imposes heterogeneous stress fields under deformation with typical interactions between the grains and elevated stress concentrations near GBs, as was shown in Figs. 8(a) and 11(a). The simulations performed on microstructures containing oxide inclusions show that the local stress state of the material is altered. If the inclusions are fully attached to the matrix, it tends to temporarily strengthen the microstructure, while in turn providing more convenient conditions for damage to occur depending on the orientations and morphology of the surrounding grains. The crystal plasticity simulations effectively show the debonding of the inclusions as a premature damage mechanism.

However, inclusion breakage was not treated with the model in the absence of damage model assigned to the inclusions themselves and thus no separation between debonding and particle breakage promoted cracking was done. Yet, once the interface has effectively separated, the crack front can continue to propagate in the matrix grains quickly after debonding had taken place, while some cracks remained arrested at the matrix GBs. This behavior describes the semi-brittle behavior of the material, where further deformation could allow significant and fatal crack growth. It was also noted that not all inclusions promote inclusion debonding from the matrix, as they can also support matrix damage process away from the interface due to the alterations in the local stress and strain fields, as is seen in Fig. 8(c).

The simulations were restricted to 2D EBSD map based grain structures, which enforces planar stress-strain states and damage growth. This limits the prediction capability of the modelling approach to further investigate large growth of damage in the material as crack growth process is essentially a 3D process, and therefore simulations were restricted to early damage phenomena. Future research could be focused on preparing sufficiently representative 3D microstructures and to have sensitivity analysis on various types of inclusions in the material as well as involvement of fracturing inclusions. Furthermore, the inclusion-matrix interface conditions are not necessarily ideal as the inclusions can be weakly adhered to the matrix or partially separated. The inclusions themselves may be heterogeneous that could be significant in terms of the overall local failure process (debonding/inclusion breakage). Such efforts require well-described synthetic and realistic 3D grain structure, either by serial-slicing EBSD reconstruction or volume-scanning synchrotron measurement.

5. Conclusions

In this work, the initiation of brittle fracture in thermally-aged high-Ni WM from a decommissioned BWR RPVH (in operation at 288 °C for 23 effective full power years) was investigated and compared to its non-aged reference condition. The mechanical testing, microstructure characterisation, fractographic examination and modelling revealed the following conclusions:

- The influence of long-term thermal aging on the fracture and impact toughness, hardness, and tensile properties of the WM in decommissioned thermally-aged RPVH compared to the non-aged reference condition are not significant.
- In the RPVH WM, round-shape oxide type initiators are found at the primary initiation sites for brittle failure and there are more debonded inclusion than broken inclusions. For the reference non-aged WM, irregular-shape and broken carbide type of primary initiators are found.
- Thermal aging could promote the debonding at the brittle fracture primary initiation sites possibly due to enhanced segregation. The long-term thermal operation promote the elemental segregation of impurities (e.g., P, S, etc.) to the particle surfaces and GBs and decrease the cohesion strength of the particle-matrix interface or GBs and facilitate the occurrence of cleavage fracture event.
- Transgranular cleavage as the dominant fracture mechanism and ID and IG fracture as the secondary fracture mode are observed. The amount of IG fracture appears to be higher in the RPVH samples than the reference material.
- Fracture toughness increases with the distance of the initiation site from the pre-fatigue crack and the size of the prior ductile crack growth before brittle fracture initiation, but decreases with the size of the initiator particle. Specimens with debonded initiators are likely to have a slightly lower fracture toughness than the specimens with broken inclusions with a similar size of primary initiator. Specimens, in which brittle fracture initiates in the RH microstructure have lower fracture toughness values compared to specimens, where initiation occurs in the AW microstructure.
- The crystal plasticity modelling with a semi-brittle behavior of the WM microstructure (EBSD-based microstructural meshes) exhibiting plasticity prior to fracture, revealed the promoting role of debonded inclusions for the premature evolution of cumulative damage and cleavage cracking. Damage is mainly observed at the interface of the inclusion and matrix leading to partial separation of the inclusions and the microcrack that forms continue to propagate to the metal matrix. And the severity of damage caused by inclusions depend on the location of the inclusion, surrounding matrix and grain orientation.

Declaration of Competing Interest

The authors declare that they have no known competing financial interests or personal relationships that could have appeared to influence the work reported in this paper.

CRediT authorship contribution statement

Zaiqing Que: Conceptualization, Data curation, Formal analysis, Investigation, Methodology, Supervision, Writing – original draft, Writing – review & editing. **Matti Lindroos:** Conceptualization, Data curation, Formal analysis, Investigation, Methodology, Writing – original draft. **Jari Lydman:** Conceptualization, Data curation, Formal analysis, Investigation, Methodology, Writing – review & editing. **Noora Hytönen:** Data curation, Formal analysis, Investigation, Writing – review & editing. **Sebastian Lindqvist:** Investigation, Methodology, Writing – review & editing. **Pål Efsing:** Conceptualization, Project administration, Resources, Supervision, Writing – review & editing. **Pekka Nevasmaa:** Conceptualization, Writing – review & editing. **Pentti Arffman:** Conceptualization, Funding acquisition, Data curation, Project administration, Resources, Writing – review & editing.

Data availability

Data will be made available on request.

Acknowledgments

The authors gratefully acknowledge the SAFIR2022 BRUTE project (Barsebäck RPV material used for true evaluation of embrittlement) and ENTENTE project (Euratom research and training programme 2019–2020 under grant agreement No. 900018) for funding the study. The authors thank the BREDA program (Barsebäck Research and Development Arena) for providing the research material. The contributions and discussions with U. Ehrnstén from VTT, M. Boåsen from KTH and Kristina Lindgren from CUT are acknowledged.

References

[1] W. Morgan, J. Livingston, A Review of Information for Managing Aging in Nuclear Power Plants, Pacific Northwest Laboratory, 1995.
[2] P. Haušild, C. Berdin, P. Bompard, Prediction of cleavage fracture for a low-alloy steel in the ductile-to-brittle transition temperature range, Mater. Sci. Eng. A 391 (1–2) (2005) 188–197.
[3] Y. Shtrombakh, B. Gurovich, E. Kuleshova, D. Maltsev, S. Fedotova, A. Chernobaeva, Thermal ageing mechanisms of VVER-1000 reactor pressure vessel steels, J. Nucl. Mater. 452 (2014) 348–358.
[4] IAEAIntegrity of Reactor Pressure Vessels in Nuclear Power Plants: Assessment of Irradiation Embrittlement Effects in Reactor Pressure Vessel Steels, International Atomic Energy Agency Nuclear Energy, 2009 Series No. NP-T-3.11.
[5] J. Hyde, G. Sha, E. Marquis, A. Morley, K. Wilford, T. Williams, A comparison of the structure of solute clusters formed during thermal ageing and irradiation, Ultramicroscopy 111 (2011) 664–671.
[6] K. Lindgren, M. Boåsen, K. Stiller, P. Efsing, M. Thuvander, Evolution of precipitation in reactor pressure vessel steel welds under neutron irradiation, J. Nucl. Mater. 488 (2017) 222.
[7] P. Joly, L. Sun, P. Efsing, J. Massoud, F. Somville, R. Gerard, Y. An, J. Bailey, Characterization of in-service thermal ageing effects in base materials and welds of the pressure vessel of a decommissioned PWR pressurizer, after 27 years of operation, in: Proceedings of the 19th International Conference on Environmental Degradation of Materials in Nuclear Power Systems-Water Reactors 2019, Boston, 2019.
[8] D. Sprouster, J. Sinsheimer, E. Dooryhee, S. Ghose, P. Wells, T. Stan, N. Almirall, G. Odette, L. Ecker, Structural characterization of nanoscale intermetallic precipitates in highly neutron irradiated reactor pressure vessel steels, Scr. Mater. 113 (2016) 18.
[9] B. Margolin, E. Yurchenko, A. Morozov, D. Chistyakov, Prediction of the effects of thermal ageing on the embrittlement of reactor pressure vessel steels, J. Nucl. Mater. 44 (2014) 107–114.
[10] B. Gurovich, A. Chernobaeva, D. Erak, E. Kuleshova, D. Zhurko, V. Papina, M. Skundin, D. Maltsev, Chemical composition effect on VVER-1000 RPV weld metal thermal aging, J. Nucl. Mater. 465 (2014) 540–549.
[11] E. Kuleshova, A. Erak, A. Kiselev, S. Bubyakin, A. Bandura, Influence of operation factors on brittle fracture initiation and critical local normal stress in SE(B) type specimens of VVER reactor pressure vessel steels, J. Nucl. Mater. 467 (2015) 927–936.
[12] K. Lindgren, M. Boåsen, K. Stiller, P. Efsing, M. Thuvander, Cluster formation in in-service thermally aged pressurizer welds, J. Nucl. Mater. 504 (2018) 23.
[13] P. Styman, J. Hyde, K. Wilford, A. Morley, G. Smith, Precipitation in long term thermally aged high copper, high nickel model, Prog. Nucl. Energy 57 (2012) 86–92.
[14] P. Styman, J. Hyde, A. Morley, K. Wilford, N. Riddle, G. Smith, The effect of Ni on the microstructural evolution of high Cu reactor pressure vessel steel welds after thermal ageing for up to 100,000 h, Mater. Sci. Eng. A 736 (2018) 111–119.
[15] K. Lindgren, M. Boåsen, Z. Que, K. Stiller, P. Efsing, M. Thuvander, Post-irradiation annealing of high flux irradiated and surveillance material reactor pressure vessel weld metal, J. Nucl. Mater. 562 (2022) 153586.
[16] P. Bowen, S. Druce, J. Knott, Effects of microstructure on cleavage fracture in pressure vessel steel, Acta Metall. 34 (6) (1986) 1121.
[17] C. McMahon, M. Cohen, Initiation of cleavage in polycrystalline iron, Acta Metall. 13 (6) (1965) 591–604.

[18] D. Fairchild, D. Howden, W. Clark, The mechanism of brittle fracture in a microalloyed steel: part I. inclusion-induced cleavage, Metall. Mater. Trans. A 31A (2000) 641–652.
[19] H. Hein, J. Kobiela, M. Brumovsky, C. Huotilainen, J. Lydman, B. Marini, B. Radiguet, O. Startsev, M. Serrano Garcia, R. Hernandez Pascual, F. Roeder, H. Viehrig, Addressing of specific uncertainties in the determination of RPV fracture toughness in the SOTERIA project, in: Proceedings of the Fontevraud 9-Contribution of Materials Investigations and Operating Experience to Light Water NPPs' Safety, Performance and Reliability, Avignon, 2018.
[20] Y. Oh, B. Lee, J. Hong, The effect of non-metallic inclusions on the fracture toughness master curve in high copper reactor pressure vessel welds, J. Nucl. Mater. 301 (2002) 108–117.
[21] D. Sarma, A. Karasev, P. Jönsson, On the role of non-metallic inclusions in the nucleation of acicular ferrite in steels, ISIJ Int. 49 (7) (2009) 1063.
[22] A. Griffith, The phenomena of rupture and flow in solids, Philos. Trans. R. Soc. Lond. 221 (1921) 163.
[23] A. Pineau, A. Benzerga, T. Pardoen, Failure of metals I: Brittle and ductile fracture, Acta Mater. 107 (2016) 424.
[24] P. Miao, J. Knott, Effects of Inclusions and their surface chemistry on cleavage fracture in a C-Mn steel weld metal, in HSLA Steels 2015, Microalloying 2015 & Offshore Engineering Steels 2015, Springer, 2015.
[25] M. Boåsen, C. Dahlberg, P. Efsing, J. Faleskog, A weakest link model for multiple mechanism brittle fracture-model development and application, J. Mech. Phys. Solids 147 (2021) 104224.
[26] W. Weibull, A statistical distribution function of wide applicability, J. Appl. Mech. 18 (1951) 293.
[27] F. Beremin, A. Pineau, F. Mudry, J. Devaux, Y. D'Escatha, P. Ledermann, A local criterion for cleavage fracture of a nuclear pressure vessel steel, Metall. Trans. A 14 (1983) 2277.
[28] M. Miller, K. Powers, R. Nanstad, P. Efsing, Atom probe tomography characterizations of high nickel, low copper surveillance RPV welds irradiated to high fluencies, J. Nucl. Mater. 437 (1–3) (2013) 107.
[29] K. Gott and Y. Haag, "Barsebäck 2, RA 90 Surveillanceprovning av reaktortankmaterial„" Studsvik/NS-90/152 rev 1. 2022
[30] N. Hytönen, Z. Que, P. Arffman, J. Lydman, P. Nevasmaa, U. Ehrnstén, P. Efsing, Effect of weld microstructure on brittle fracture initiation in the thermally-aged boiling water reactor pressure vessel head weld metal, Int. J. Miner. Metall. Mater. 28 (2021) 867–876.
[31] M. Lindroos, J.M. Scherer, S. Forest, A. Laukkanen, T. Andersson, J. Vaara, A. Mäntylä, T. Frondelius, Micromorphic crystal plasticity approach to damage regularization and size effects in martensitic steels, Int. J. Plast. 151 (2022) 103187.
[32] O. Aslan, N. Cordero, A. Gaubert, S. Forest, Micromorphic approach to single crystal plasticity and damage, Int. J. Eng. Sci. 49 (12) (2011) 1311–1325.
[33] P. Sabnis, S. Forest, J. Cormier, Microdamage modelling of crack initiation and propagation in FCC single crystals under complex loading conditions, Comput. Methods Appl. Mech. Eng. 312 (2016) 468–491.
[34] J. Scherer, J. Besson, S. Forest, J. Hure, B. Tanguy, Strain gradient crystal plasticity with evolving length scale: application to voided irradiated materials, Eur. J. Mech. A Solids 77 (2019) 103768.
[35] J. Scherer, J. Besson, S. Forest, J. Hure, B. Tanguy, A strain gradient plasticity model of porous single crystal ductile fracture, J. Mech. Phys. Solids 156 (2021) 104606.
[36] M. Lindroos, T. Andersson, J. Metsäjoki, A. Laukkanen, Crystal Plasticity with micromorphic regularization in assessing scale dependent deformation of polycrystalline doped copper alloys, Crystals 11 (2021) 994.
[37] T. Hoc, S. Forest, Polycrystal modelling of IF-Ti steel under complex loading path, Int. J. Plast. 17 (1) (2001) 65–85.
[38] M. Lindroos, A. Laukkanen, T. Andersson, J. Vaara, A. Mäntylä, T. Frondelius, Micromechanical modeling of short crack nucleation and growth in high cycle fatigue of martensitic microstructures, Comput. Mater. Sci. 170 (2019) 109185.
[39] J. Byun, J. Shim, Y. Cho, D. Lee, Non-metallic inclusion and intragranular nucleation of ferrite in Ti-killed C–Mn steel, Acta Mater. 49 (12) (2003) 593–1606.
[40] J. Shim, Y. Oh, Y. Cho, J. Shim, J. Byun, D. Lee, Ferrite nucleation potency of non-metallic inclusions in medium carbon steels, Acta Mater. 49 (12) (2001) 2115–2122.
[41] S. Babu, H. Bhadeshia, A direct study of grain boundary allotriomorphic ferrite crystallography, Mater. Sci. Eng. A 142 (2) (1991) 209–219.
[42] L. Cheng, X. Wan, K. Wu, Three-dimensional morphology of grain boundary Widmanstätten ferrite in a low carbon low alloy steel, Mater. Charact. 61 (2) (2010) 192–197.
[43] L. Cheng, K. Wu, X. Wan, R. Wei, *In-situ* observation on the growth of Widmanstätten sideplates in an Fe–C–Mn steel, Mater. Charact. 87 (2014) 86–94.
[44] D. Phelan, R. Dippenaar, Widmanstätten ferrite plate formation in low-carbon steels, Metall. Mater. Trans. A 35 (2004) 3701–3706.
[45] D. Phelan, N. Stanford, R. Dippenaar, *In situ* observations of Widmanstätten ferrite formation in a low-carbon steel, Mater. Sci. Eng. A 407 (1–2) (2005) 127–134.
[46] H. Bhadeshia, L. Svensson, Modelling the evolution of microstructure in steel weld metal, in: Mathematical Modelling of Weld Phenomena, Institute of Materials, London, 1993, pp. 109–182.
[47] W. Filho, A. Carvalho, P. Bowen, Micromechanisms of cleavage fracture initiation from inclusions in ferritic welds part I. quantification of local fracture behavior observed in notched testpieces, Mater. Sci. Eng. A 460–461 (2007) 436–452.
[48] J. Lydman, S. Lindqvist, P. Nevasmaa, U. Ehrnstén, "Microstructural characterization of non-irradiated Barsebäck RPV base material and weld metal," VTT Report, VTT-R-05125-18, 2018, Espoo Finland.
[49] Z. Que, H. Seifert, P. Spätig, J. Holzer, A. Zhang, G. Rao, S. Ritter, Environmental degradation of fracture resistance in high-temperature water environments of low-alloy reactor pressure vessel steels with high sulphur or phosphorus contents, Corros. Sci. 154 (2019) 191–207.
[50] M. Boåsen, Modeling of Structural Integrity of Aged Low Alloy Steels Using Non-Local Mechanics, KTH Royal Institute of Technology, Stockholm, Sweden, 2020.